TECHNICAL REPORT

NASA Research Grant NAG-1-279
(UMass Account #5-28903)

"Near Millimeter Wave Imaging/Multi-Beam Integrated Antennas"

Period Covered: April 1, 1985 - September 30, 1985

Principal Investigator: Professor K. Sigfrid Yngvesson
Co-Investigators: Assoc. Prof. Daniel H. Schaubert

Department of Electrical and Computer Engineering
University of Massachusetts
Amherst, MA 01003

The progress on Grant NAG-1-279, is described in several attached manuscripts. A comprehensive list of these manuscripts, and their status with respect to publication, follows:

App. I: R. Janaswamy and D.H. Schaubert, "Additional Results on the Radiating Properties of LTSA's and CWSA's", a technical report.

App. II: R. Janaswamy and D.H. Schaubert, "Characteristic Impedance of a Wide Slot Line on Low Permittivity Substrates", submitted to the IEEE Trans. Microwave Theory and Techn.

App. III: R. Janaswamy, D.H. Schaubert, and D.M. Pozar, "Analysis of the TEM Mode Linearly Tapered Slot Antenna", submitted to Radio Science.

App. IV: K.S. Yngvesson, J. Johansson, and E.L. Kollberg, "Millimeter Wave Imaging System with an Endfire Receptor Array", Accepted paper for the 10th International Conference on Infrared and Millimeter Waves, Orlando, Florida, December 1985.

App. V: K.S. Yngvesson, "Imaging Front-End Systems for Millimeter Waves and Submillimeter Waves", Invited paper for the SPIE Conference on Submillimeter Spectroscopy, Cannes, France, December 5-6, 1985.

App. VI: J. Johansson, E.L. Kollberg, and K.S. Yngvesson, "Model Experiments with Slot Antenna Arrays for Imaging", ibid.

App. VII: K.S. Yngvesson, J. Johansson, and E.L. Kollberg, "A New Integrated Slot Element Feed Array for Multi-Beam Systems", submitted to the IEEE Trans. Antennas and Propagat., October 1985.

App. VIII: T.L. Korzeniowski, "A 94 GHz Imaging Array Using Slot Line Radiators, Technical Report", (Ph.D. thesis).

The following papers, submitted in an earlier technical report, have now been published or accepted for publication:

1) R. Janaswamy and D.H. Schaubert, "Dispersion Characteristics for Wide Slotlines on Low-Permittivity Substrates", IEEE Trans. Microw. Theory Techn., MTT-33, 723-726 (Aug. 1985).

2) K.S. Yngvesson, D.H. Schaubert, T.L. Korzeniowski, E.L. Kollberg, and J. Johansson, "Endfire Tapered Slot Antennas on Dielectric Substrates", accepted for publication in the IEEE Trans. Antennas Propag., December Issue, 1985.

SMR
(175)

TECHNICAL REPORT

NASA Research Grant NAG-1-279
(UMass Account #5-28903)

"Near Millimeter Wave Imaging/Multi-Beam Integrated Antennas"

Period Covered: April 1, 1985 - September 30, 1985

Principal Investigator: Professor K. Sigfrid Yngvesson
Co-Investigators: Assoc. Prof. Daniel H. Schaubert

Department of Electrical and Computer Engineering
University of Massachusetts
Amherst, MA 01003

The progress on Grant NAG-1-279, is described in several attached manuscripts. A comprehensive list of these manuscripts, and their status with respect to publication, follows:

App. I: R. Janaswamy and D.H. Schaubert, "Additional Results on the Radiating Properties of LTSA's and CWSA's", a technical report.

App. II: R. Janaswamy and D.H. Schaubert, "Characteristic Impedance of a Wide Slot Line on Low Permittivity Substrates", submitted to the IEEE Trans. Microwave Theory and Techn.

App. III: R. Janaswamy, D.H. Schaubert, and D.M. Pozar, "Analysis of the TEM Mode Linearly Tapered Slot Antenna", submitted to Radio Science.

App. IV: K.S. Yngvesson, J. Johansson, and E.L. Kollberg, "Millimeter Wave Imaging System with an Endfire Receptor Array", Accepted paper for the 10th International Conference on Infrared and Millimeter Waves, Orlando, Florida, December 1985.

App. V: K.S. Yngvesson, "Imaging Front-End Systems for Millimeter Waves and Submillimeter Waves", Invited paper for the SPIE Conference on Submillimeter Spectroscopy, Cannes, France, December 5-6, 1985.

App. VI: J. Johansson, E.L. Kollberg, and K.S. Yngvesson, "Model Experiments with Slot Antenna Arrays for Imaging", ibid.

App. VII: K.S. Yngvesson, J. Johansson, and E.L. Kollberg, "A New Integrated Slot Element Feed Array for Multi-Beam Systems", submitted to the IEEE Trans. Antennas and Propagat., October 1985.

App. VIII: T.L. Korzeniowski, "A 94 GHz Imaging Array Using Slot Line Radiators, Technical Report", (Ph.D. thesis).

The following papers, submitted in an earlier technical report, have now been published or accepted for publication:

1) R. Janaswamy and D.H. Schaubert, "Dispersion Characteristics for Wide Slotlines on Low-Permittivity Substrates", IEEE Trans. Microw. Theory Techn., MTT-33, 723-726 (Aug. 1985).

2) K.S. Yngvesson, D.H. Schaubert, T.L. Korzeniowski, E.L. Kollberg, and J. Johansson, "Endfire Tapered Slot Antennas on Dielectric Substrates", accepted for publication in the IEEE Trans. Antennas Propag., December Issue, 1985.

Appendices I-III describe the most recent work on the theory of single element LTSAs and CWSAs. The radiation mechanism for these is presently well understood and allows quantitative calculation of beamwidths and sidelobe levels, provided that the antennas have a sufficiently wide conducting region on either side of the tapered slot.

Appendices IV-VII represent earlier work on the grant, as well as work done during Professor Yngvesson's sabbatical visit to Chalmers University of Technology, Gothenburg, Sweden, from Jan. 1, through Aug. 1, 1985 and work done after Professor Yngvesson's return to the University of Massachusetts. This work further elucidates the properties of arrays of CWSA elements, and the effects of coupling on the beam-shape. It should be noted that typical beam-efficiencies of 65% have been estimated, and that element spacings of about one Rayleigh unit are possible. Further, two-point resolution at the Rayleigh spacing has been demonstrated for a CWSA array in a 30.4 cm paraboloid at 31 GHz. These results underscore the interest in further studies of the radiation mechanism of tapered slot arrays.

Appendix VII constitutes a final, detailed report on the work leading to a 94 GHz seven element LTSA array imaging system, which has been reported previously in less detail.

D1

N86-12479

APPENDIX I

Additional Results on the Radiating Properties of LTSAs and CWSAs

October 1985.

TABLE OF CONTENTS

Abstract: In this report, we present results on the theoretical and experimental investigations of the radiating properties of Linearly Tapered Slot Antennas (LTSAs) and Constant Width Slot Antennas (CWSAs) carried out during April - August 1985. The antenna is treated as a flared slot radiating in the presence of a conducting half plane. The aperture distribution in the flared slot is determined by approximating the tapered structure as a series of short sections of parallel slots. The slot field of a uniform slotline is determined by employing the spectral Galerkin's technique and a power conservation criterion is employed to match the fields at the step junction between two successive sections. Comparison is made between theory and experiment for several LTSAs and CWSAs etched on ε_r =2.22 and 2.55 substrates, and for flare angles $4^o \leq \gamma \leq 10^o$. It is shown that the theory adequately models the physics of the problem when the lateral dimension D of the antenna is large and when the propagation constant of a parallel slot line can be estimated very accurately. Newly observed effects of the lateral truncation on the radiation pattern of the antenna are discussed.

I. INTRODUCTION

A detailed description of the problem formulation and some preliminary results on CWSAs are given in the previous report under the Aperture Field Model (AFM). We shall briefly summarize the key steps involved in the model and discuss at length the results of the AFM on the LTSAs and CWSAs.

Fig. 1 shows the geometry of the LTSA. The method of analysis essentially involves two steps. In the first step, we determine the aperture distribution (i.e., electric field distribution) in the tapered slot region. In the second step, the equivalent magnetic current in the slot is assumed to radiate in the presence of a conducting half plane and the far-field components of the antenna are obtained.

The aperture distribution in the slot region is obtained in the following manner. The two lateral edges cd and c'd' are far enough from the slot so that they have little effect on the field distribution in the slot. The LTSA is consequently extended laterally in both directions to infinity. Also, the slot truncation at bc and b'c' is assumed to result only in a reflected wave of the dominant mode. (Note that this does not mean that we are ignoring the important near field scattering due to the edges bc, b'c'. This point will be clarified shortly.) Hence as far as finding the aperture distribution is concerned, the LTSA structure is reduced to a non-uniform (tapered) slot line. The aperture distribution of the tapered slot line is determined by considering it as being comprised of short sections of parallel slots of varying widths, connected end to end. The aperture field of a parallel slot line is obtained by employing the spectral Galerkin's technique. For the purpose of radiation pattern computations, it is assumed that the step discontinuity is "soft" enough so as to not result in any

higher order modes of the slot line or in any reflections. A power continuity criterion across the junctions is enforced to determine the amplitude distribution of the tapered structure. The phase distribution (i.e., propagation constant) of the tapered slot line is considered to be the same as that of the stepped approximation (valid for shallow taper angles and when the dielectric substrate is thin enough). The validity of the stepped approximation is verified by comparing the radiation pattern of an air dielectric LTSA obtained using (i) the aperture distribution obtained using the stepped approximation and (ii) the exact aperture distribution for the tapered infinite structure obtained by using a conformal mapping technique. A favorable comparison between the two justifies the stepped approximation model.

Truncation of the aperture results in the edge cbb'c' and as a result, diffraction currents are induced on the metallic portion of the structure. As the slot is extended right onto the edge, the contribution to the radiation pattern due to these induced currents is expected to be quite significant. (Indeed, it is shown in Section II, that the radiation pattern in the E-plane (XZ plane) is entirely due to the edge diffraction). Effects of the dielectric truncation on the radiation pattern of the antenna are ignored. This should be a valid approximation for electrically thin substrates. Near field scattering due to the metallic edge cbb'c' is then rigorously taken into account by treating the slots as radiating in the presence of a conducting half plane.

In section II, we present the theoretical details of the analysis. In section III, computed radiation patterns of LTSAs and CWSAs are discussed at length vis-a-vis experimentally observed ones. Comparison with experiment

has revealed that the theory adequately models the physics of the problem when the lateral dimensions of the LTSA and CWSA are large. However, new trends in the radiation pattern have been observed experimentally, as the lateral dimension D of the antenna is decreased. Lateral truncation effects are more pronounced in the E-plane. These are discussed in detail in section III.

II. FORMULATION OF THE PROBLEM

Fig. 1 shows the geometry of the LTSA and the coordinate system considered. As pointed out in section I, the tapered slot is replaced by a stepped approximation. The field distribution of a uniform slot line is determined by the spectral Galerkin's technique [1,2]. The unknown longitudinal and transverse components of the electric field E_x^s and E_z^s, respectively, are expanded in terms of the basis functions (Tchebycheff polynomials in the present case) as [2]

$$E_x^s = \sum_{m=1}^{M_x} b_m \left(\frac{1}{\pi W}\right) U_{2m-1}\left(\frac{z}{W}\right) \cdot \sqrt{1-\left(\frac{z}{W}\right)^2} \tag{1}$$

$$E_z^s = \sum_{n=0}^{M_z} a_n \left(\frac{1}{\pi W}\right) \frac{T_{2n}\left(\frac{z}{W}\right)}{\sqrt{1-\left(\frac{z}{W}\right)^2}} \tag{2}$$

Where $T_j(\cdot)$ and $U_j(\cdot)$ are Tchebycheff polynomials of the first and the second kind respetively and 2W is the width of the uniform slot. M_x and M_z+1 are the respective number of basis functions used for the x and z directed electric fields. The factor $e^{-jk_x x}$ is suppressed in (1) and (2). k_x is the propagation constant of the line. The a_n's, b_m's and k_x are obtained by solving the eigenvalue equation generated in the spectral Galerkin's technique [2].

The characteristic impedance Z_o for a uniform slot line is defined as [3,4]

$$Z_o = \frac{|V_o|^2}{P_f} \tag{3}$$

where $V_o = \int_{-W}^{W} E_z^s(z)\, dz$ = Voltage across the slot in the y = 0 plane

and P_f is the power flow along the direction of propagation i.e., along the x-axis. For the basis functions chosen, $V_o = a_o$. We therefore have

$$P_f = |a_o|^2 Z_o \tag{4}$$

Equations (1), (2) and (4) are utilized in defining the slot field for the tapered structure. Enforcing the power continuity condition on the stepped structure, we see that the slot field for the i-th section may be defined as

$$E_x^s \Big|_{\text{i-th section}} = \frac{(Z_o^i)^{1/2}}{\pi W_i} \sum_{1}^{M^i} b_m^i\, U_{2m-1}\left(\frac{z}{W_i}\right) \cdot \sqrt{1-\left(\frac{z}{W_i}\right)^2} \tag{5}$$

$$E_z^s \Big|_{\text{i-th section}} = \frac{(Z_o^i)^{1/2}}{\pi W_i} \sum_{0}^{M^i} a_n^i\, \frac{T_{2n}(z/W_i)}{\sqrt{1-(z/W_i)^2}} \tag{6}$$

Where Z_o^i is the characteristic impedance of the slot line with a slot width of $2W_i$. The coefficients a_n^i and b_m^i are normalized such that the impedance dependence of a_o^i as per equation (4) has been explicitly brought out and a_o^i = 1 for any i. The remaining coefficients a_n^i and b_m^i are all defined in terms of a_o^i.

It can be shown following Tai's analysis [5] of infinitesimal slots radiating in the presence of a conducting half plane that the longitudinal slot field E_x^s does not contribute to the far-field in either principal plane. This may be explained intuitively as follows: E_x^s is an odd function of z and hence the far-field due to E_x^s has a null in the plane of symmetry

i.e., XY plane (H-plane). The far-field components in any plane have two terms. The first term may be labelled the direct field ie., field in the absence of the edge cbb'c'. The second term arises as a result of scattering due to the edge cbb'c'. Both the direct field and the scattered field due to E_x^s are polarized normal to the edge i.e., along the y-axis and hence contribute only to the crosspolarized component in the E-plane. Indeed, the only copolar term appearing in the E-plane is due to the radiation of the transverse slot field E_z^s scattering from the edge cbb'c'.

Henceforth we shall be concerned only with E_z^s and shall be referring to it as the aperture distribution E_a. We shall also include the phase term in it. With respect to the coordinate system defined in fig. 1, the aperture distribution E_a^i of the i-th section is given by

$$E_a^i = E_z^s\Big|_{i\text{-th section}} e^{jk_x^i(x'-L)} = \frac{(Z_o^i)^{1/2}}{\pi W_i} e^{jk_x^i(x'-L)} \sum_0^{M_z^i} a_n^i \frac{T_{2n}(z'/W_i)}{\sqrt{1-(z'/W_i)^2}} \quad (7)$$

The primed quantities stand for the source coordinates and

$k_x^i = c^i k_o$ = propagation constant corresponding to the i-th section.

L = total length of the LTSA

For the air dielectric case, we have

$c^i = 1$

$Z_o^1 = \ldots = Z_o^i = Z_o^{i+1} = \ldots = 1$ (by appropriate normalization)

$M_z^i = 0$

$$E_a^i\Big|_{\varepsilon_r = 1.0} = \frac{e^{jk_o(x'-L)}}{\pi W_i} \frac{1}{\sqrt{1-(z'/W_i)^2}} \quad (8)$$

For this case, however, the exact aperture field distribution for a flared infinite structure can be found using a conformal mapping technique [6] and may be shown to be

$$E_a^{exact}\Big|_{\varepsilon_r=1} = \frac{e^{-jk_o\eta'}}{\eta'} \quad \frac{\cos\xi'}{\sqrt{\tan^2(\frac{\gamma}{2}) - \tan^2(\frac{\xi'}{2})}} \tag{9}$$

where (η',ξ') are the polar coordinates in the plane of the slot with the vertex of the LTSA at the origin and 2γ is the flare angle of the LTSA. The LTSA width $W(x')$ and the flare angle γ are related as $W(x') = (L-x')\tan\gamma$. For shallow flare angles,

$$\tan(\frac{\gamma}{2}) \simeq \frac{1}{2}\tan\gamma$$

$$\tan(\frac{\xi'}{2}) \simeq \frac{1}{2}\tan\xi'$$

$\eta' \simeq (L-x')$ in the amplitude part of (9)

$\cos\xi' \simeq 1.0$

$$\frac{\tan(\frac{\xi'}{2})}{\tan(\frac{\gamma}{2})} \simeq \frac{\tan\xi'}{\tan\gamma} = \frac{z'}{W(x')}$$

Therefore $$E_a^{exact}\Big|_{\varepsilon_r = 1} \simeq \frac{2e^{-jk_o\eta'}}{W(x')} \quad \frac{1}{\sqrt{1-[z'/w(x')]^2}} \tag{10}$$

We notice from equations (10) and (8) that E_a^{exact} and E_a^i have the same functional form except that the radial wave in (10) is replaced by a plane wave in (8). This minor difference is expected to influence only the far out angles off the end-fire for LTSAs with shallow taper angles.

Following Tai's [5] analysis of infinitesimal slots in the presence of a conducting half plane, it can be shown that the far-field component of the electric field due to an infinitesimal horizontal slot (i.e., z directed electric field) is (for the coordinate system shown in fig. 1)

$$E_\theta^\delta = e^{jk_o(x'\sin\theta\cos\phi+z'\cos\theta)} \sqrt{|\sin\phi|}\, e^{j\pi/4} F(v) + \frac{e^{-j\pi/4}}{\sqrt{\pi k_o x'\sin\theta}}\, e^{-jk_o(x'\sin\theta-z'\cos\theta)} \cdot \sin\left(\frac{\phi}{2}\right), \quad \theta \neq 0, \pi \tag{11}$$

where $v = k_o x'\sin\theta(\cos\phi+1)$

and $F(v) = \int_0^v \frac{e^{-jt}}{\sqrt{2\pi t}}\, dt$ (Fresnel Integral)

Note that

$$\lim_{v\to\infty} e^{j\pi/4} F(v) \to \frac{1}{\sqrt{2}} \tag{12}$$

We observe from equation (11) that the magnitude of the second term decays to zero as $k_o x' \to \infty$ ($\theta \neq 0, \pi$, since the asymptotic expression is not valid for $\theta = 0, \pi$) and that E_θ^δ is dominated by the first term which, in this case, reduces to the familiar far field expression due to a slot in an infinite ground plane. We may consequently interpret the first term as the 'direct field' and the second term as the 'edge diffraction field'.

In the E-plane, $\phi = 0, \pi$ and the first term vanishes, as it should for a slot in an infinite ground plane. The E-plane pattern is hence governed entirely by the edge diffracted field.

The far-field components due to the i-th section are obtained by integrating (7) over the i-th aperture with E_θ^δ as the kernel. Integration over z' with E_θ^δ as the kernel may be recognized as the Fourier transform (w.r.t. z') of the aperture distribution (7) and is known in closed form for the basis functions chosen. Integration over x' can also be effected in a

closed form over each individual parallel section. Radiation from the LTSA is finally obtained by summing the far-fields from all sections.

III. DISCUSSION OF COMPUTED AND EXPERIMENTAL RESULTS

Using the foregoing theory, radiation patterns have been computed for LTSAs and CWSAs with $\varepsilon_r = 1.0$, $\varepsilon_r = 2.22$ (substrate thicknesses d/λ_o of 0.015, 0.02, 0.058) and $\varepsilon_r = 2.55$ ($d/\lambda_o = 0.04$) for lengths varying over $3.0 \leq L/\lambda_o \leq 9.6$ and flare angles varying over $8^o \leq 2\gamma \leq 21^o$.

The aperture distribution given in equation (7) includes only the forward travelling wave. It is expected that the truncation of the structure to length L will alter the aperture distribution, at least by introducing a reflected wave. To study the effects of the reflected wave on the radiation pattern, a reflected wave was included in the aperture distribution and the voltage reflection coefficient R was varied over $-1 \leq R \leq 1$. Patterns were computed for various combinations of L, 2γ and ε_r. It was found that for a long antenna the reflected wave affected the pattern only at angles far away from the end-fire direction and had little influence on the forward lobe. The front lobe is almost entirely decided by the forward travelling wave. Figs. 2a and 2b show the typical behaviour observed in the pattern by including a reflected wave in the aperture distribution. Patterns are shown for an LTSA with $2\gamma = 10^o$ and $L/\lambda_o = 3$ and 10 respectively, with R as a parameter. It is seen that the effect of the reflected wave on the front lobe is not very critical and diminishes as the length of the antenna is increased. In all the subsequent patterns, only a forward wave as defined in (7) is considered for the aperture distribution. Notice that the cases of $R = \pm 1$ correspond to a uniform phase distribution on the aperture (i.e., a pure standing wave on the slot) and would have resulted in a broadside pattern (i.e., maximum along the y-axis) had the slot been radiating in free space. However, currents are induced on the

metalization as a result of near-field scattering off the edge cbb'c'. These induced currents radiate with a maximum in the endfire direction as evidenced by the second term in equation (11). The radiated fields of the LTSA are dominated by those produced by the induced currents and this is clear from the end-fire nature of the H-plane patterns as shown in figs. 2a and 2b.

Fig. 3a and 3b show the comparison for the E-plane pattern obtained by using the exact aperture distribution given by equation (9) and the stepped approximation given in (8) for $\varepsilon_r = 1.0$, $2\gamma = 15^\circ$ and $L/\lambda_o = 6.3$. It was found that five steps per wavelength gave convergent results on the radiation pattern. In figure 3b, five steps per wavelength have been chosen. The favorable comparison between the two justifies the use of the stepped approximation model in determining the aperture distribution for air dielectric LTSA. The stepped approximation should be valid also for $\varepsilon_r > 1$ antennas. In all the subsequent computations, five steps per free space wavelength have been chosen to model the continuous taper.

The computed patterns in the E and H planes for an air dielectric LTSA are shown in fig. 4a. Corresponding experimental patterns are shown in figs. 4b and 4c. Comparison is shown for L = 19.0 cm, $2\gamma = 15^\circ$ and f=8.0 GHz. The experimental model was built using a 5 mil brass sheet with D=11.0 cm. A microwave diode (HP-5082-2215) was connected across the feed terminals to detect the RF signal. The antenna was supported by using 1/2" styrofoam ($\varepsilon_r = 1.02$) strips along the outer boundary. Table 1 summarizes the comparison between the two. A similar agreement between the theory and experiment was obtained on other LTSAs over the range $8^\circ \leq 2\gamma \leq 21^\circ$ and $3 \leq L/\lambda_o \leq 9.6$. In all these cases, the LTSA height D satisfied $D \geq 2.75\ \lambda_o$ and $D/W_o \geq 3.3$,

where $W_o = L \tan\gamma$. The ripples observed in the experimental E-plane pattern are due to finite D as will be discussed shortly. A summary of the comparison of the 3 dB beamwidth between the theory and experiment over the above range of taper angles is shown in figs. 4d and 4e for $L/\lambda_o = 5$ and 6.33 respectively. It is seen that the agreement between the two is very good.

Figs. 5a-5d show the computed and experimental patterns for an LTSA on $\varepsilon_r = 2.55$ and with d = 1.6 mm $2\gamma = 11.4^o$ L = 22.7 cm, f = 8.0 GHz. The computed patterns have been calculated using the slot line data obtained via the spectral Galerkin technique. The experimental model was built with D = 9.7 cm. Table 2 summarizes the comparison and it is seen that the agreement between the two is quite good. Note that we have $D/\lambda_o = 2.6$ and $D/W_o = 4.28$ and the substrate is thick ($d/\lambda_o = 0.043$).

It is expected that the theoretical model considered would correctly predict both the E and the H-plane patterns for a large D (it may be recalled that the model assumes that $D \to \infty$) and this has indeed been demonstrated by comparing theory with experiment for LTSAs on $\varepsilon_r = 1.0$ for which both the amplitude and phase of the dominant term (i.e., the TEM wave) of the aperture distribution can be determined exactly. However, it has been observed experimentally that the lateral truncation of the LTSA and CWSA has a pronounced effect on the radiation pattern, particularly in the E-plane, as the height D begins to decrease and approach W_o. Ripples appear in the E-plane pattern (as seen in fig. 4b) even for moderate D. The E-plane beam narrows as D is decreased, reaching a minimum value before beginning to broaden again. The H-plane beam, while being less sensitive to D initially and having a low backlobe, begins to broaden with the backlobe

becoming more prominent. Both the E-plane and the H-plane patterns develop a large backlobe and a poorly defined front lobe as D approaches W_o. Experimental patterns in both the E-plane and the H-plane for various values of D ranging between 2.5 cm $\leq$ D $\leq$ 15.24 cm are shown in Appendix A (Figs. A1-A7) for an air dielectric LTSA at 9.0 GHz with L = 24 cm and $\gamma = 5.9^o$. Figs. 6 and 7 summarize the results of the effect of lateral truncation on the beamwidths (3 dB and 10 dB) of an air dielectric LTSA ($2\gamma = 11.8^o$) in the E and H-plane respectively for L/λ_o = 6.4, 7.2 and 8.0. In figs. 6a and 7a beamwidths are plotted as a function of D/λ_o, whereas in figs. 6b and 7b, beamwidths are plotted as a function of W_o/D. It is seen from figs. 6b and 7b that the curves approach the theoretical values as $W_o/D \to 0$. Clearly the H-plane beam is less sensitive to the lateral truncation for sufficiently large D and it is felt that the success of the foregoing analysis with infinite D would be better evidenced in the H-plane.

Figs. 8a-8d show the computed and experimental patterns of a CWSA with ϵ_r = 2.22, d/λ_o = 0.017, $2W/\lambda_o$ = 0.67, L/λ_o = 4.2. The tapered portion was modeled by the stepped approximation. Experiments were conducted on a 20-mil RT Duroid 5880 substrate at X-band with W = 1.0 cm and D = 5.0 cm. It is seen that there is a lot of discrepancy between the two in the E-plane. The calculated 3 dB beamwidth of 42^o is twice the experimental value of 21^o. The theoretical 3 dB beamwidth and the locations of the first minimum in the H-plane, differ from experimental ones by about 25%. The H-plane pattern of a CWSA is governed primarily by the wavelength ratio c ($= k_x/k_o = \lambda_o/\lambda'$) and the length of the antenna. (The antenna departs from behaving as a pure surface wave linear antenna in the H-plane in that the diffraction due to the edge cbb'c' narrows the H-plane beam noticeably hence the use of the

term primarily in the above sentence. In other words, the radiation pattern of the slot antenna has a narrower main beam in the H-plane than an equivalent wire antenna of the same length and having the same dispersion characteristic. Currents induced on the metalization due to the edge cbb'c' tend to narrow the beam of the purely surface wave antenna.) It may be recalled that the pattern of a surface wave antenna is highly sensitive to 'c' due to the phase accumulation of the wave as it progresses along the structure. (Typically the beam width changes by about 20% for a 2-3% change in 'c' for a $4\lambda_o$ long antenna). The slot line wavelength as determined by the spectral Galerkin's method is only within 2-2.5% of the measured value as reported in [1] and this is expected to influence the radiation pattern. The measured normalized wavelength for a slot line with the above parameters was found to be 0.952 at 10 GHz compared to the computed value of 0.978 i.e., differing by 2.7%. The pattern of the CWSA computed using the measured value of c is shown in figs. 9a and 9b. Table 3 shows the comparison between theory and experiment with and without the correction factor for c. It is seen that there is good agreement in the H-plane between the experiment and the theory based on the measured value of c. The discrepancy in the E-plane is attributed to the lateral truncation effects. However, for the thick substrate case ($d/\lambda_o = 0.043$) shown in fig. 5, a good agreement with experiment is obtained for pattern computations based on the calculated slot wavelength. Patterns corresponding to the CWSA at another frequency (8.0 GHz) are plotted in Appendix B. (figs. B1-B4)

Figs. 10a and 10b show the computed H-plane patterns of an LTSA with $\varepsilon_r = 2.22$, $d/\lambda_o = 0.017$, $2\gamma = 10^o$, $L/\lambda_o = 4.2$at 10 GHz. In fig. 10a, the computed slot wavelength is used whereas, in fig. 10b, the correction factor

of 2.7%, as discussed above is used over the entire length. Experiments were conducted on a 20-mil Duroid substrate and D was set equal to 10 cm. Fig. 11d shows the experimentally observed pattern. Table 4 summarizes the comparison. Once again a very good agreement between theory and experiment is obtained when the correction factor of 2.7% for c is used. The respective E-plane patterns are plotted in figs. 11a, 11b and 11c. We see from Table 4 that there is a good agreement in the E-plane too and this is expected since D is large in this case, i.e., $D/W_o = 10.0$ and $D/\lambda_o = 3.33$. However, the presence of ripples on the main beam seems to suggest that the lateral truncation effects are not totally absent. Similar trends in agreement have been found at other frequencies over the X-band. Comparison at 8.0 GHz may be made from figs. 12a-12f. Additional experimental plots showing the dependence of patterns on D are plotted in Appendix B. Patterns are shown at both 8.0 GHz and 10 GHz. (B5-B19)

An LTSA on a substrate with $\varepsilon_r > 1$ radiates all along its length because the propagation constant and characteristic impedance of the slot line change with slot width. In contrast, a CWSA radiates only from the feed and terminal discontinuities as in the case of uniform dielectric rod antennas. A forward travelling wave on a CWSA radiates primarily due to the terminal discontinuity (edges bc and b'c'). We may therefore anticipate that the lateral truncation effects are more severe in a CWSA than in an LTSA with the same height and and length. To verify this notion, we may compare the E-plane patterns of the CWSA shown in Figs. 8 and 9 with the E-plane patterns of the LTSA shown in Fig. B16. Both the antennas have approximately the same length $L/\lambda_o = 4.2$ and height $D/\lambda_o = 1.67$ (corresponding $D/W_o = 5$) at 10 GHz. It is seen that the discrepancy with

respect to the theory in the 3dB beamwidth is ≈ 100% in the case of CWSA and only 65% in the case of a LTSA. Comparison in other cases showed the same effect.

IV. CONCLUSION

Traveling wave slotline antennas have been analyzed in two steps. In the first step, a wide uniform slot line is analyzed using a spectral Galerkin's technique (i.e., wavelength, characteristic impedance and the slot fields are obtained). The LTSA is approximated by a stepped model consisting of short sections of uniform slot line. Data on the uniform slot line are utilized in determining the aperture distribution of the stepped structure with a power continuity criterion employed at the step junction of two adjacent sections. In the second step, the radiated field is obtained by using a rigorous theory of slots radiating in the presence of a conducting half plane to account for the important near field scattering due to the edge of the conductor at the aperture and the far field components are obtained.

Numerous experiments were conducted on LTSAs and CWSAs over the range of parameters $3.0 \leq L/\lambda_o \leq 9.6$, $8° \leq 2\Upsilon \leq 21°$ and $\varepsilon_r = 1.0, 2.22, 2.55$. L and 2Υ are the length and the flare angle of the LTSA. Comparison between theory and experiment has indicated that the theory adequately models the physics of the problem and predicts the radiation pattern of the antenna with sufficient accuracy if the wavelength of the slot line is known accurately (more accurately than the present 2 1/2% discrepancy between the computed and measured values) and the height D of the antenna is large enough ($D \geq 2.5\lambda_o$ and $D/W_o \geq 5$).

A systematic experimental study has, however, revealed that the radiation pattern of the antenna is sensitive to the height D of the antenna when it is no longer large. In particular, lateral truncation of the LTSA

can result in narrower beams in the E-plane than those obtained with infinite D. The H-plane pattern is initially insensitive to D but eventually broadens as D is decreased. Both E and H plane patterns deteriorate and are poorly defined as D begins to approach W_o. There is a range of D over which the antenna exhibits the narrowest E-plane beam and a satisfactory H-plane pattern. Clearly, D is one of the critical parameters in the design of LTSAs and CWSAs. It is therefore desirable to include truncation effects (i.e., finite D) in the theory. Work is presently ongoing in treating this.

Table 1

Comparison of pattern between theory and experiment for an air dielectric LTSA

$L = 19.0$ cm; $f = 8.0$ GHz; $2\gamma = 15^{\circ}$

	3 dB Beamwidth (deg)		10 dB Beamwidth (deg)		SLL(dB)		Location of the first Minimum	
	Theory	Exp	Theory	Exp	Theory	Exp	Theory	Exp
E-Plane	37.4	34.2	53.4	55	-15	-13	42	35
H-Plane	46.5	45.5	64	70	-10	- 9	35	42

Table 2

Comparison of pattern between theory and experiment for an LTSA

$L = 22.7$ cm; $\varepsilon_r = 2.55$; $d = 0.16$ cm
$2\gamma = 11.4^{\circ}$
$f = 8.0$ GHz

	3 dB BW($^{\circ}$)		10 dB BW ($^{\circ}$)		SLL(dB)		Location of the first minimum	
	Theory	Exp	Theory	Exp	Theory	Exp	Theory	Exp
E-Plane	25	26.5	40	51	-17.2	-18	35	37
H-Plane	21	24.6	NA	NA	- 6.5	- 6	20	20

Table 3

Comparison of pattern between theory and experiment for a CWSA

$L/\lambda_o = 4.2$, $\varepsilon_r = 2.22$, $d/\lambda_o = 0.017$, $2W/\lambda_o = 0.67$

	3 dB BW(°)			SLL(dB)			Location of the first Minimum		
	Theory Using Computed 'c' (c_{th})	Theory Using Measured c (c_{meas})	Exp	Theory Using c_{th}	Theory Using c_{meas}	Exp	Theory Using c_{th}	Theory Using c_{meas}	Exp
E-plane	42	38	21	-11.5	-11	-12	36	33	34
H-plane	40	32	32	- 9	- 8	- 9	33	28	27

Table 4

Comparison of pattern between theory and experiment of an LTSA

$L/\lambda_o = 4.2$ $\varepsilon_r = 2.22$; $d/\lambda_o = 0.017$

$2\Upsilon = 10^o$

	3 dB BW(°)			SLL(dB)			Location of the first Minimum		
	Theory Using Computed 'c' c	Theory Using Measured c	Exp	Theory Using c_{th}	Theory Using c_{meas}	Exp	Theory Using c_{th}	Theory Using c_{meas}	Exp
E-plane	45.6	40	38	-13	-12	-10	38.6	36	32
H-plane	42.7	34.5	30	-11.5	-10.5	-10.5	36	31	30

References

[1] T. Itoh and R. Mittra, "Dispersion Characteristics of Slot Lines," Electron. Lett., Vol. 7, pp. 364-365, July 1971.

[2] R. Janaswamy and D.H. Schaubert, "Dispersion Characteristics for Wide Slot Lines on Low Permittivity Substrates," IEEE Trans. Microwave Theory and Tech., Vol. MTT-33, No. 8, pp. 723-726, Aug. 1985.

[3] R. Janaswamy and D.H. Schaubert, characteristic impedance of a Wide Slot Line on low Permittivity Substrates," submitted to the IEEE Trans. Microwave Theory and Tech. for publication.

[4] J.B. Knorr and K. Kuchler, "Analysis of Coupled Slots and Coplanar Strips on Dielectric Substrate," IEEE Trans. Microwave Theory and Tech., Vol. MTT-23, No. 7, pp. 541-548, July 1975.

[5] C. T. Tai, Dyadic Green's Functions in Electromagnetic Theory, Intext Educational Pub. Scranton, Pennsylvania, 1971.

[6] R.L. Carrel, "The Characteristic Impedance of Two Infinite Cones of Arbitrary Cross Section," IRE Trans. Antennas Propagat., Vol AP , pp. 197-201, April 1958.

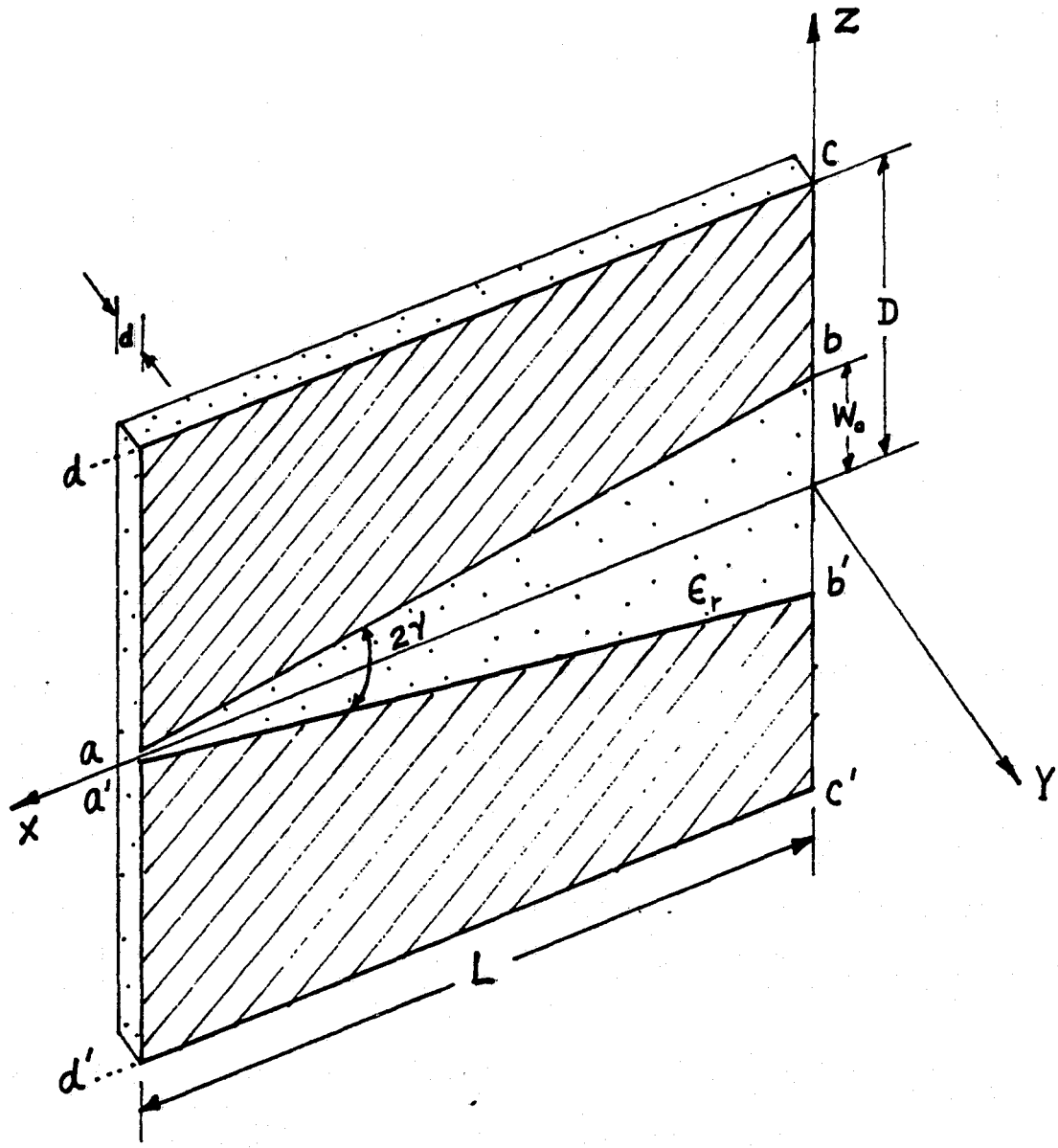

Fig. 1. Geometry of the LTSA and the coordinate system.

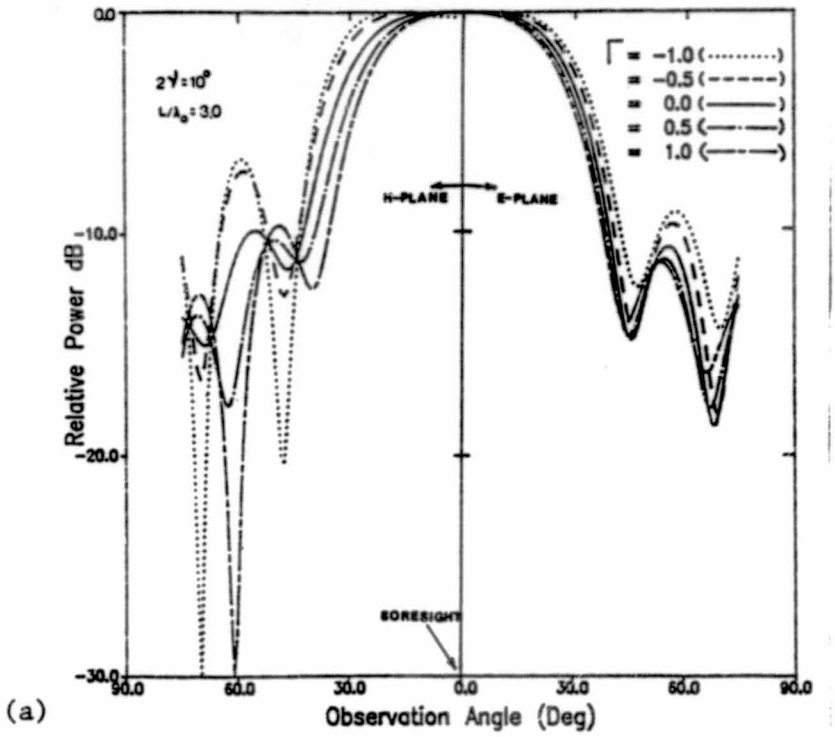

(a)

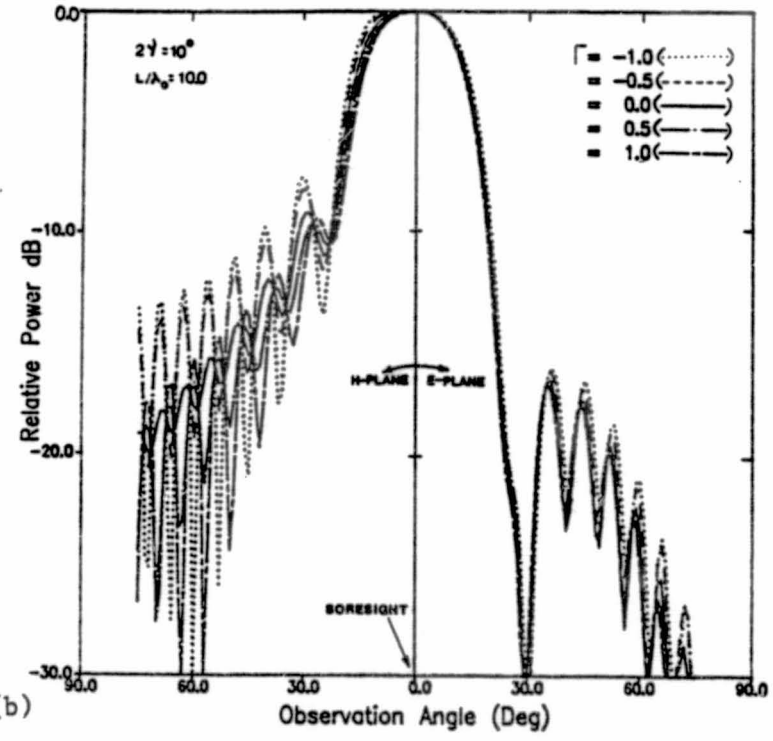

(b)

Fig. 2. Effect of the reflected wave on the radiation pattern of air dielectric LTSA . a) $L/\lambda_o = 3.0$ b) $L/\lambda_0 = 10.0$

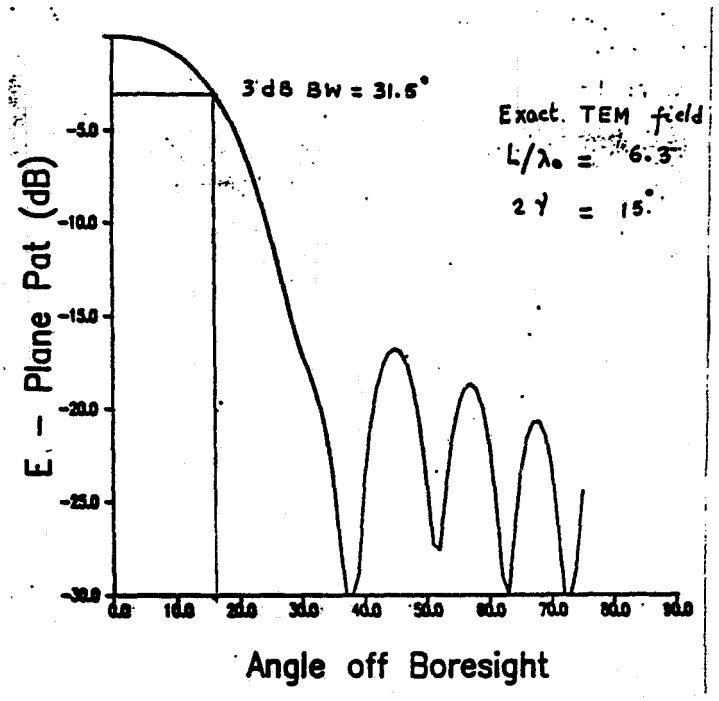

(a)

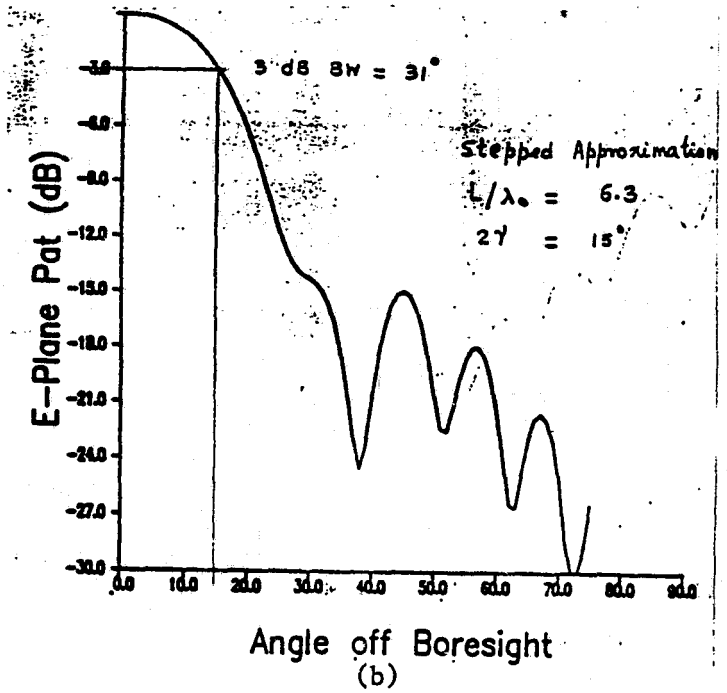

(b)

Fig. 3. Radiation Pattern of an Air Dielectric LTSA obtained by using a) the exact Aperture Distribution b) the Aperture Distribution determined by the Stepped Approximation.

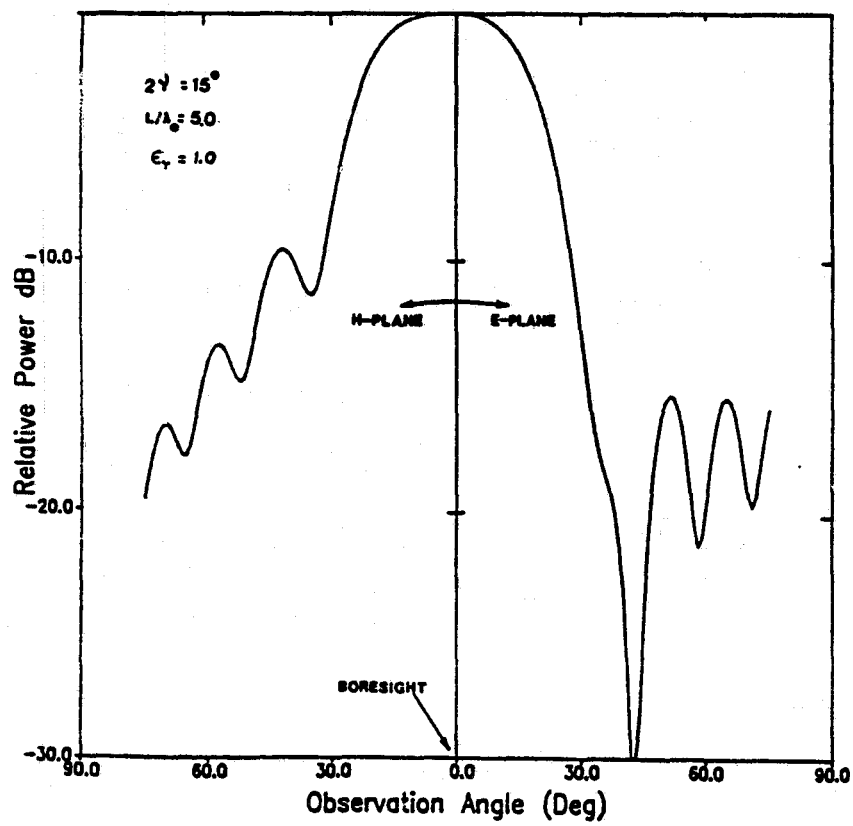

(a)

Fig. 4. Comparison of the radiation pattern between the theory and experiment for an air dielectric LTSA with $L/\lambda_0 = 5.0$; $2\gamma = 15$. a) Theory b) Experiment (E-Plane) c) Experiment (H-Plane)

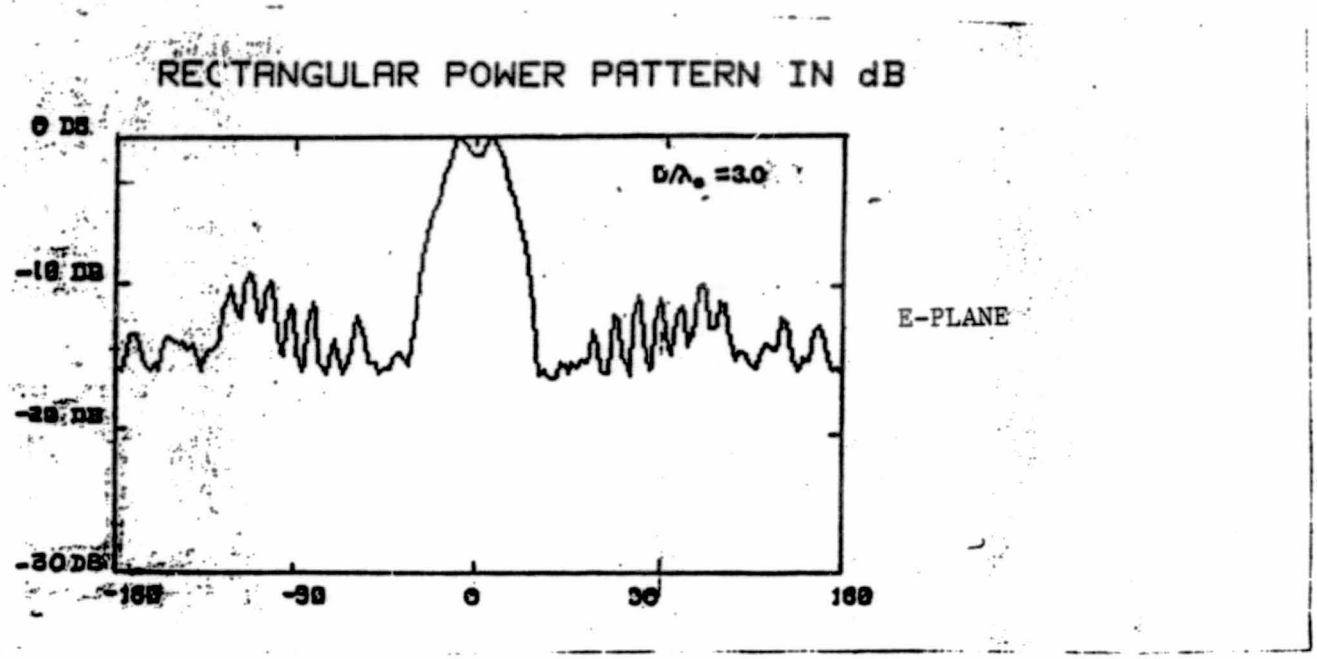

(b)

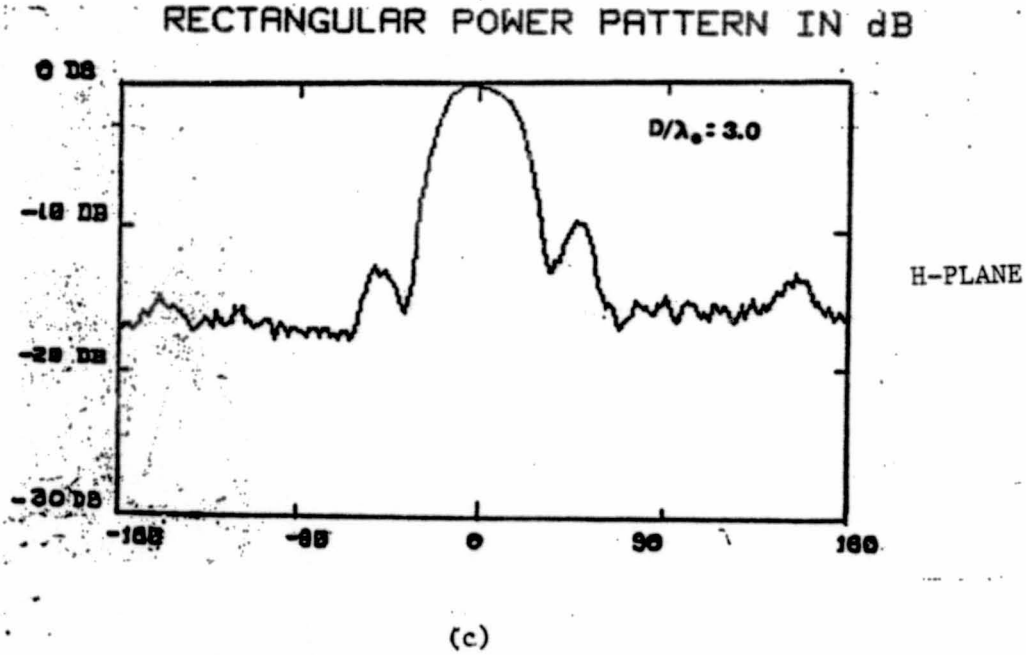

(c)

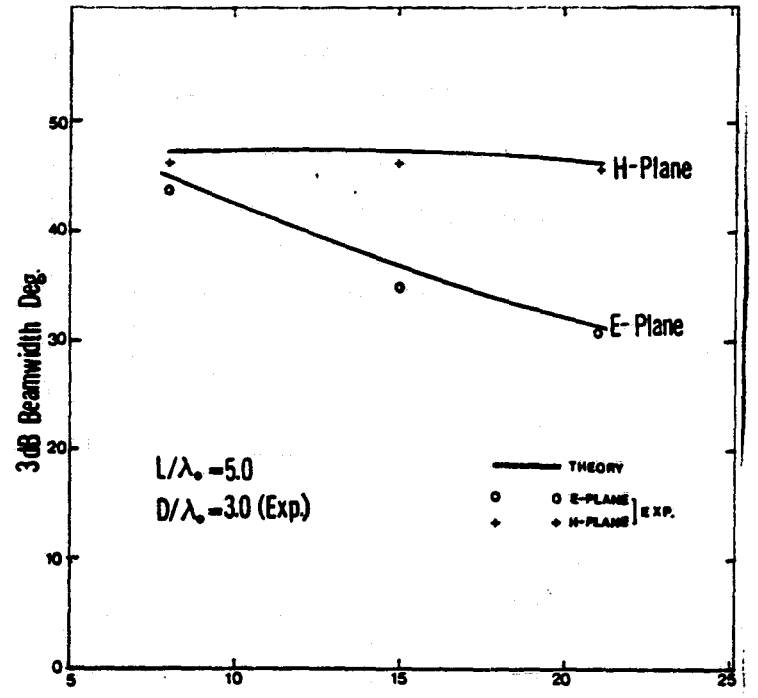

(d)

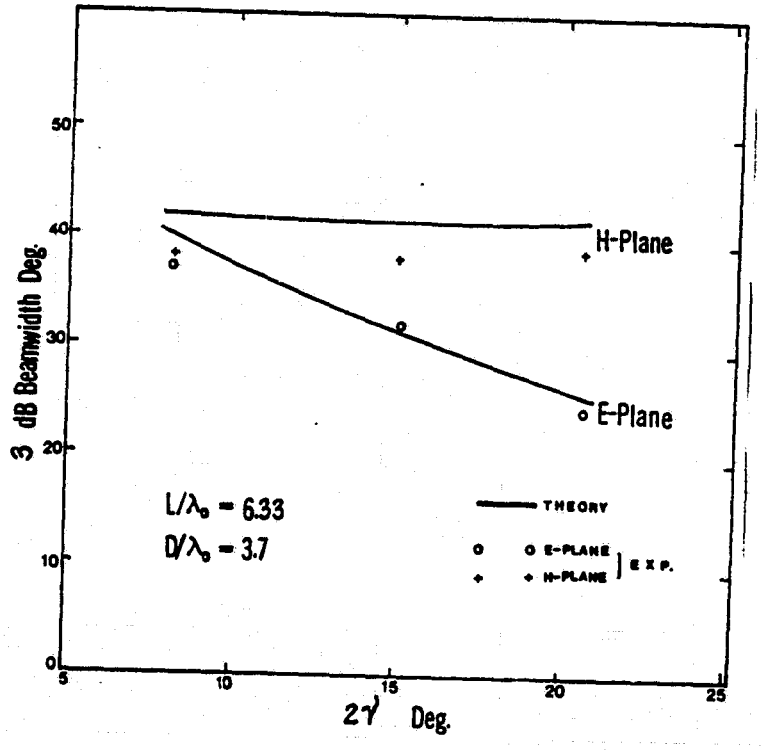

(e)

Fig. 4. Comparison of the 3 dB beamwidth between the theory and experiment over $8 < 2\gamma < 21$.
d) $L/\lambda_0 = 5.0$
e) $L/\lambda_0 = 6.3$

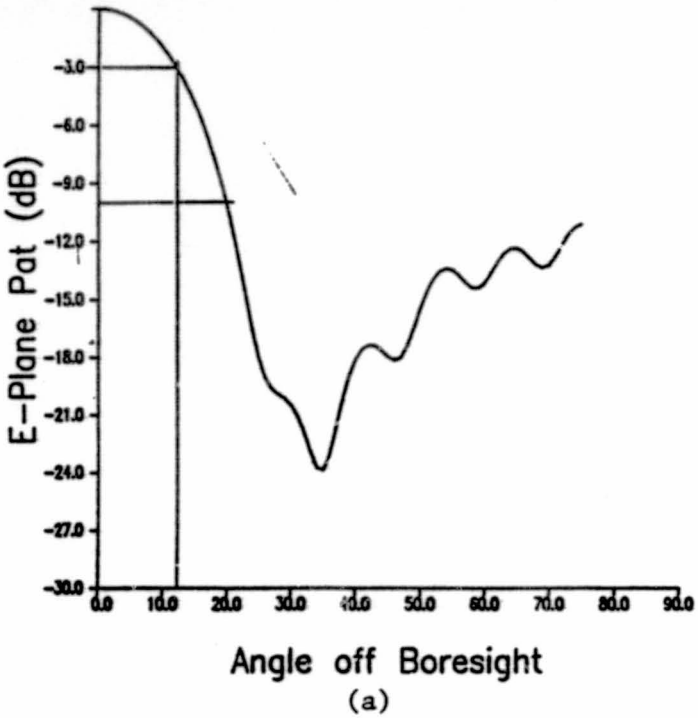

(a)

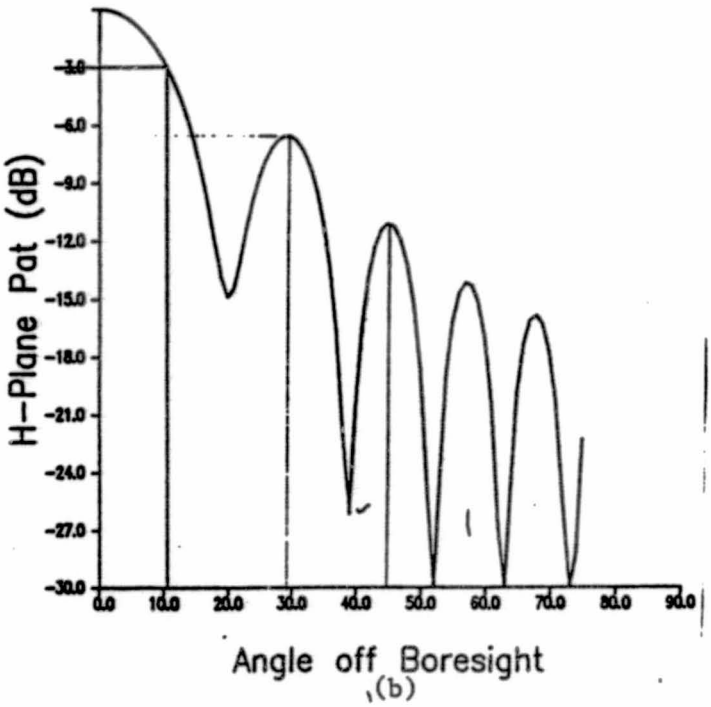

(b)

Fig. 5. Comparison of the radiation pattern between the theory and experiment for an LTSA with $L/\lambda_0 = 6.0$; $2\gamma = 11.4^\circ$; $\varepsilon_r = 2.55$ and $d/\lambda_0 = 0.043$. a) Theory (E-Plane) b) Theory (H-Plane) c) Experiment (E-Plane) d) Experiment (H-Plane)

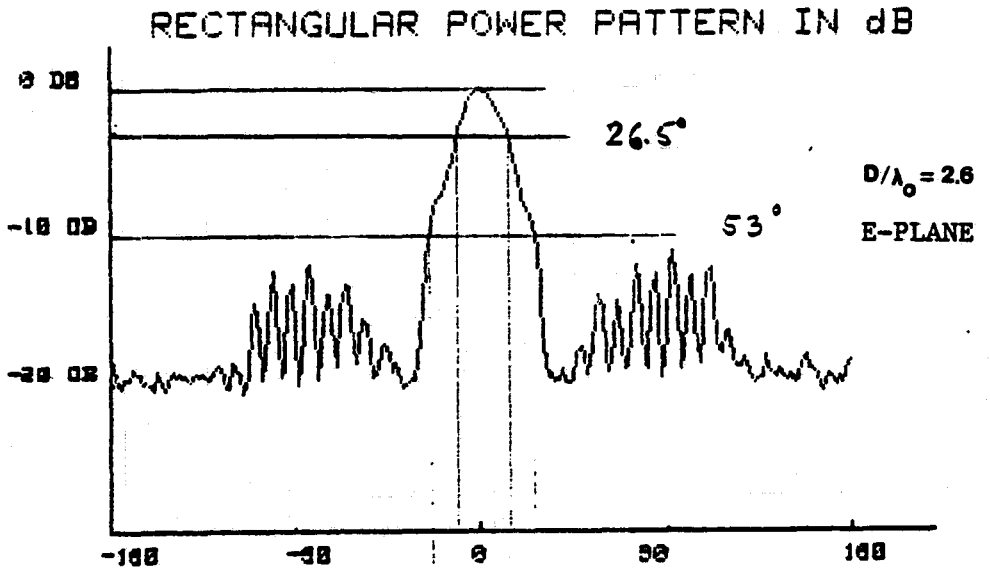
RECTANGULAR POWER PATTERN IN dB
0 DB
-10 DB
-20 DB
26.5°
53°
D/λ0 = 2.6
E-PLANE
-180
-90
0
90
180

(c)

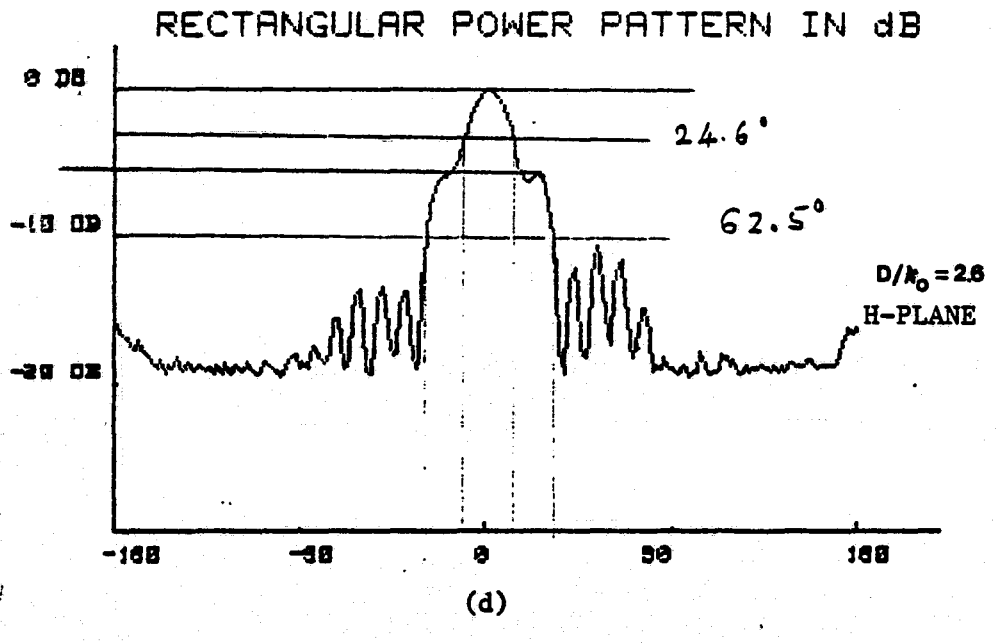
RECTANGULAR POWER PATTERN IN dB
0 DB
-10 DB
-20 DB
24.6°
62.5°
D/λ0 = 2.6
H-PLANE
-180
-90
0
90
180

(d)

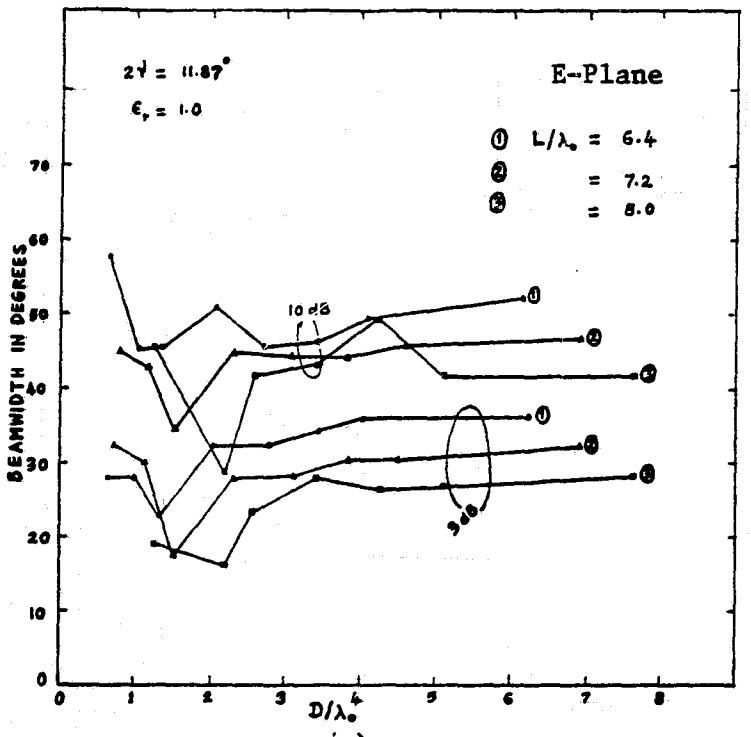

(a)

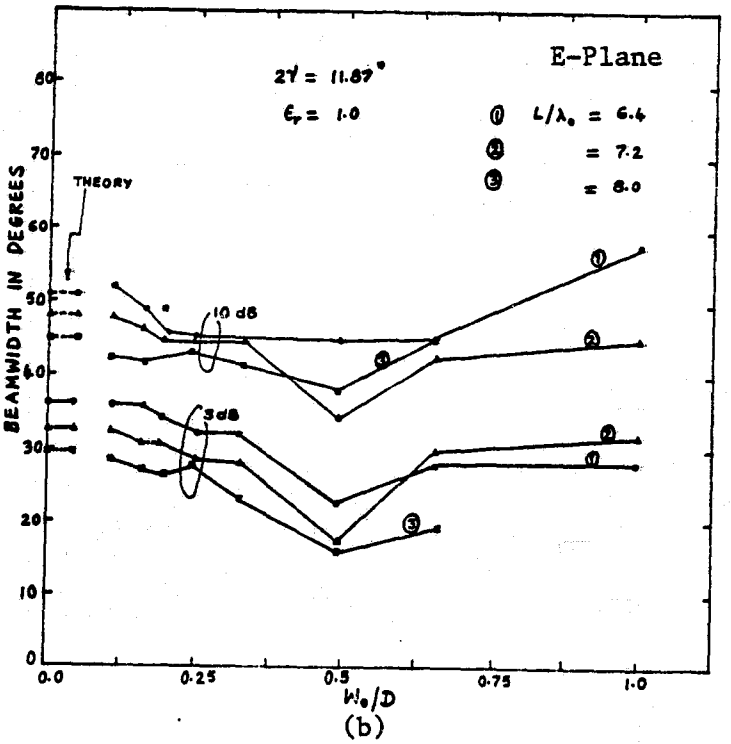

(b)

Fig. 6. Effect of the lateral truncation of the antenna on the E-Plane beamwidth of the air dielectric LTSA.
(a) Beamwidth vs D/λ_0 (b) Beamwidth vs W_0/D

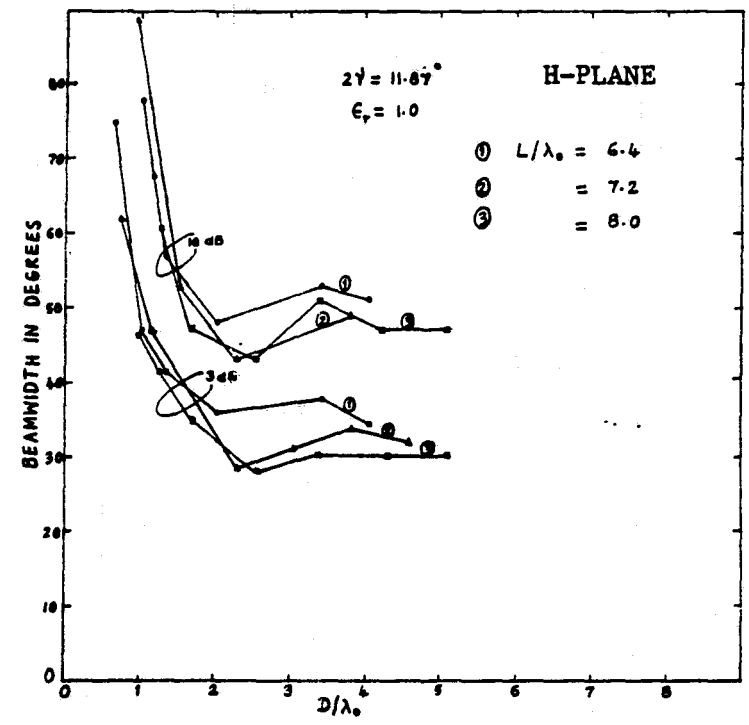

(a)

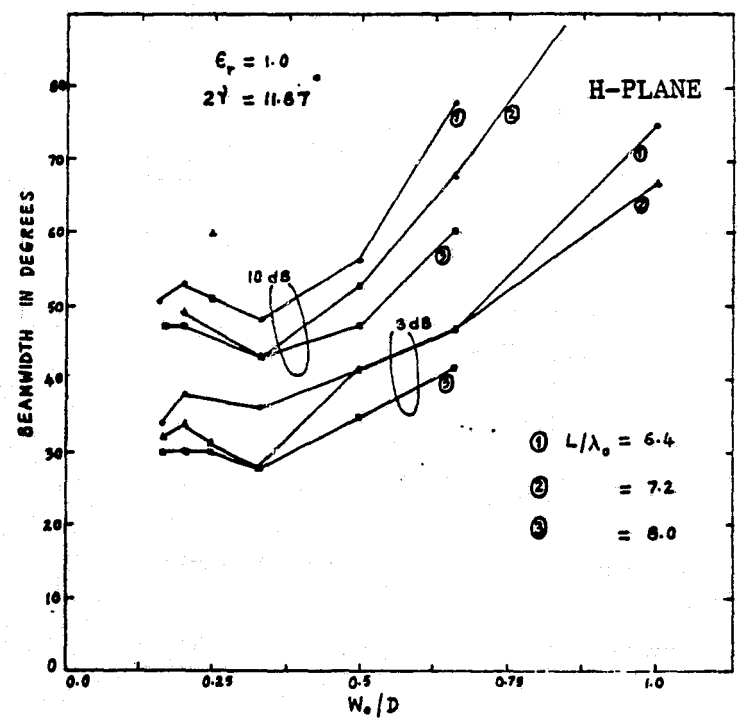

(b)

Fig. 7. Effect of the lateral truncation of the antenna on the H-Plane beamwidth of the air dielectric LTSA.
(a) Beamwidth vs D/λ_0 (b) Beamwidth vs W_0/D.

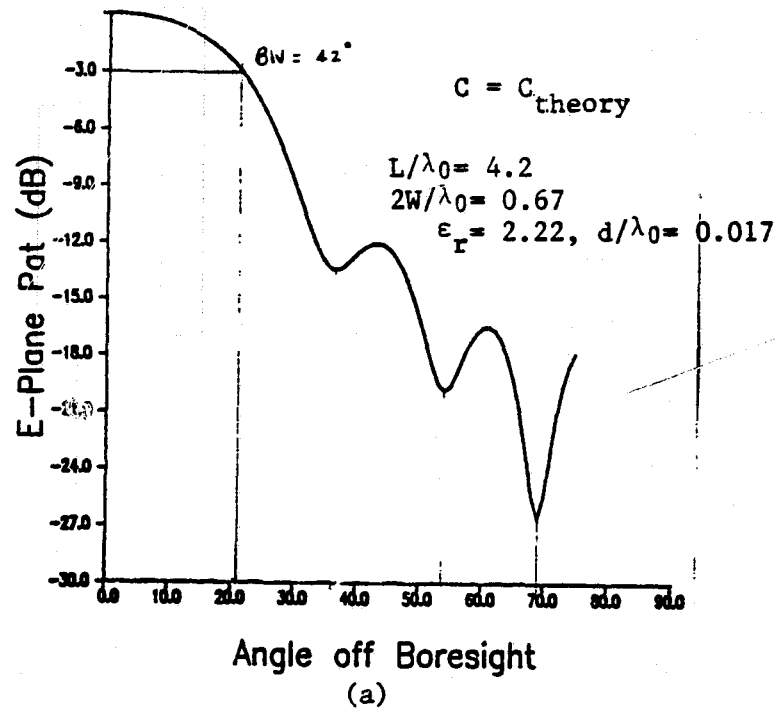

(a)

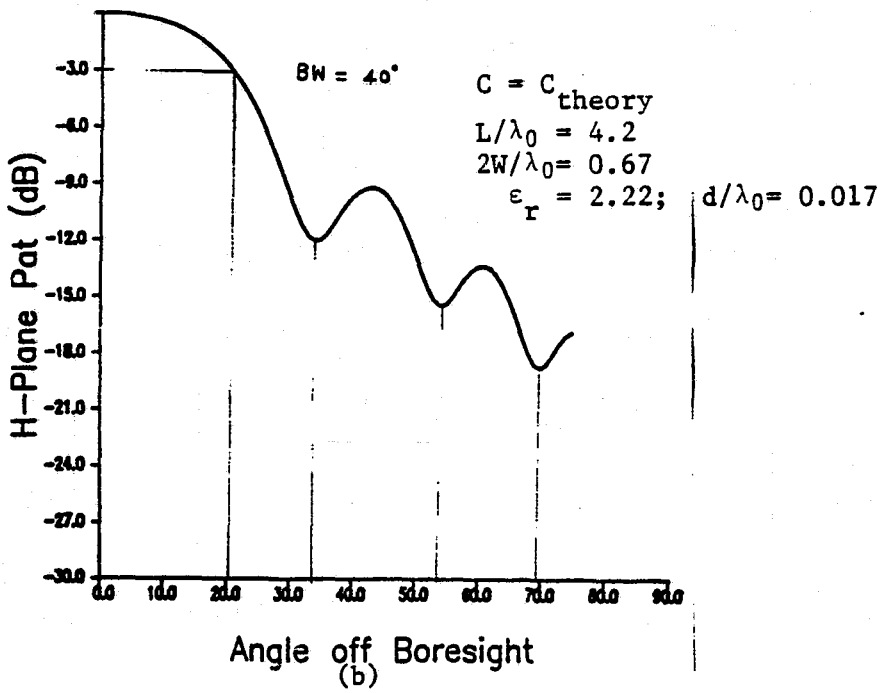

(b)

Fig. 8. Comparison of the radiation pattern between the theory and experiment. a) Theory (E-Plane) b) Theory (H-PLane) c) Exp. (E-Plane) d) Exp. (H-Plane)

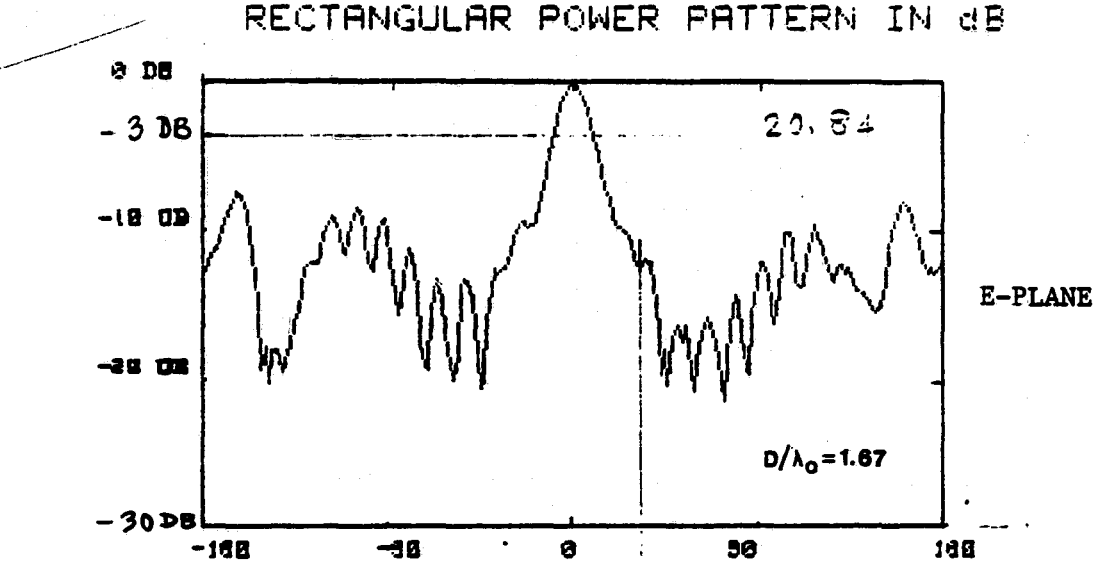
RECTANGULAR POWER PATTERN IN dB
0 DB
- 3 DB
-10 DB
-20 DB
-30 DB
20.84
E-PLANE
D/λo=1.67
-180
-90
0
90
180

(c)

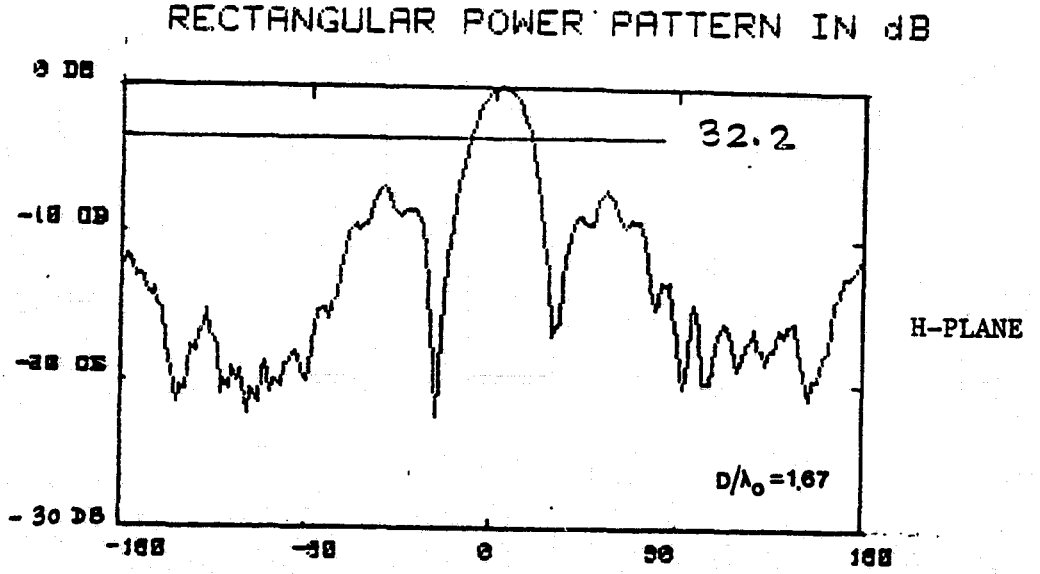
RECTANGULAR POWER PATTERN IN dB
0 DB
-10 DB
-20 DB
-30 DB
32.2
H-PLANE
D/λo=1.67
-180
-90
0
90
180

(d)

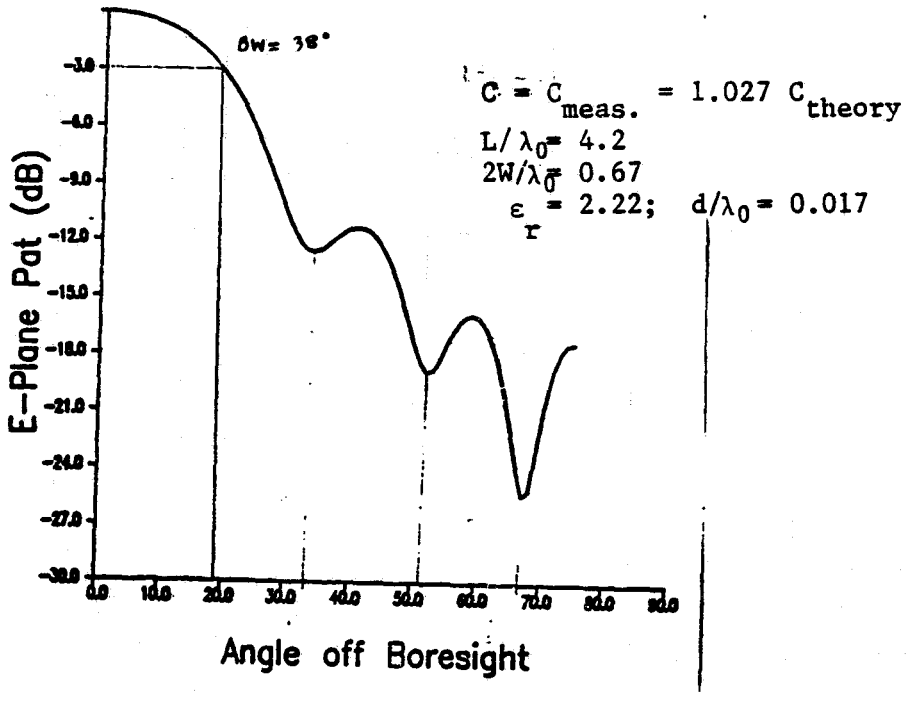

(a)

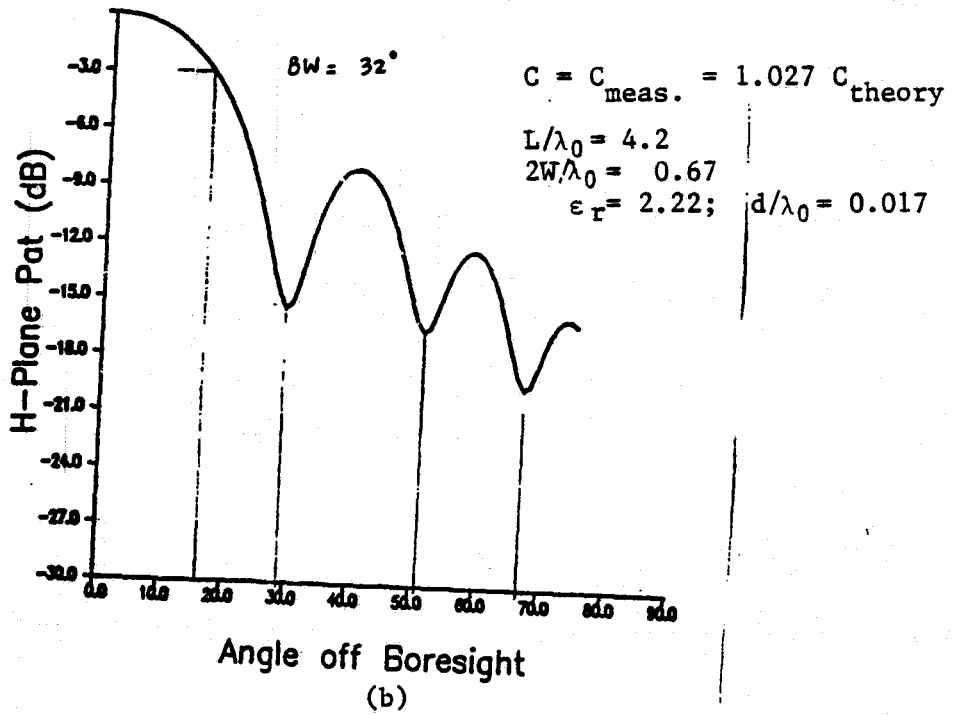

(b)

Fig. 9. Computed radiation pattern of the CWSA using the measured slot wavelength. a) E-Plane b) H-Plane.

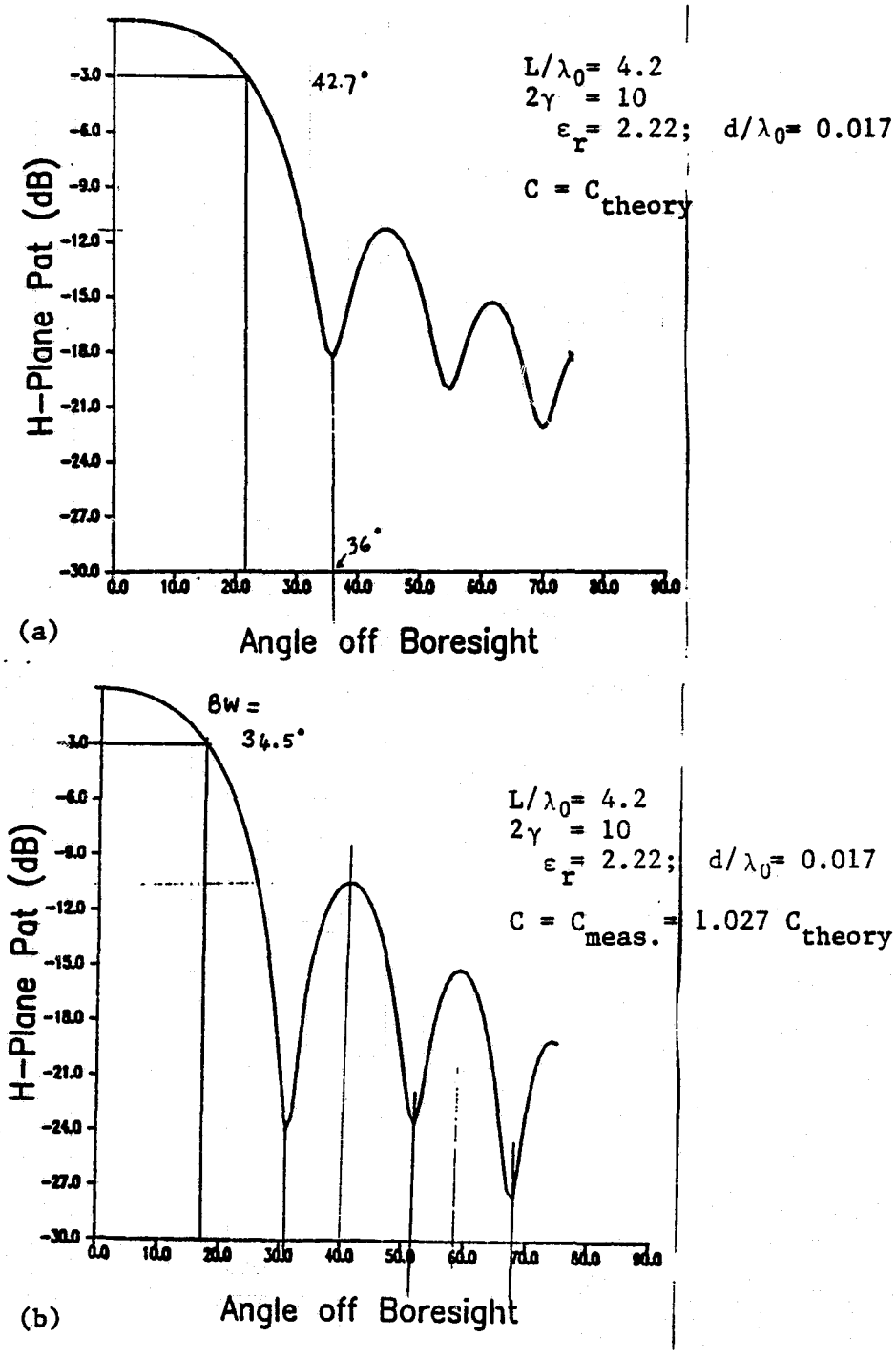

Fig. 10. Computed H-Plane pattern of LTSA using
a) Computed slot wavelength
b) Measured slot wavelength

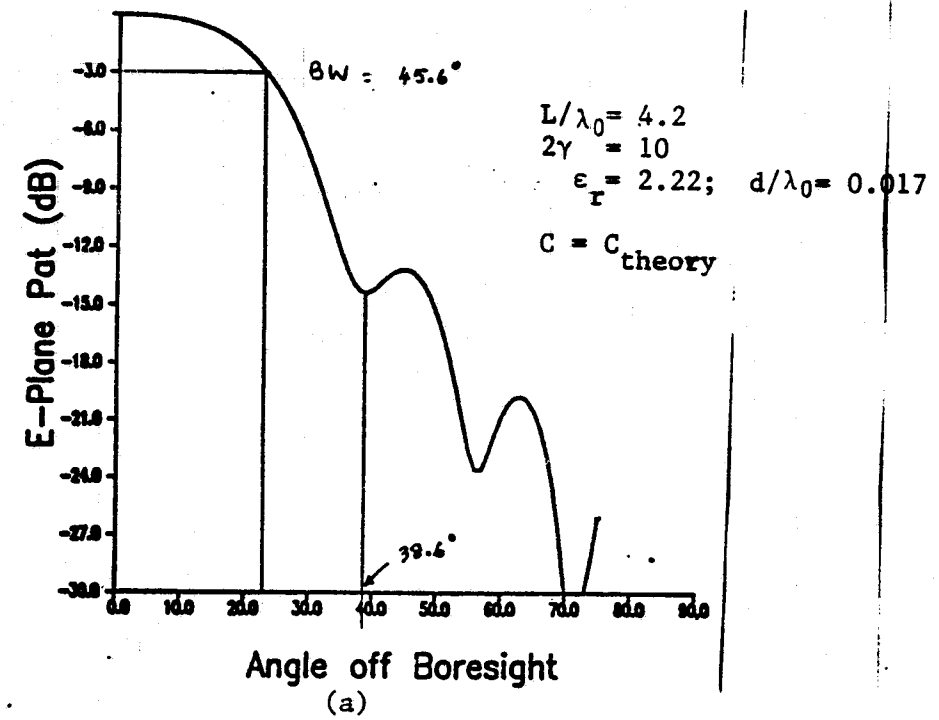

(a)

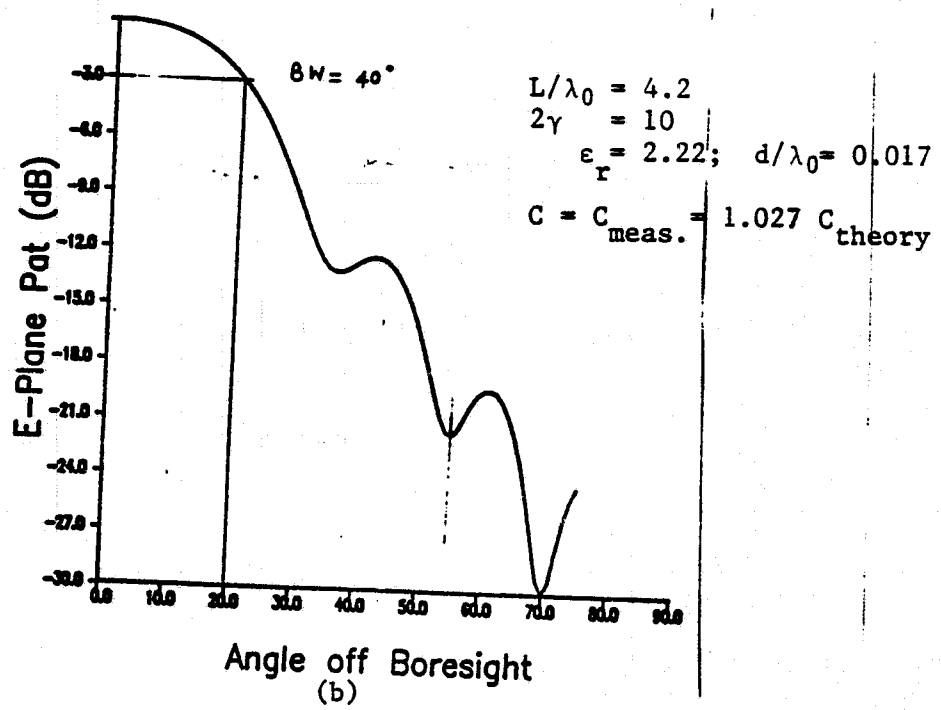

(b)

Fig. 11. Computed E-Plane pattern of LTSA using
a) Computed slot wavelength
b) Measured slot wavelength

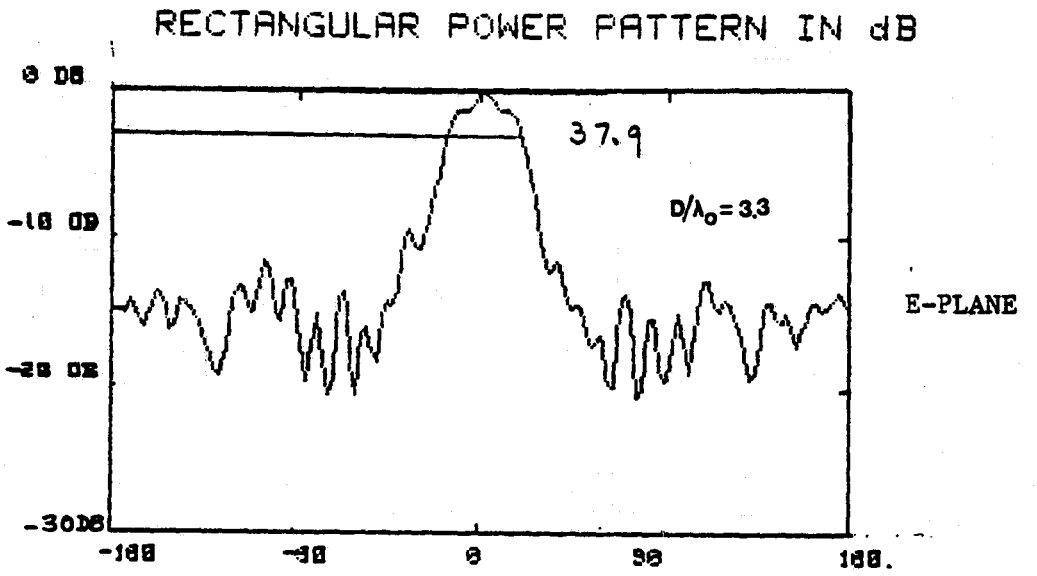

Fig. 11c. Measured E-PLANE pattern of LTSA.
$L/\lambda_0 = 4.2$, $2\gamma = 10$, $\varepsilon_r = 2.22$, $d/\lambda_0 = 0.017$

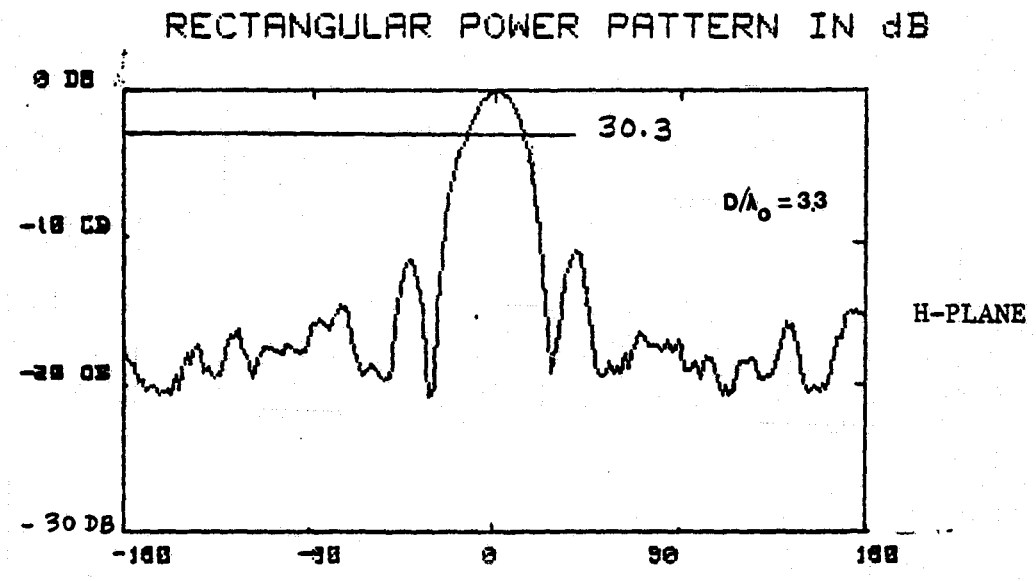

Fig. 11d .Measured H-Plane pattern of LTSA.
$L/\lambda_0 = 4.2$, $2\gamma = 10$, $\varepsilon_r = 2.22$, $d/\lambda_0 = 0.017$

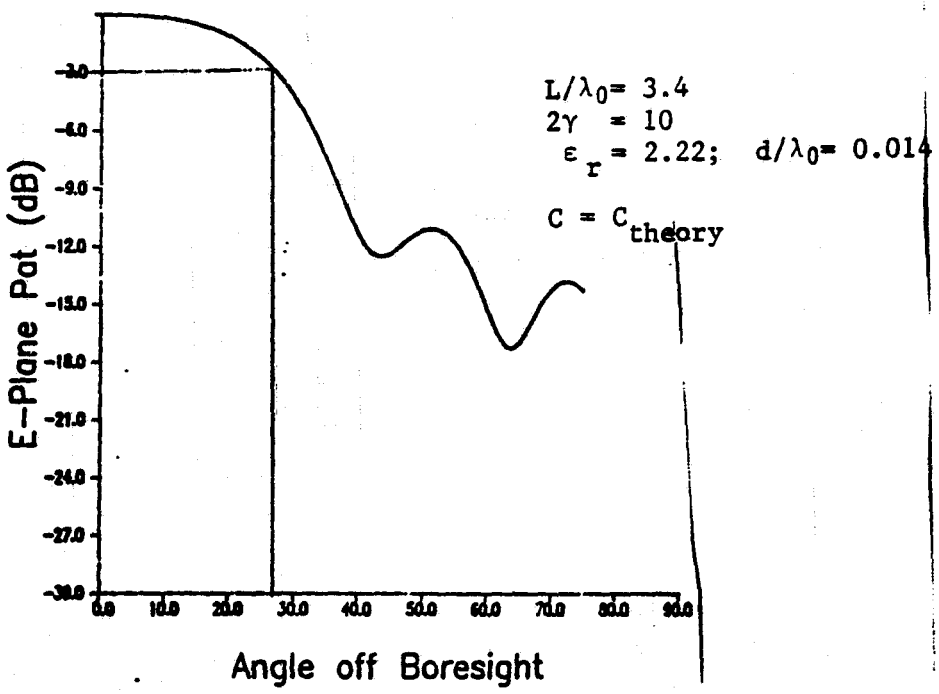

(a)

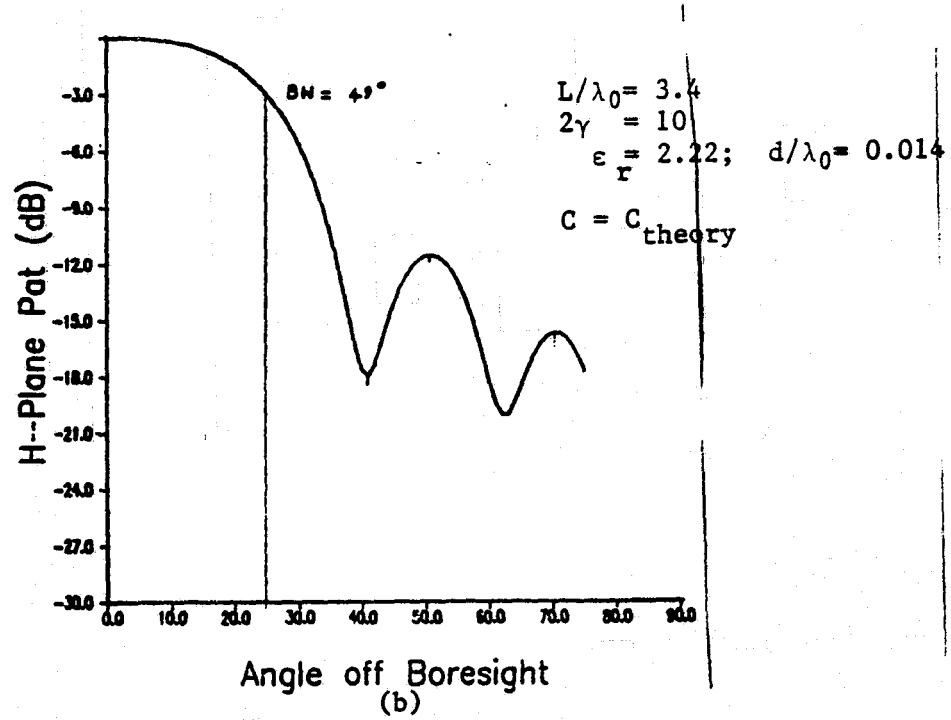

(b)

Fig. 12. Computed radiation pattern of LTSA.
a) E-Plane.
b) H-Plane.

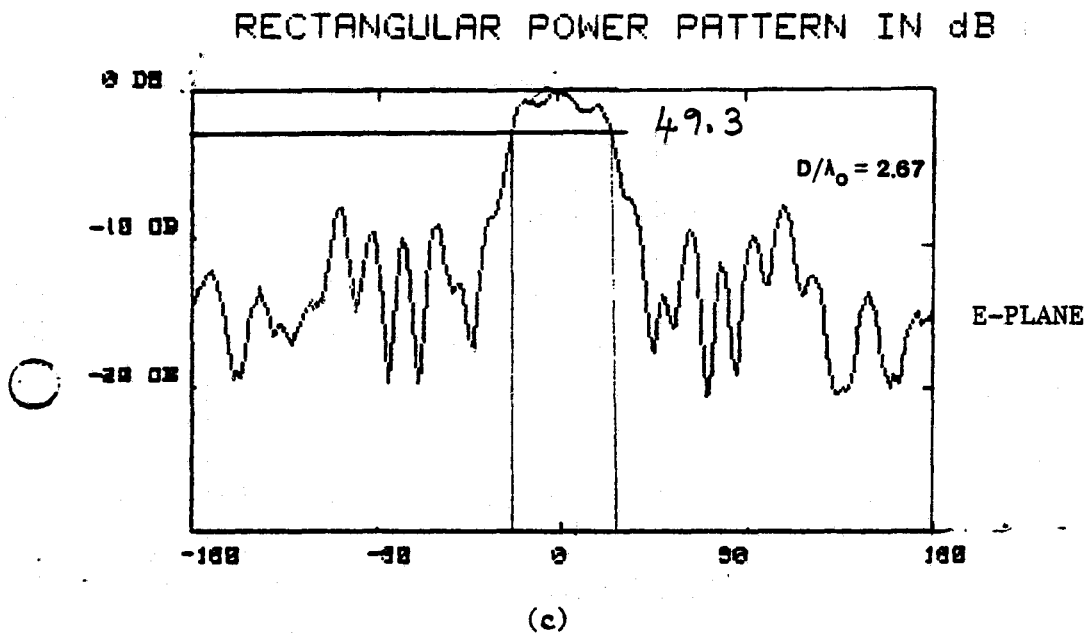

(c)

$L/\lambda_0 = 3.4$, $2\gamma = 10$, $\varepsilon_r = 2.22$; $d/\lambda_0 = 0.014$

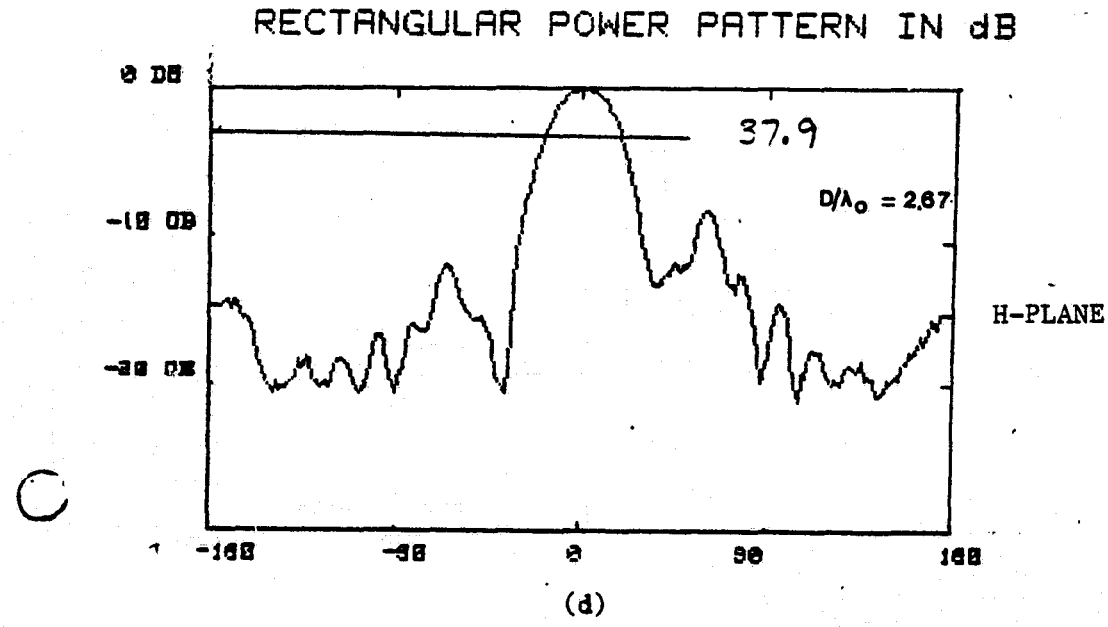

(d)

Fig. 12. Measured radiation pattern of the LTSA.
c) E-PLANE.
d) H-PLANE.

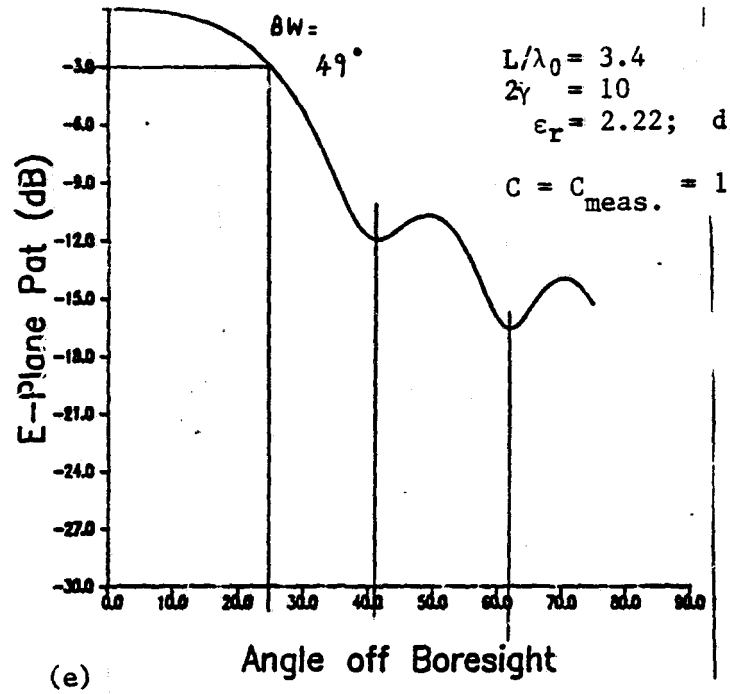

(e)

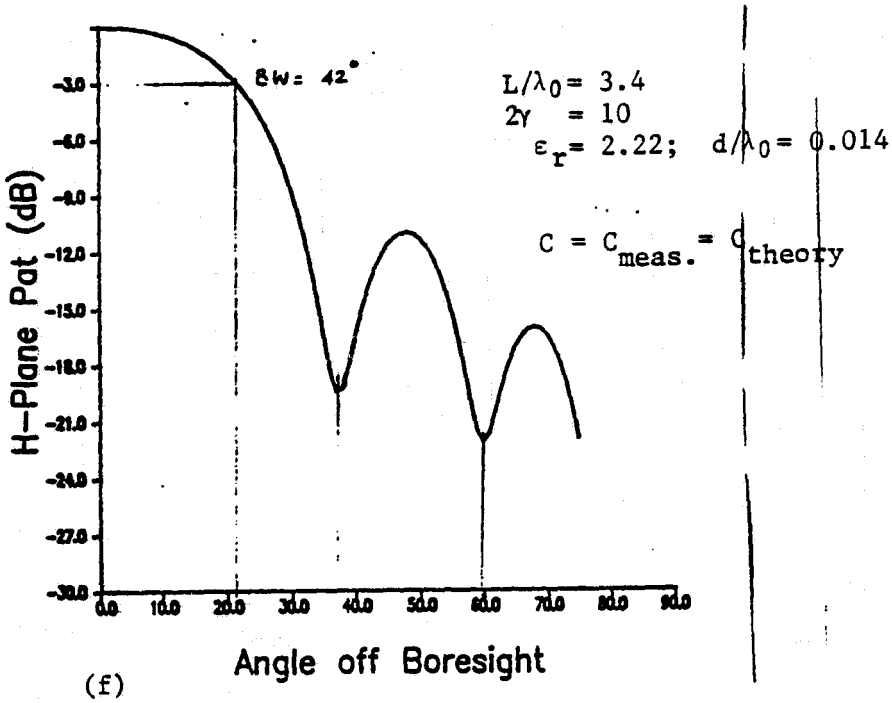

(f)

Fig. 12. Computed radiation pattern of the LTSA using the measured slot wavelength
e) E-PLANE
f) H-PLANE

A P P E N D I X A:

EFFECT OF LATERAL HEIGHT D ON LTSA PATTERNS

FIGURES A1 - A7 : E-PLANE, H-PLANE

$L/\lambda_0 = 7.2$

$2\gamma = 11.9$ Degrees.

E - P L A N E P A T T E R N S

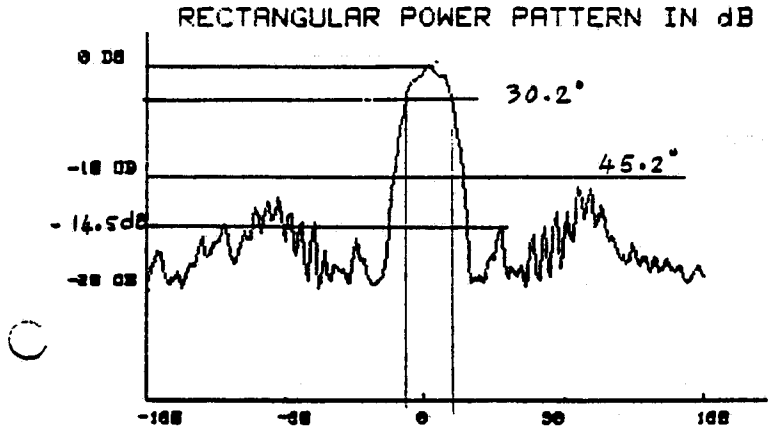

$D/\lambda_0 = 4.5$

$W_0/D = 0.17$

E-PLANE

(A1)

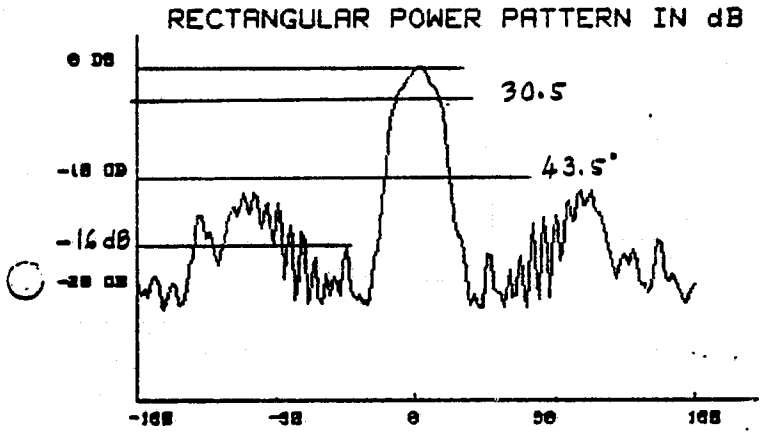

$D/\lambda_0 = 3.75$

$W_0/D = 0.2$

E-PLANE

(A2)

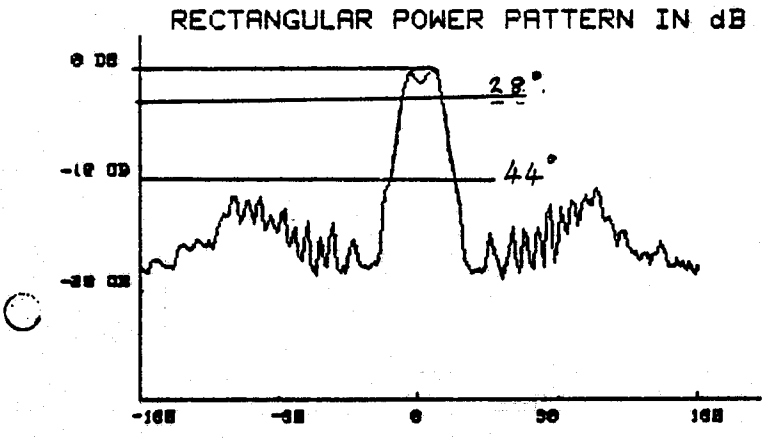

$D/\lambda_0 = 3.0$

$W_0/D = 0.25$

E-PLANE

(A3)

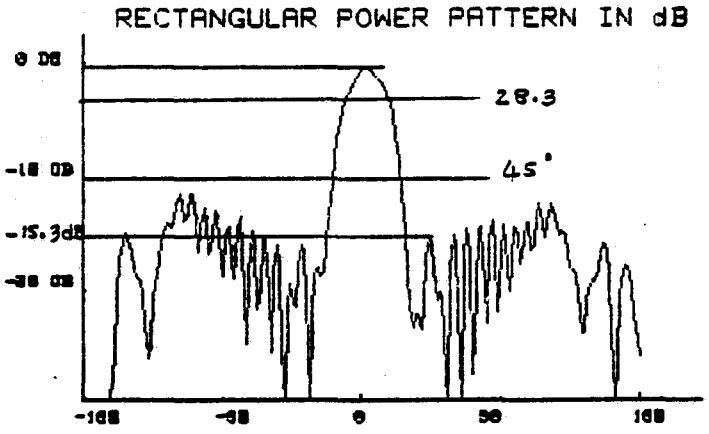

$D/\lambda_0 = 2.25$

$W_0/D = 0.33$

E-PLANE

(A4)

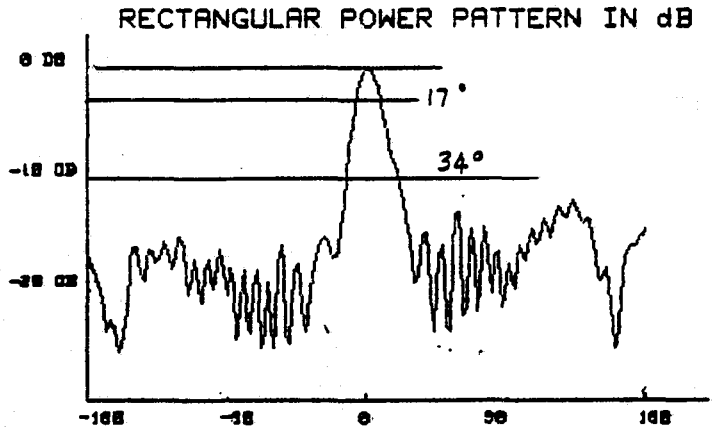

$D/\lambda_0 = 1.5$

$W_0/D = 0.5$

E-PLANE

(A5)

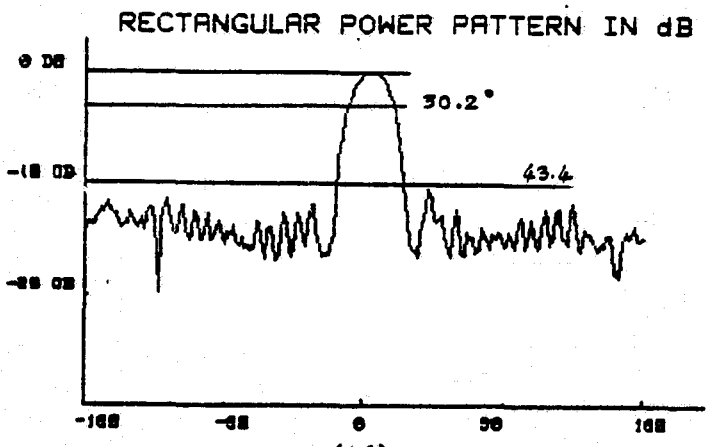

$D/\lambda_0 = 1.125$

$W_0/D = 0.67$

E-PLANE

(A6)

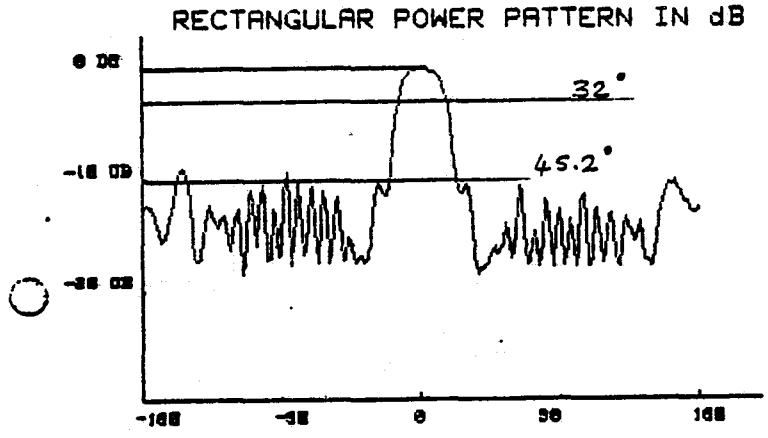

$D/\lambda_0 = 0.75$

$W_0/D = 1.0$

E-PLANE

H - P L A N E P A T T E R N S

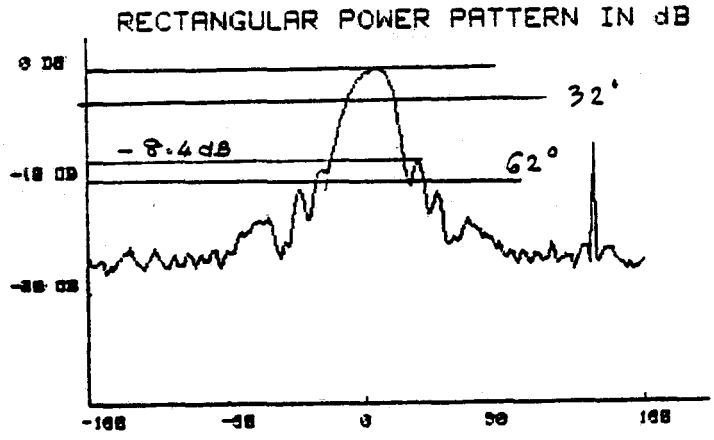

$D/\lambda_0 = 4.5$

$W_0/D = 0.17$

H-PLANE

(A1)

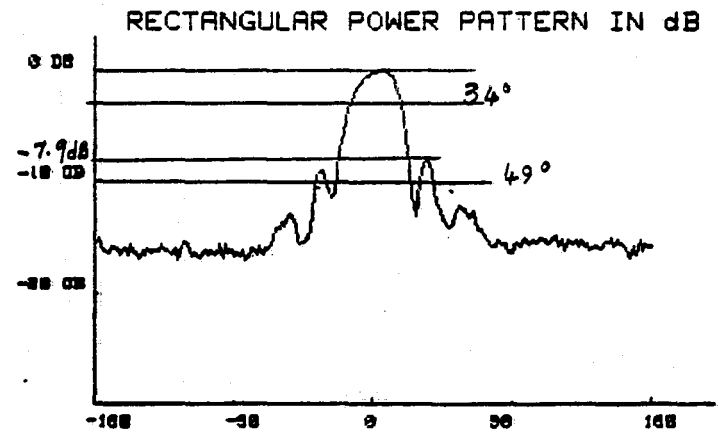

$D/\lambda_0 = 3.75$

$W_0/D = 0.20$

H_PLANE

(A2)

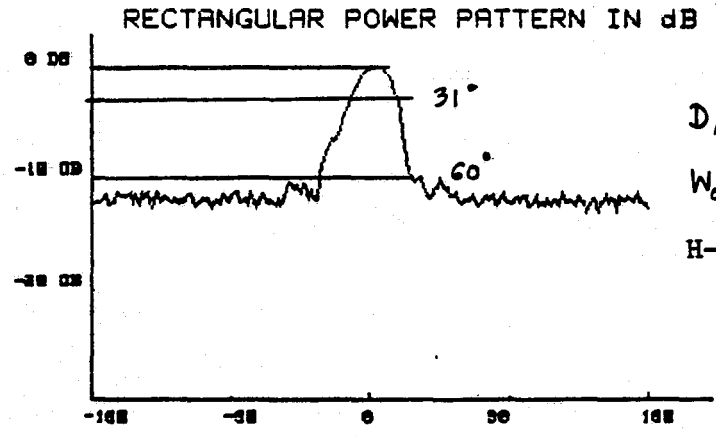

$D/\lambda_0 = 3.0$

$W_0/D = 0.25$

H-PLANE

(A3)

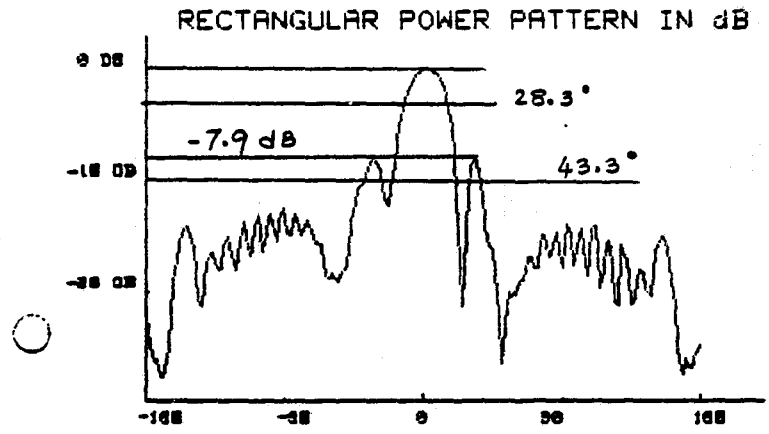

$D/\lambda_0 = 2.25$

$W_0/D = 0.33$

H-PLANE

(A4)

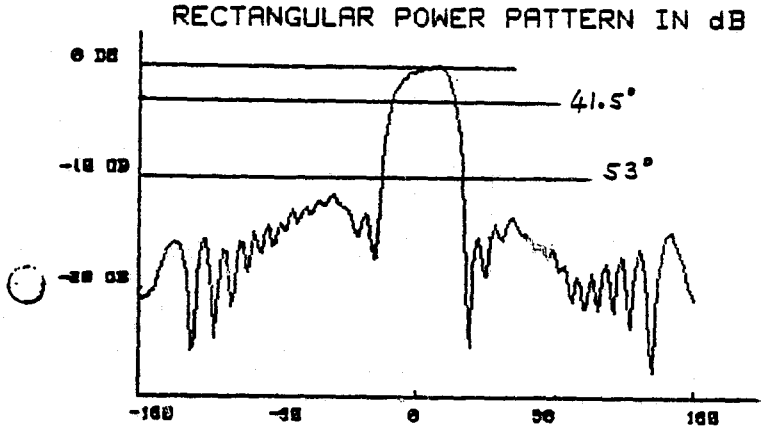

$D/\lambda_0 = 1.5$

$W_0/D = 0.5$

H-PLANE

(A5)

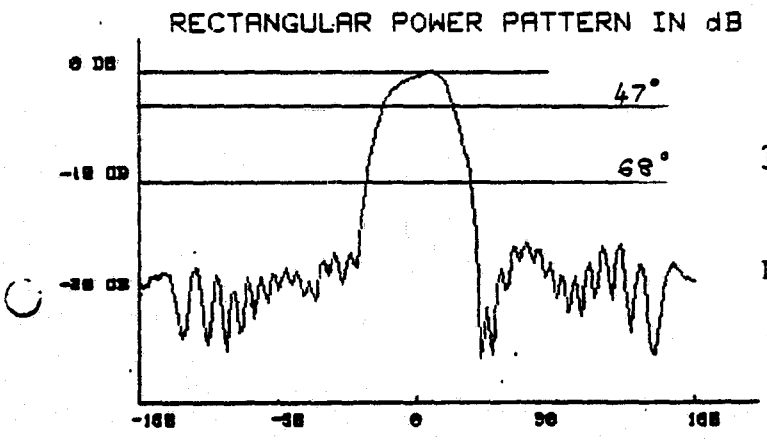

$D/\lambda_0 = 1.125$

$W_0/D = 0.67$

H-PLANE

(A6)

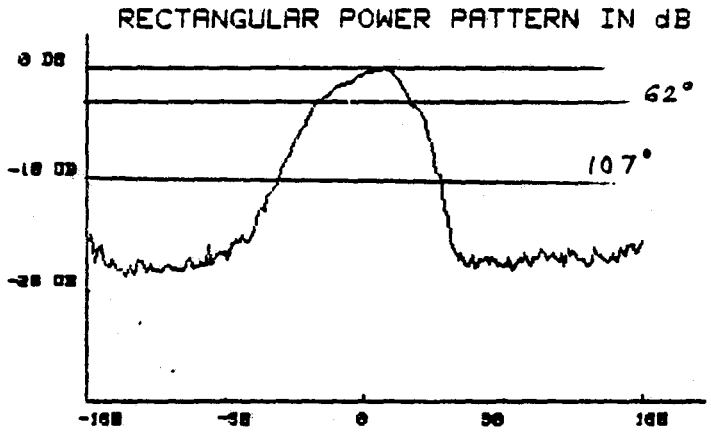

$D/\lambda_0 = 0.75$

$W_0/D = 1.0$

H-PLANE

A P P E N D I X B:

ADDITIONAL RADIATION PATTERNS AND LATERAL TRUNCATION EFFECTS ON LTSA PATTERNS

Figs. B1 - B4 : Comparison of the radiation pattern between the theory and experiment at 8.0 GHz.

B1 - Theory (E-PLANE)
B2 - Theory (H-PLANE)
B3 - Exp. (E-PLANE)
B4 - Exp. (H-PLANE)

(C W S A)

Figs. B5 - B12 : Effect of the lateral height D on the patterns (L T S A) at 8.0 GHz

$L/\lambda_0 = 3.4$, $2\gamma = 10$, $\varepsilon_r = 2.22$, $d/\lambda_0 = 0.014$

Figs. B13 - B19 : Effect of the lateral height D on L T S A patterns at 10.0 GHz.

$L/\lambda_0 = 4.2$, $2\gamma = 10$, $\varepsilon_r = 2.22$, $d/\lambda_0 = 0.017$

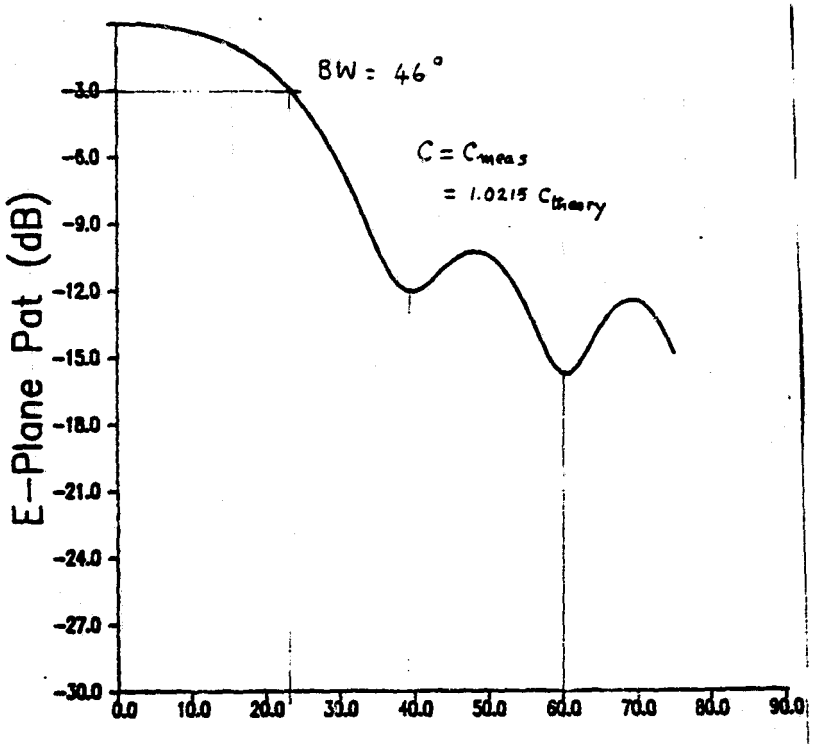

(B1)

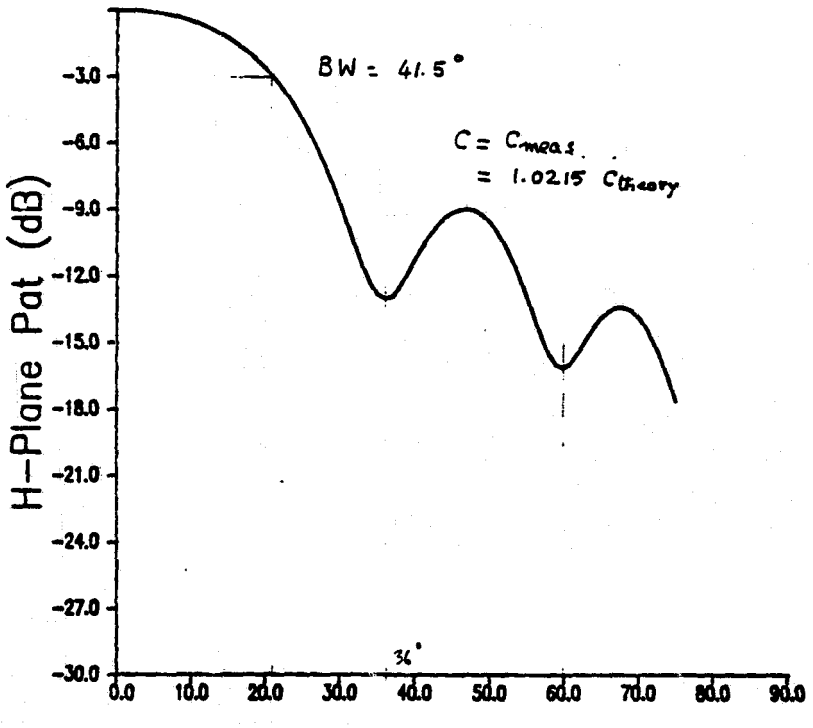

(B2)

Computed patterns of CWSA at 8.0 GHz.
$L/\lambda_0 = 3.4$, $2W/\lambda_0 = 0.54$, $\epsilon_r \hat{=} 2.22$, $d/\lambda_0 = 0.014$

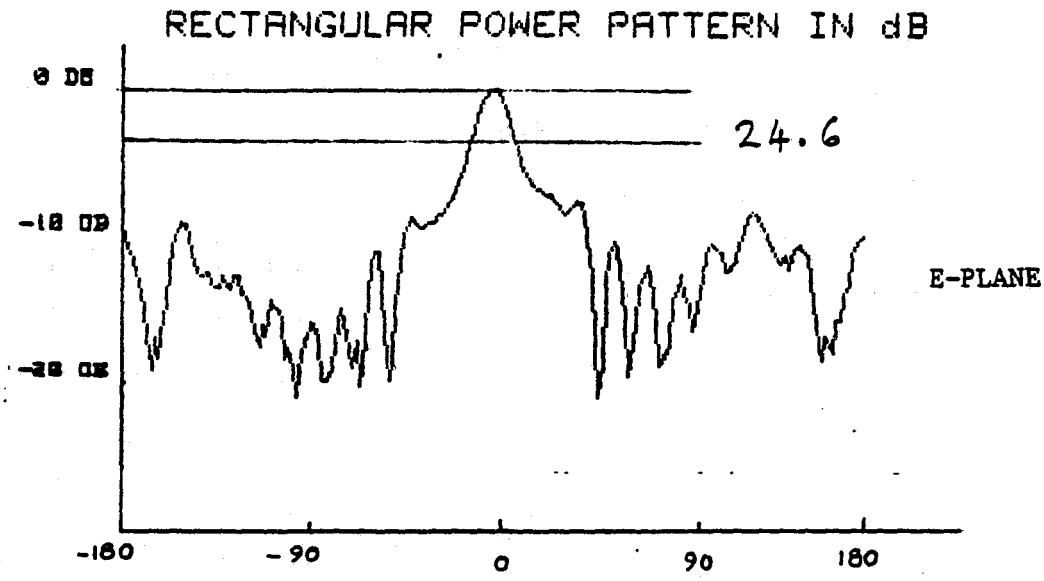

(B3)

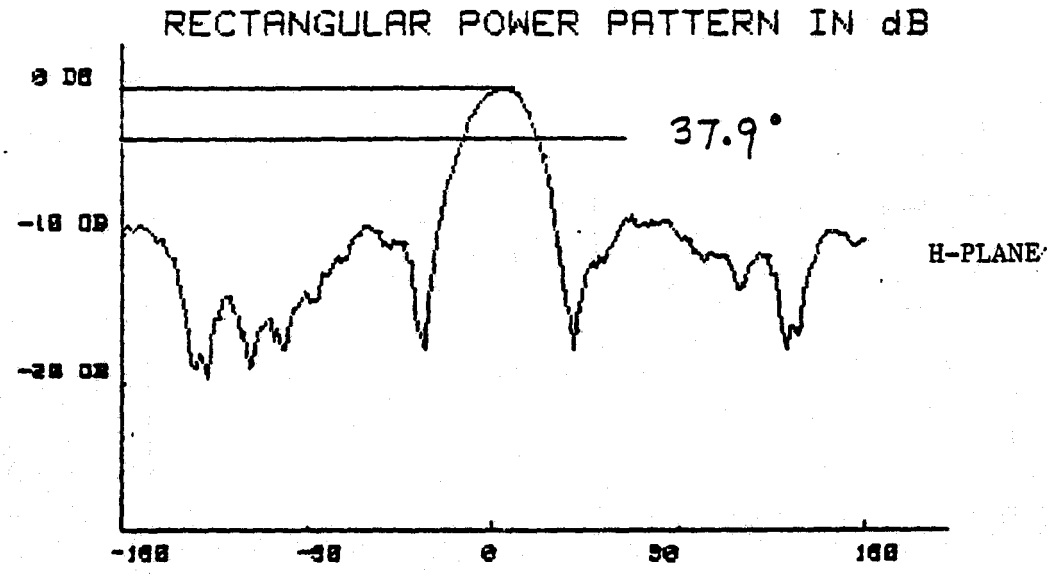

(B4)

Measured radiation patterns of CWSA.

E-PLANE PATTERNS

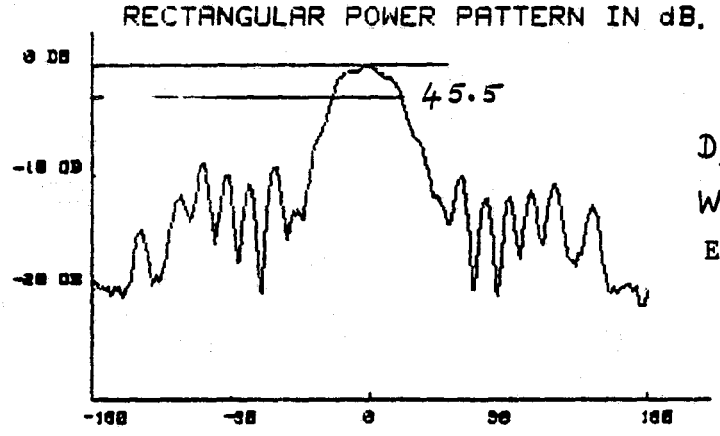

$D/\lambda_0 = 2.4$

$W_0/D = 0.11$

E-PLANE

(B5)

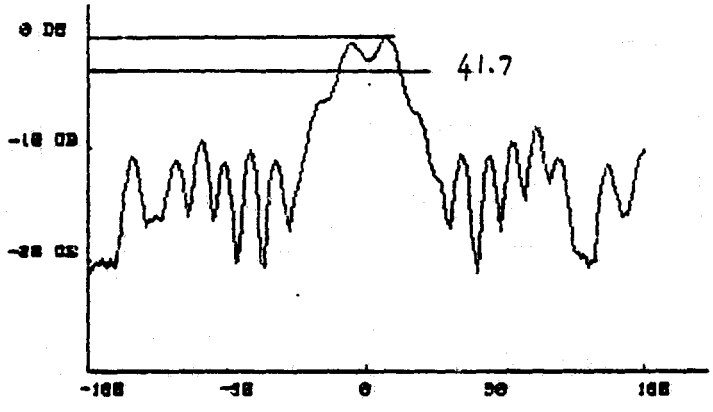

$D/\lambda_0 = 2.13$

$W_0/D = 0.125$

E-PLANE

(B6)

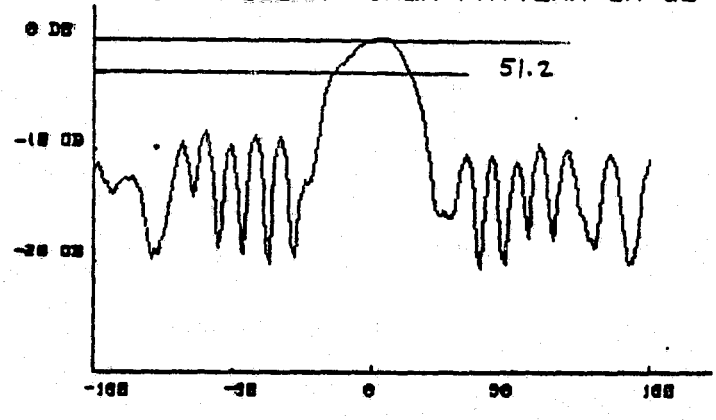

$D/\lambda_0 = 1.87$

$W_0/D = 0.143$

E-PLANE

(B7)

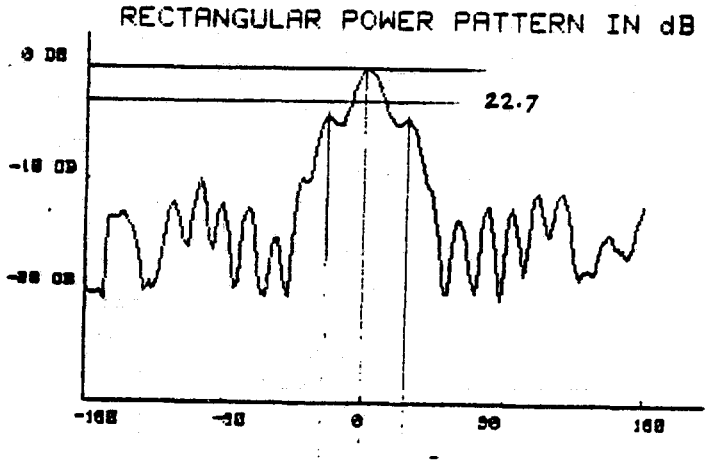

$D / \lambda_0 = 1.6$

$W_0/D = 0.17$

E-PLANE

(B8)

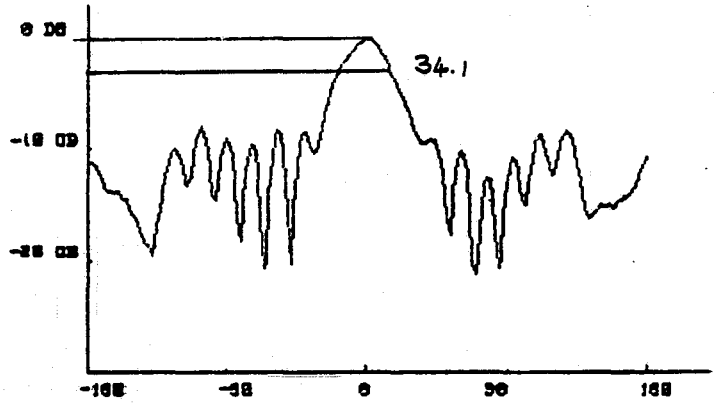

$D/\lambda_0 = 1.33$

$W_0/D = 0.2$

E-PLANE

(B9)

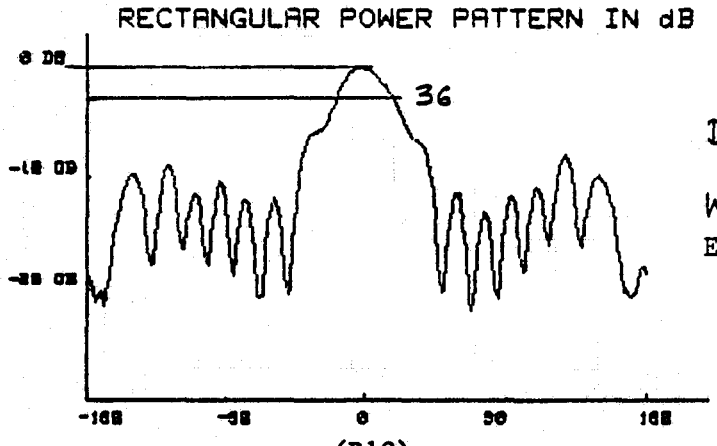

$D/\lambda_0 = 0.8$

$W_0/D = 0.33$

E-PLANE

(B10)

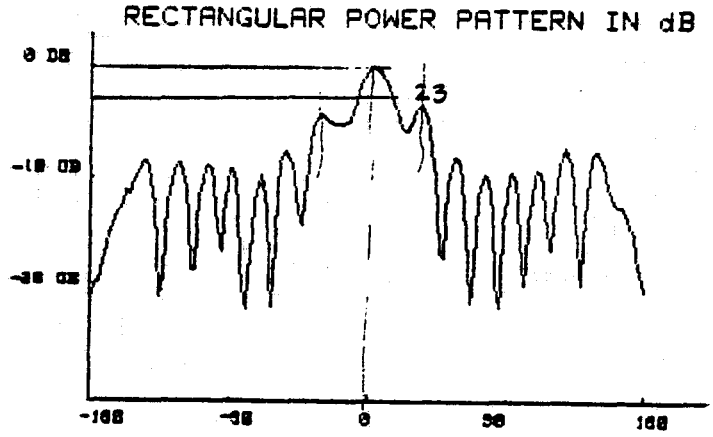

$D/\lambda_o = 0.53$

$W_o/D = 0.5$

E-PLANE

(B11)

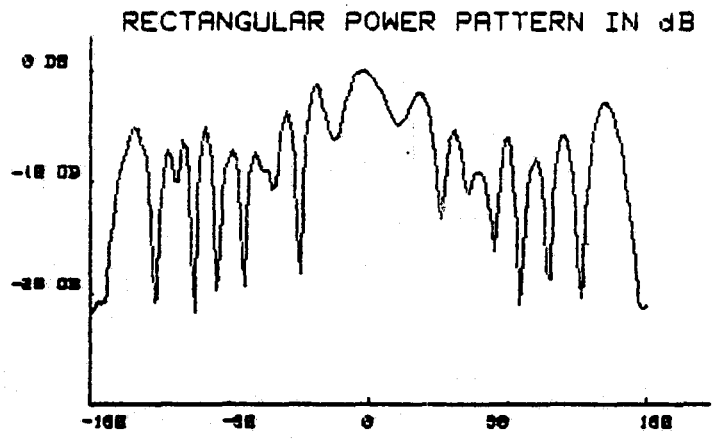

$D/\lambda_o = 0.4$

$W_o/D = 0.67$

E-PLANE

(B12)

H - P L A N E P A T T E R N S

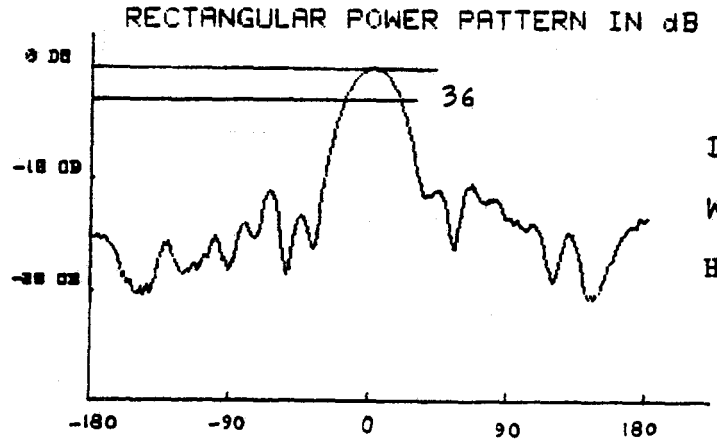

$D/\lambda_0 = 2.4$

$W_0/D = 0.11$

H-PLANE

(B5)

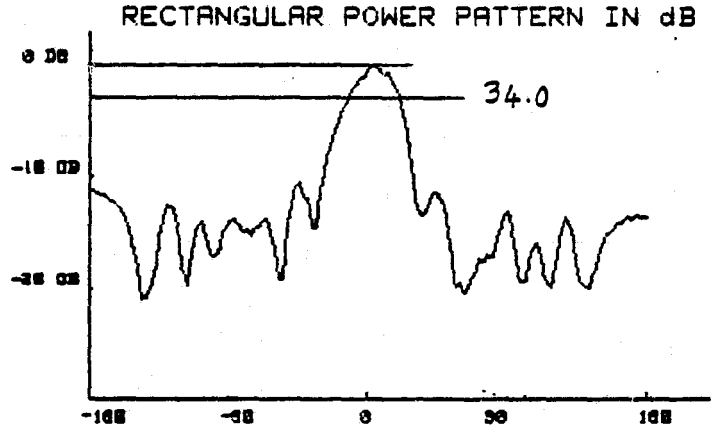

$D/\lambda_0 = 2.13$

$W_0/D = 0.125$

H-PLANE

(B6)

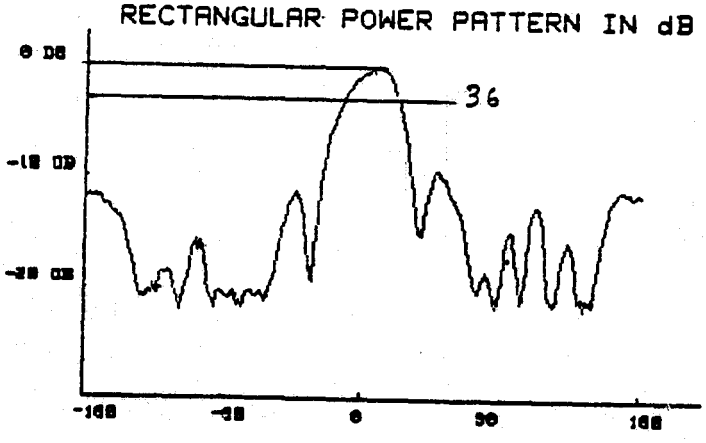

$D/\lambda_0 = 1.87$

$W_0/D = 0.143$

H-PLANE

(B7)

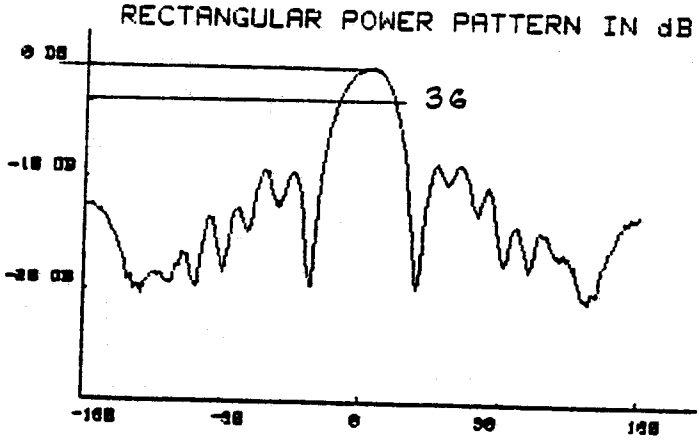

$D/\lambda_o = 1.6$

$W_o/D = 0.17$

H-PLANE

(B8)

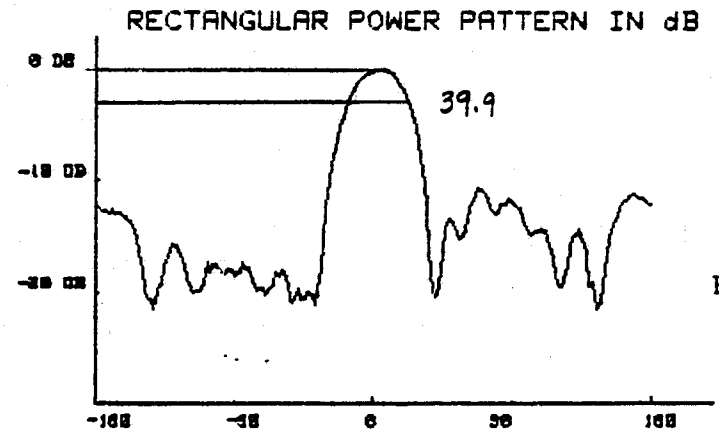

$D/\lambda_o = 1.33$

$W_o/D = 0.2$

H-PLANE

(B9)

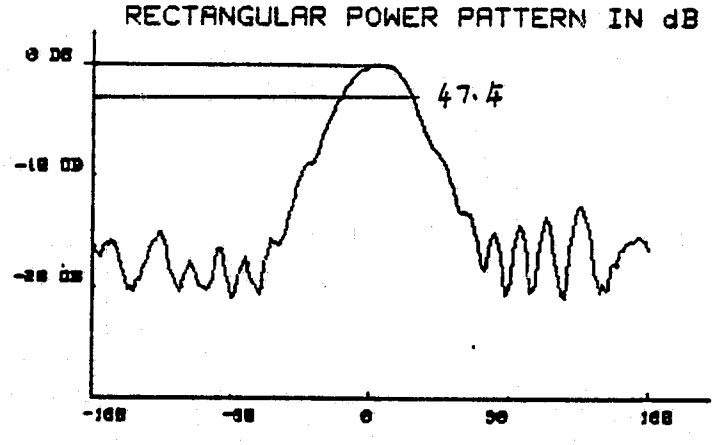

$D/\lambda_o = 0.8$

$W_o/D = 0.33$

H-PLANE

(B10)

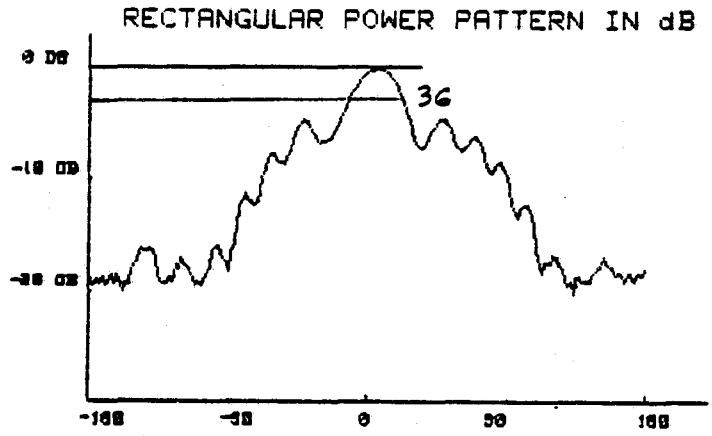

$D/\lambda_0 = 0.53$

$W_0/D = 0.5$

H-PLANE

(B11)

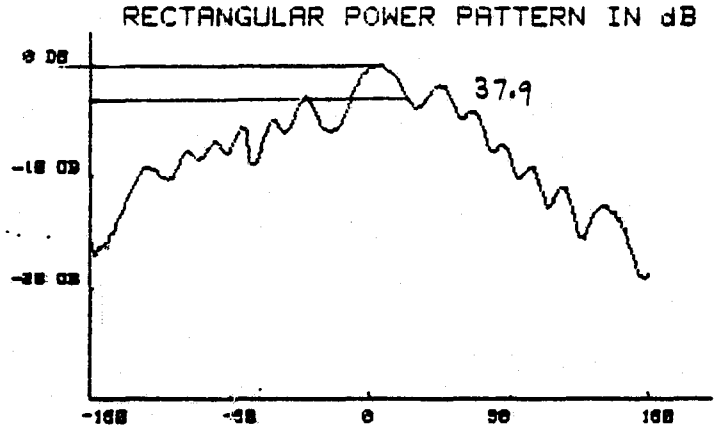

$D/\lambda_0 = 0.4$

$W_0/D = 0.67$

H-PLANE

(B12)

ORIGINAL PAGE IS
OF POOR QUALITY

E - P L A N E P A T T E R N S

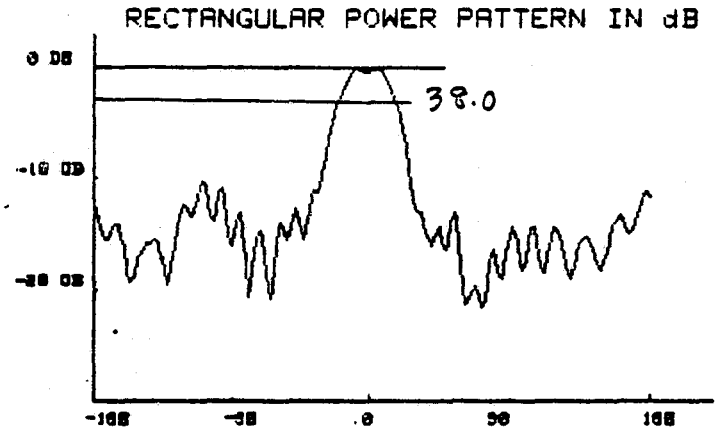

$D/\lambda_0 = 3.33$

$W_0/D = 0.11$

E-PLANE

(B13)

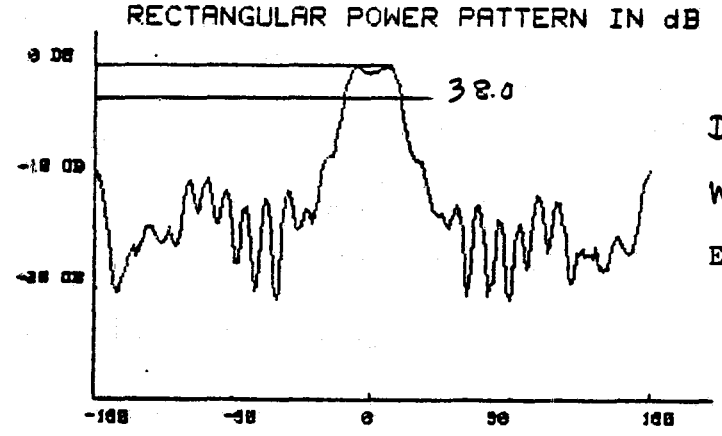

$D/\lambda_0 = 2.33$

$W_0/D = 0.143$

E-PLANE

(B14)

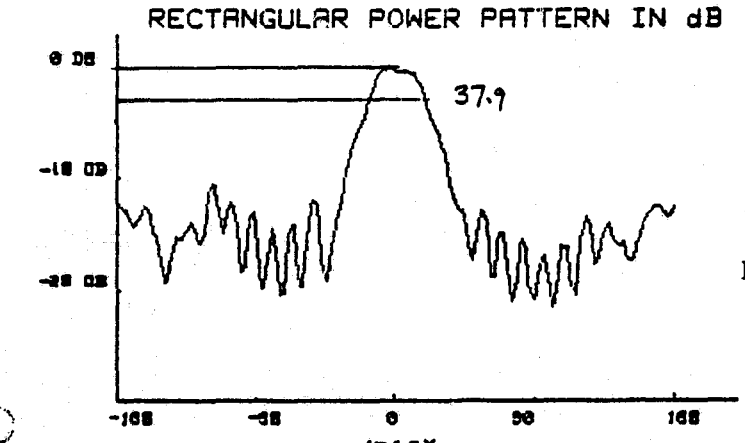

$D/\lambda_0 = 2.0$

$W_0/D = 0.17$

E-PLANE

(B15)

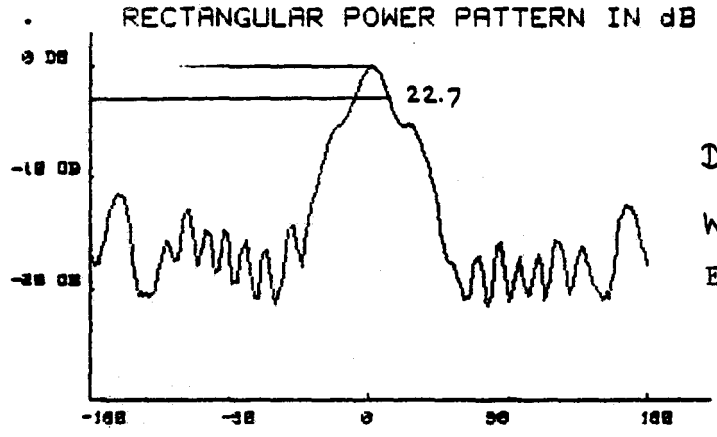

$D/\lambda_o = 1.67$

$W_o/D = 0.2$

E-PLANE

(B16)

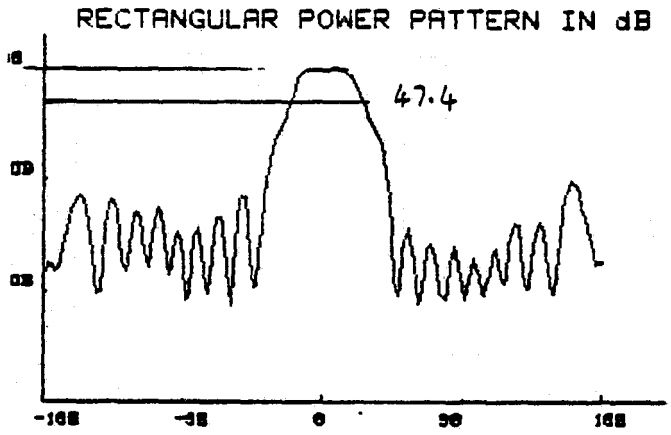

$D/\lambda_o = 1.0$

$W_o/D = 0.33$

E-PLANE

(B17)

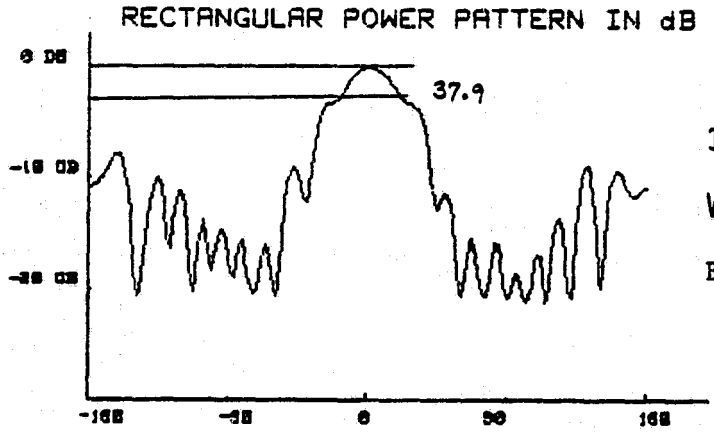

$D/\lambda_o = 0.67$

$W_o/D = 0.50$

E-PLANE

(B18)

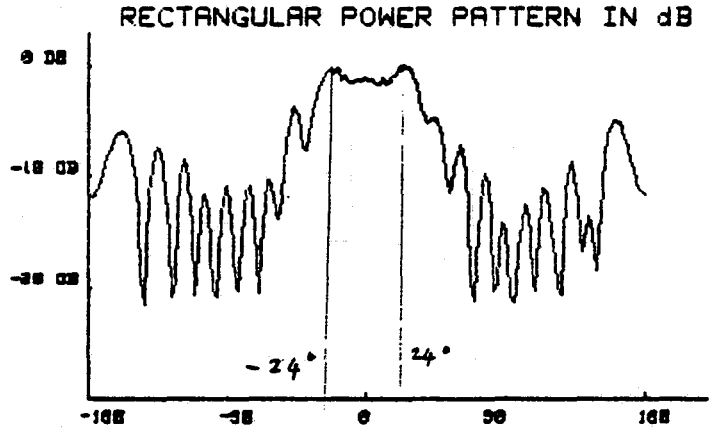

$D/\lambda_o = 0.5$

$W_o/D = 0.67$

E-PLANE

RECTANGULAR POWER PATTERN IN dB

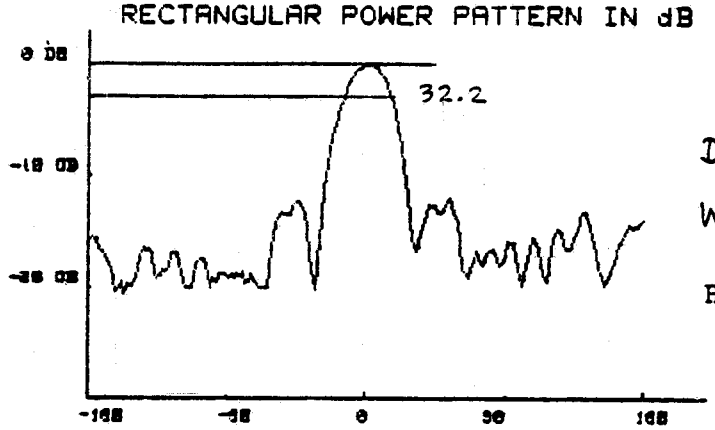

$D/\lambda_0 = 3.33$

$W_0/D = 0.11$

H-PLANE

(B13)

RECTANGULAR POWER PATTERN IN dB

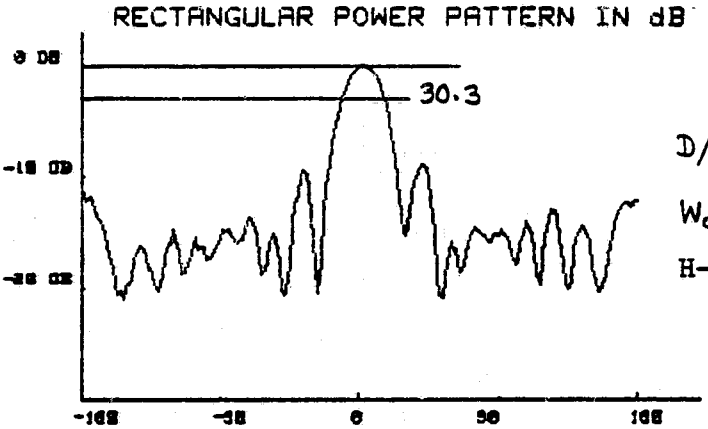

$D/\lambda_0 = 2.33$

$W_0/D = 0.143$

H-PLANE

(B14)

RECTANGULAR POWER PATTERN IN dB

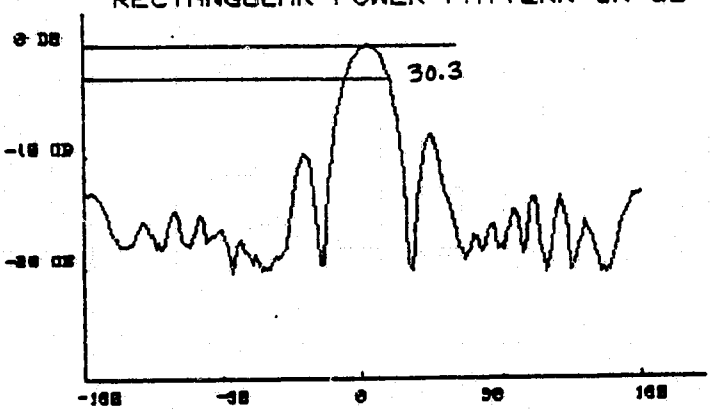

$D/\lambda_0 = 2.0$

$W_0/D = 0.17$

H-PLANE

(B15)

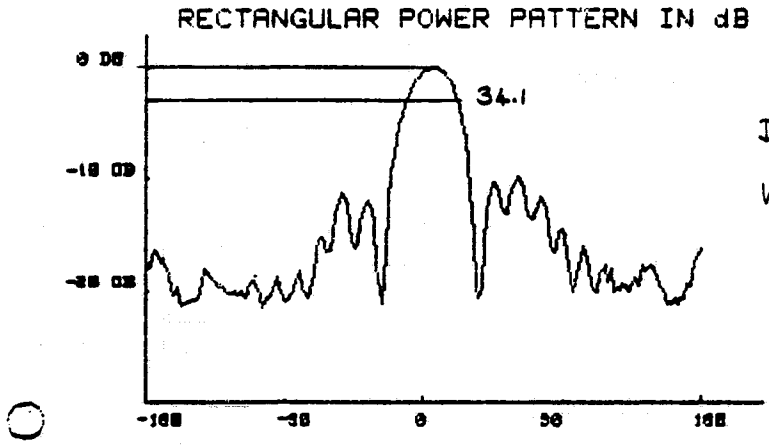

$D/\lambda_o = 1.67$

$W_o/D = 0.2$

H-PLANE

(B16)

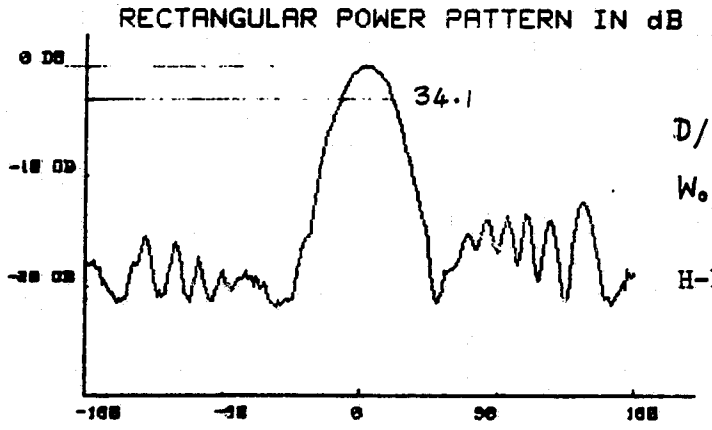

$D/\lambda_o = 1.0$

$W_o/D = 0.33$

H-PLANE

(B17)

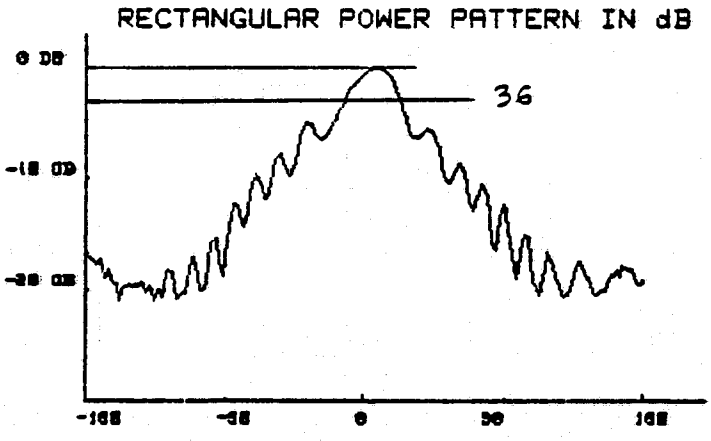

$D/\lambda_o = 0.67$

$W_o/D = 0.50$

H-PLANE

(B18)

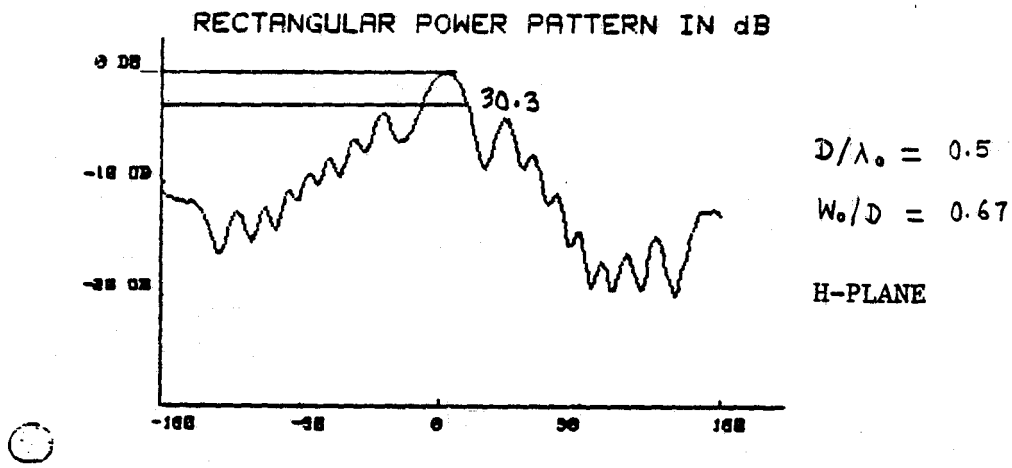
RECTANGULAR POWER PATTERN IN dB
0 DB
-10 DB
-20 DB
30.3
-180
-90
0
90
180
D/λ₀ = 0.5
W₀/D = 0.67
H-PLANE

D2

N86-12480

Characteristic Impedance of a Wide Slot Line on Low Permittivity Substrates*

R. Janaswamy
D.H. Schaubert

Department of Electrical and Computer Engineering
University of Massachusetts
Amherst, MA 01003

July 1985

* This work was supported by NASA Langley Research Center under grant number NAG-1-279

Abstract: Computed results on the characteristic impedance of wide slots etched on an electrically thin substrate of low dielectric constant ε_r are presented. These results combined with those in [1] provide design data for these slotlines. Results are given for ε_r = 2.22, 3.0, 3.8 and 9.8. Comparison is shown for the characteristic impedance between the present calculations and those available in the literature for high-ε_r substrates.

I. Introduction

Impedance properties of a slot line shown in Fig. 1 have been thoroughly treated in the literature by a number of authors [2,3]. All the previous work has been confined to slots on high-ε_r substrates ($\varepsilon_r \geq 9.6$), which are typically used for circuit applications. No data have been reported for slots on low-ε_r substrates, where slot lines have interesting applications as antennas [4-6]. Knowledge of the characteristic impedance of slot lines on these low-ε_r substrates is highly desirable in designing a proper feed and accompanying circuits for these antennas.

In this paper, computed data are presented for the characteristic impedance Z_o for slots on low-ε_r substrates. The problem is formulated in the spectral domain and the eigenvalue equation for the eigen-pair (λ', e^s), where λ' is the slot wavelength and e^s the slot field, is solved by using the spectral Galerkin's method [7]. The slot characteristic impedance Z_o is calculated from the slot field in the spectral domain.

II. Formulation of the Problem and Numerical Results

The characteristic impedance Z_o of the slot line shown in Fig. 1 is defined as [2]

$$Z_o = \frac{|V_o|^2}{P_f} \tag{1}$$

where V_o is the voltage across the slot in the plane of the slot and is given in terms of the transverse electric field component E_x as

$$V_o = \int_{-W/2}^{W/2} E_x dx = \tilde{E}_x(\alpha)\Big|_{\alpha=0} = \tilde{E}_x(0) \tag{2}$$

"~" denotes quantities Fourier transformed with respect to the x-axis and α is the transform variable. P_f is the real part of the complex power flow (actually real in this case for a propagating mode) along the slot and is given by

$$\begin{aligned} P_f &= \int_x \int_{y \text{ plane}} (E_x H_y^* - E_y H_x^*)\, dxdy \\ &= \frac{1}{2\pi} \int_\alpha \int_{y \text{ plane}} (\tilde{E}_x \tilde{H}_y^* - \tilde{E}_y \tilde{H}_x^*)\, d\alpha dy \end{aligned} \tag{3}$$

where E_x, E_y, H_x, H_y are fields tangential to the z=constant plane. The second equality in (3) follows from Parseval's theorem.

The fields $\tilde{E}$ and $\tilde{H}$ in the spectral domain pertaining to the air and dielectric region of the slot line can be related to the aperture field (i.e., field in the slot), which is modeled by the method of moments. As was done in [1], the field in the slot region is expanded as

$$E_x^s = \sum_{n=0}^{M_x} a_n e_n^x \quad ; \quad e_n^x = \left(\frac{2}{\pi W}\right) \frac{T_{2n}\left(\frac{2x}{W}\right)}{\sqrt{1-\left(\frac{2x}{W}\right)^2}} \quad ; n = 0,1,\ldots \tag{4}$$

$$E_z^s = \sum_{m=1}^{M_z} b_m e_m^z \quad ; \quad e_m^z = \left(\frac{2}{\pi W} n\, U_{2m-1}\left(\frac{2x}{W}\right) \sqrt{1-\left(\frac{2x}{W}\right)^2}\right) \quad ; m = 1,2,\ldots \tag{5}$$

where T_n and U_n are Tchebycheff polynomials of the I and II kind respectively.

The Fourier transforms of the above basis functions can be found readily in closed form as [8]

$$\tilde{e}_n^x = (-1)^n J_{2n}\left(\frac{\alpha W}{2}\right) \quad , \quad n = 0,1,\ldots \tag{6}$$

$$\tilde{e}_m^z = j(-1)^m 2m \frac{J_{2m}\left(\frac{\alpha W}{2}\right)}{\left(\frac{\alpha W}{2}\right)} \quad , \quad m = 1,2,\ldots \tag{7}$$

The integration with respect to y in (3) can be done in closed form, however, the integration on the α variable must be done numerically. The slot wavelength λ' is stationary with respect to the slot field and it was found that λ' converges with only one basis function for the longitudinal field as reported in [1]. However, more than one basis function for E_z^s is needed for the convergence of characteristic impedance Z_o for a wide slot. The maximum number of basis functions needed for E_x^s and E_z^s during the computation of Z_o was 5 and 3, respectively, when the slot width approached one free space wavelength λ_o.

Computer programs were developed to compute λ' and Z_o for a specified ε_r, λ_o and d. As a check of these programs, Table 1 shows a comparison for Z_o between these computations and those in [3]. Characteristic impedances for slot lines have been computed for $\varepsilon_r = 2.22$, 3.0, 3.8 and 9.8 and for widths varying over $0.05 \leq W/\lambda_o \leq 1.0$. Computed values of Z_o vs. W/λ_o with d/λ_o as a parameter are plotted in Figure 2.

III. Conclusion

A spectral domain Galerkin method is used to compute the characteristic impedance of wide slot lines on low ε_r substrates. The data presented here supplement data already available on high ε_r substrates.

References

[1] R. Janaswamy and D.H. Schaubert, "Dispersion Characteristics for Wide Slot Lines on Low Permittivity Substrates," to appear in IEEE Trans. Microwave Theory and Tech., Vol. MTT-33, No. 8, pp. 723-726, August 1985.

[2] J.B. Knorr and K. Kuchler, "Analysis of Coupled Slots and Coplanar Strips on Dielectric Substrate," IEEE Trans. Microwave Theory and Tech., Vol. MTT-23, No. 7, pp. 541-548, July 1975.

[3] E.A. Mariani et al., "Slotline Characteristics," IEEE Trans. Microwave Theory and Tech., Vol. MTT-17, No. 12, pp. 1091-1096, December 1969.

[4] E.L. Kollberg et al., "New Results on Tapered Slot Endfire Antennas on Dielectric Substrate," presented at the 8th IEEE International Conference on Infrared and Millimeter Waves, Miami, December 1983.

[5] S.N Prasad and S. Mahapatra, "A New MIC Slot Line Aerial," IEEE Trans. Antennas and Propagat., Vol. AP-31, No. 3, pp. 525-527, May 1983.

[6] J.F. Johansson, "Investigation of Some Slotline Antennas," Ph.D. Dissertation, Chalmers University, Gothenberg, Sweden, 1983.

[7] T. Itoh and R. Mittra, "Dispersion Characteristics of Slot Lines," Electron Lett., Vol. 7, pp. 364-365, July 1971.

[8] A. Erdelyi et al., Tables of Integral Transforms, Vol. 2, McGraw Hill Book Co., New York, 1954.

Figures

Figure 1. Geometry of slot line.

Figure 2. Characteristic impedance of slot line as a function of normalized slot width. a) $\varepsilon_r = 2.22$ b) $\varepsilon_r = 3.0$ c) $\varepsilon_r = 3.8$ d) $\varepsilon_r = 9.8$.

Table 1. Comparison of calculated characteristic impedance Z_o.

Table 1

Comparison of calculated slot characteristic impedance Z_o.

ε_r	d/λ_o	W/d	$Z_o(\Omega)$	Present
			From curves in [3]	
9.6	0.06	1.0	140	141.87
11.0	0.04	1.5	160	159.8153
13.0	0.03	0.4	80	81.6118
16.0	0.025	2.0	150	151.0611
20.0	0.03	1.0	100	101.405

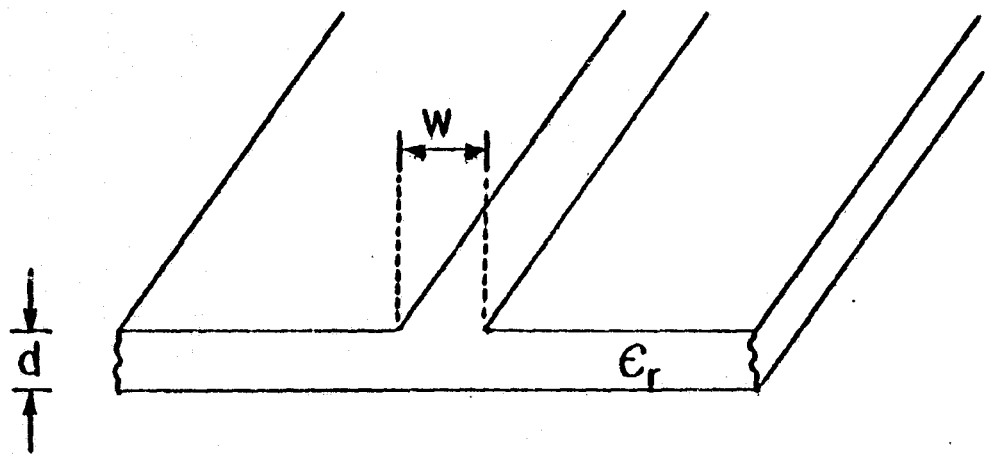

Fig. 1

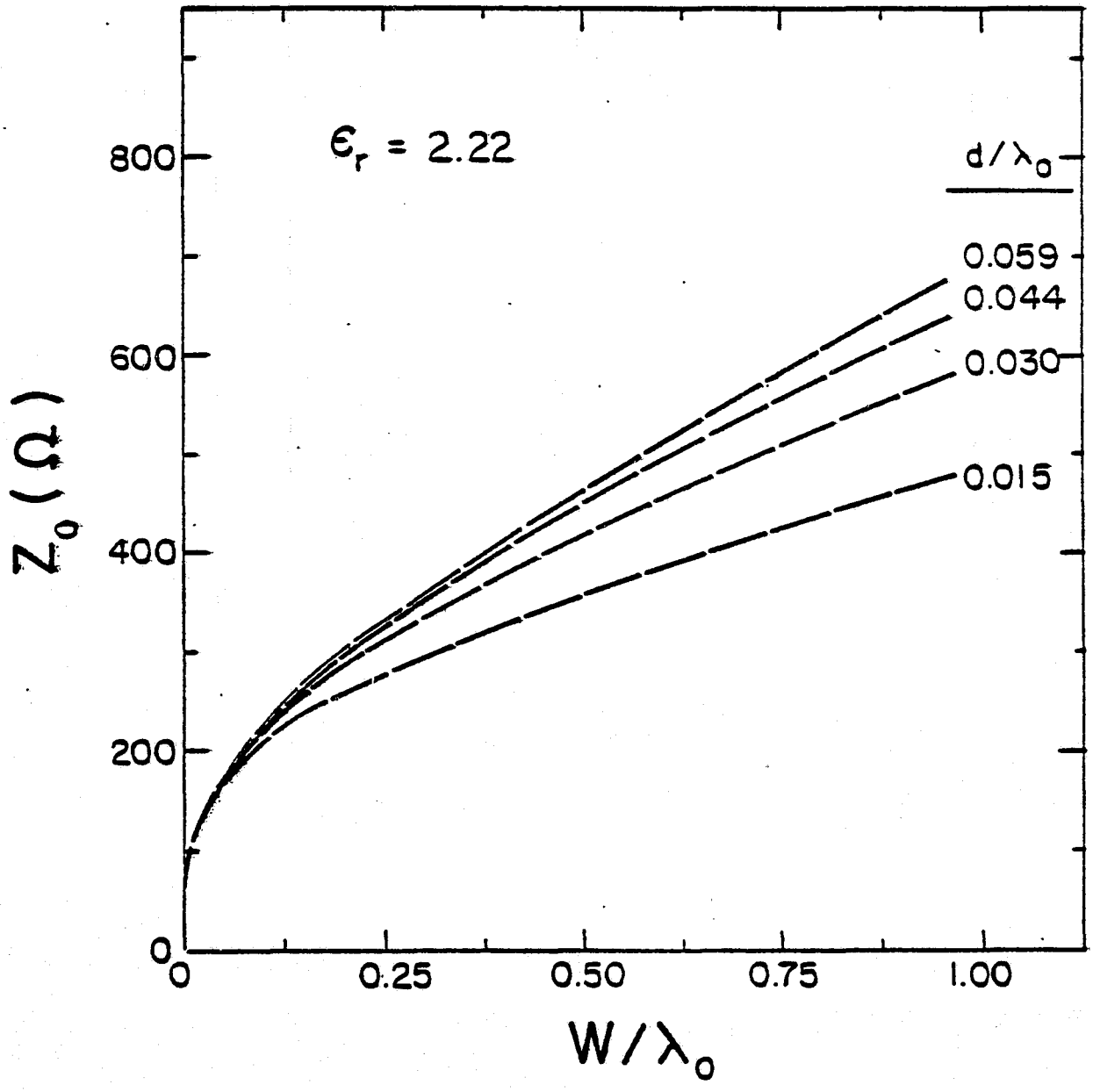
$\epsilon_r = 2.22$
d/λ_0
0.059
0.044
0.030
0.015
800
600
400
200
0
0
0.25
0.50
0.75
1.00
$Z_0\ (\Omega)$
W/λ_0

Fig. 2a

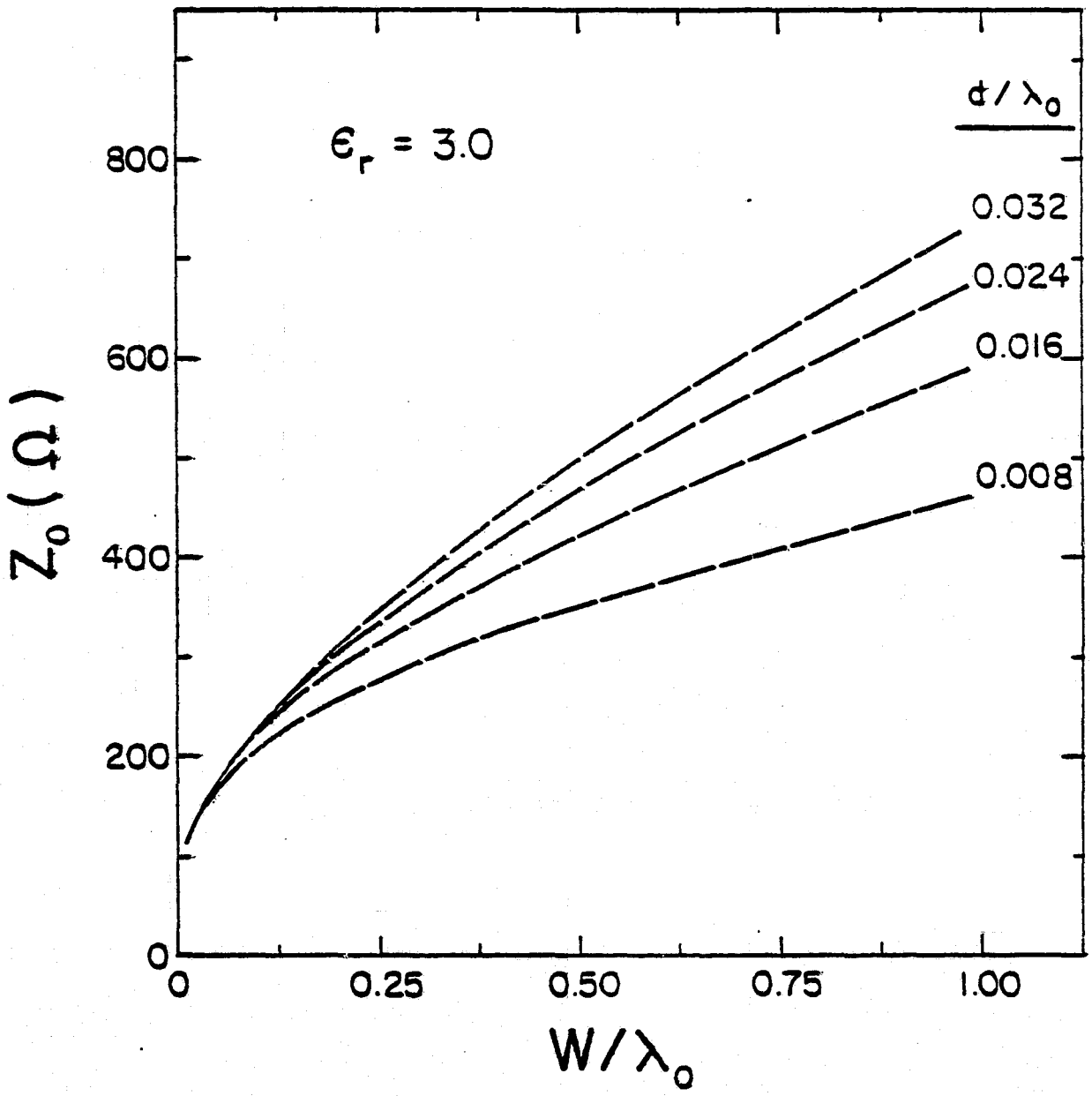
$\epsilon_r = 3.0$
d/λ_0
0.032
0.024
0.016
0.008
800
600
400
200
0
$Z_0(\Omega)$
0
0.25
0.50
0.75
1.00
W/λ_0

Fig. 2b

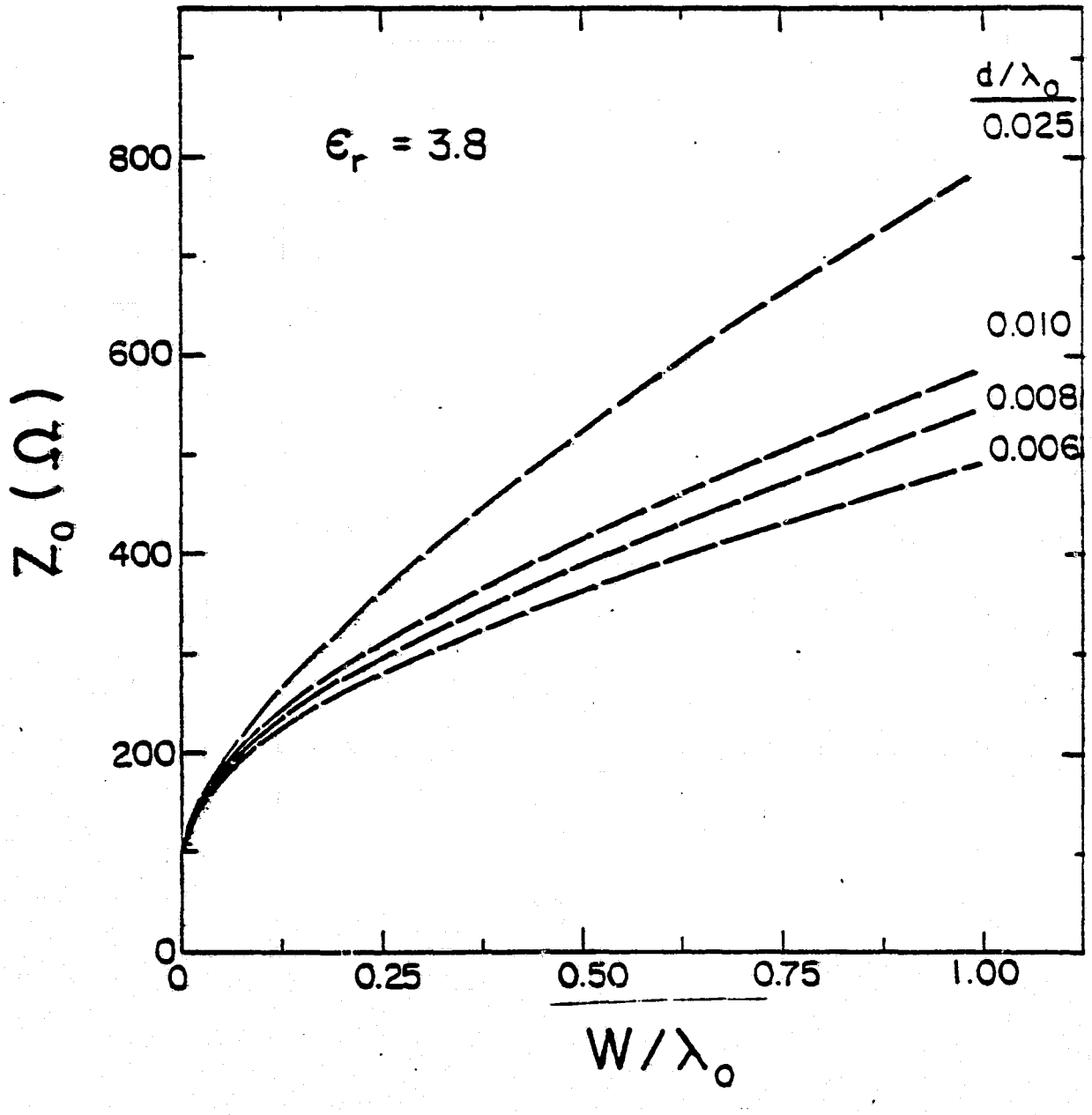
$\epsilon_r = 3.8$
d/λ_0
0.025
0.010
0.008
0.006
800
600
400
200
0
Z_0 (Ω)
0
0.25
0.50
0.75
1.00
W/λ_0

Fig. 2c

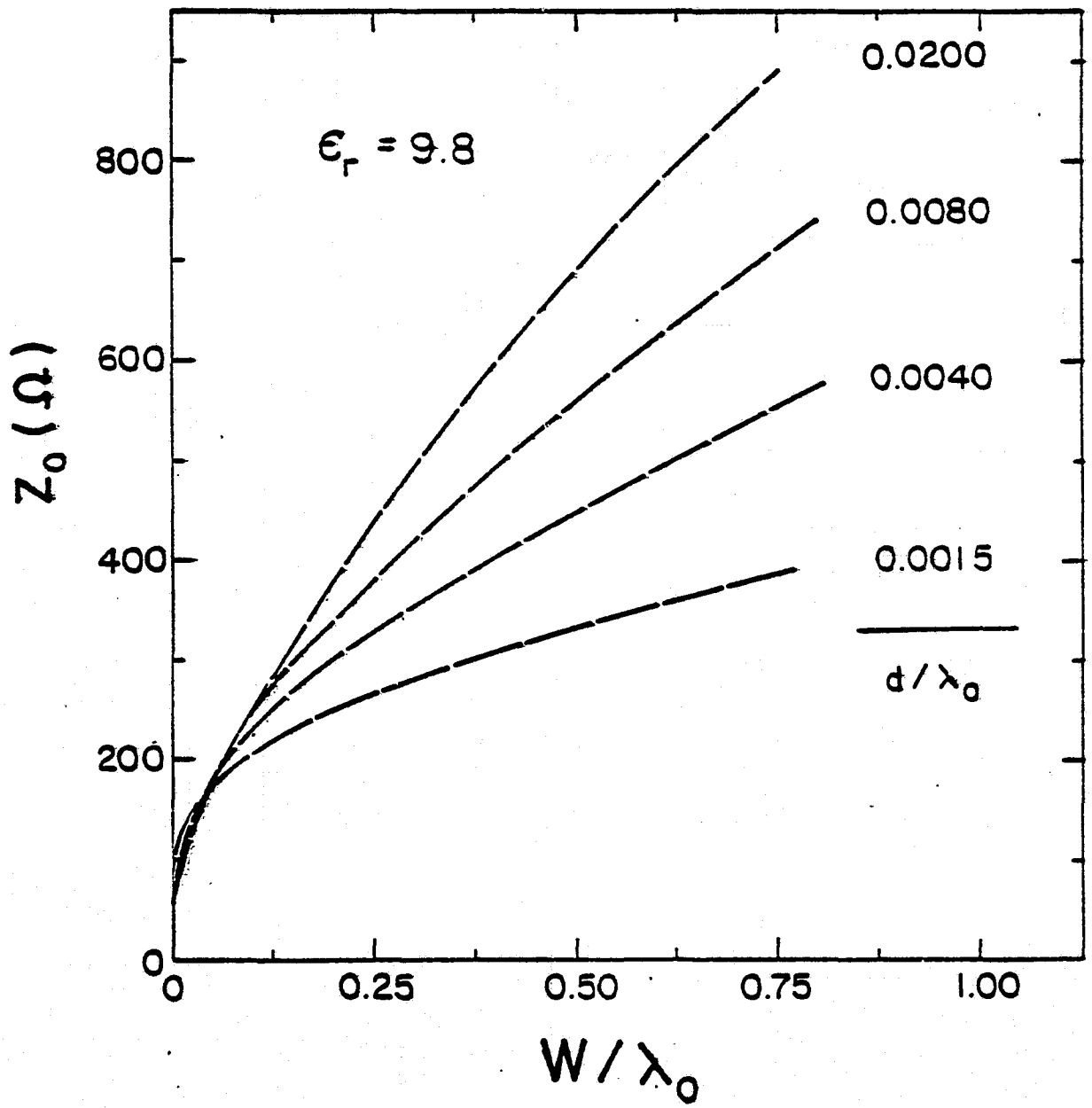
$\epsilon_r = 9.8$
0.0200
0.0080
0.0040
0.0015
d/λ_0
$Z_0(\Omega)$
800
600
400
200
0
0
0.25
0.50
0.75
1.00
W/λ_0

Fig. 2d

D3

N86-12481

APPENDIX III

ANALYSIS OF THE TEM MODE LINEARLY TAPERED SLOT ANTENNA

by

Ramakrishna Janaswamy

Daniel H. Schaubert

David M. Pozar

Department of Electrical and Computer Engineering

University of Massachusetts

Amherst, MA 01003

October 1985

This work was supported in part by NASA Langley Research Center under grant number NAG-1-279.

In this paper we present the theoretical analysis of the radiation characteristics of the TEM mode Linearly Tapered Slot Antenna (LTSA). The theory presented is valid for antennas with air dielectric and forms the basis for analysis of the more popular dielectric-supported antennas. The method of analysis involves two steps. In the first step, the aperture distribution in the flared slot is determined. In the second step, the equivalent magnetic current in the slot is treated as radiating in the presence of a conducting half-plane and the far-field components are obtained. Detailed comparison with experiment is made and excellent agreement is obtained. Design curves for the variation of the 3 dB and 10 dB beamwidths as a function of the antenna length, with the flare angle as a parameter, are presented.

1. INTRODUCTION

Over the past few years there has been an increasing interest in the use of planar antennas in microwave and millimeter wave integrated systems. The various kinds of planar antennas presently in use may be broadly divided into two classes; broadside and end-fire. Subsystems have been denveloped using broadside radiating elements such as printed dipoles and slots, microstrip patches, etc. [Kerr et al., 1977; Carver and Mink, 1981; Parrish et al., 1982; Rutledge, 1985]. These elements are all resonant structures yielding a 3 dB bandwidth of 10 - 15 % maximum. The element gain for all of these elements is fairly low, and does not suffice in applications where a 10 dB beamwidth of 12° - 60° is required [Yngvesson, 1983]. End-fire travelling wave antennas are included in the second class. Typical 10 dB beamwidths obtainable with these antennas range between 30° and 50° and thus

can be used directly in Cassegrain systems with f - numbers between 1 and 2 [Yngvesson, 1983]. The Linearly Tapered Slot Antenna (LTSA), which will be investigated here, belongs to the second class.

The tapered slot antenna consists of a tapered slot in a thin film of metal with or without an electrically thin dielectric substrate on one side of the film. The slot is very narrow towards one end for efficient coupling to devices such as mixer diodes. Away from this region, the slot is tapered so that the travelling wave propagating along the slot gradually radiates in the end-fire direction. Use of these antennas has so far been based on empirical designs. Gibson [1979] used an exponentially tapered slot antenna (he named it the 'Vivaldi' antenna) on an Alumina substrate in an 8 - 40 GHz video receiver module. He showed that the antenna is capable of producing a symmetric beam over a very wide bandwidth (3:1 bandwidth). Korzeniowski et al. [1983], developed an imaging system at 94 GHz using LTSA elements on a 1-mil Kapton substrate. The LTSA was first introduced by Prasad and Mahapatra [1979]. Their antenna was short ($\approx \lambda_0$) and etched on an Alumina substrate. Some preliminary experimental results on LTSAs were also published by Kollberg et al. [1983]. All these workers based their designs on empirical results, as no theory is yet available on these antennas. It is highly desirable to develop a suitable theoretical model for these antennas to facilitate successful designs. In this paper, we deal with the radiation pattern analysis of the LTSA. The theory considered is applicable only to the air dielectric LTSA (i.e., the TEM-LTSA). The case of an arbitrary taper (i.e., exponential, linear, constant, etc.) and dielectric substrate (thin) is also being treated by us and will be published in a future paper. The TEM-LTSA is simpler and direct to treat analytically but will nevertheless

shed light on the basic physics governing the radiation mechanism of this important class of end-fire travelling wave antennas. It forms the basis for analysis of the more popular dielectric-supported antennas.

Fig. 1a shows the geometry of the TEM-LTSA. The antenna radiates in the end-fire direction, i.e., along the negative X-axis with the E-field linearly polarized in the XZ-plane (copolar component). The method of analysis involves two steps. In the first step, the aperture distribution (i.e., electric field distribution) in the tapered slot is obtained. In the second step, the slot is treated as radiating in the presence of a conducting half plane (to account for the diffraction due to the edge cbb'c') and the far-field components are obtained.

The aperture distribution of the tapered slot is obtained in the following manner. The lateral edges cd and c'd' are far enough from the slot region that they have little effect on the field distribution in the slot. Hence they are receded to infinity. In addition, we employ the usual travelling wave antenna assumption that the aperture distribution on the structure is essentially determined by the propagating modes corresponding to the non-terminated structure. Note that this does not mean that we are ignoring the important diffraction effects due to the edge cbb'c' on the radiation pattern of the antenna. The effect of the termination of the structure at cbb'c' is incorporated by adding a backward travelling wave. The problem then reduces to finding the field distribution in the slot region for a tapered fin structure shown in Fig. 1b. The resulting structure, a pair of infinite coplanar "conical" fins, supports a spherical TEM wave (and hence the name TEM-LTSA) for which the scalar wave equation

can be solved exactly by employing the conformal mapping technique [Carrel, 1958].

The second step of the analysis is the determination of the fields radiated by the aperture distribution determined in step 1. As the tapered slot is extended right onto the edge cbb'c', it is expected that the edge diffraction will play a dominant role on the radiation pattern of the antenna. The edge diffraction is important because the radiation pattern of a slot in an infinite ground plane (i.e., without the edge being considered) has a null in the plane of the conductor (the E-plane). Hence, the E-plane pattern of the antenna is governed entirely by the currents induced on the metalization as a result of scattering off the edge. This important near field scattering effect will be rigorously taken into account by treating the tapered slot as radiating in the presence of a conducting half plane. Tai [1971] developed the exact theory of infinitesimal slots radiating in the presence of a conducting half plane by using the dyadic Green's function approach. Following his approach, an expression shall be obtained for the far-field due to an infinitesimal slot located on a conducting half plane. The radiation pattern of the LTSA will be found by integrating the aperture distribution found in step 1 over the slot region, with the expression found in step 2 as the kernel.

In section 2, we present the key steps involved in the formulation of the problem. In section 3, the computed radiation patterns of the LTSA are compared with the experimental results and design curves for the 3 dB and 10 dB beamwidths are presented.

2. FORMULATION OF THE PROBLEM

Fig. 1a shows the geometry of the TEM-LTSA and the coordinate system considered. As pointed out in section 1, the LTSA geometry is replaced by a pair of coplanar fins (Fig. 1b) for determining the aperture distribution in the slot. The resulting structure supports a spherical TEM wave [Carrel, 1958]. Carrel determined the characteristic impedance of this TEM line by employing a series of conformal transformations. Using the same transformations, it can be shown (see Appendix A for details) that the x and z-directed components of the electric field in the slot region are approximately given by

$$E_x^s(R,\alpha) \approx \frac{e^{-jk_oR}}{R} \frac{\sin\alpha}{\sqrt{\tan^2(\frac{\gamma}{2}) - \tan^2(\frac{\alpha}{2})}} \tag{1}$$

$$E_z^s(R,\alpha) \approx \frac{e^{-jk_oR}}{R} \frac{\cos\alpha}{\sqrt{\tan^2(\frac{\gamma}{2}) - \tan^2(\frac{\alpha}{2})}} \tag{2}$$

where (R,α) are the polar coordinates in the plane of the slot with the vertex of the LTSA at the origin and 2γ is the flare angle of the LTSA. We shall, however, be concerned with only the z-directed slot field for the following reasons: It can be shown [Tai, 1971] from the analysis of infinitesimal slots radiating in the presence of a conducting half plane that the longitudinal slot field E_x^s does not contribute to the far-field in either principal plane. This may be explained physically as follows. E_x^s is an odd function of z, hence the far-field due to it has a null in the XY-plane (the H-Plane). The far-field component in any plane is composed of two

terms. The first term may be labelled the 'direct field' i.e., field in the absence of the edge cbb'c'. The second term arises as a result of scattering due to the edge cbb'c'. Both the incident field and the scattered field due to E_x^s are normal to the edge i.e., along the Y-axis and contribute only to the cross-polarized component in the E-plane. Henceforth, we shall be concerned with only the z-directed slot field and shall be referring to it as the aperture distribution E_a i.e.,

$$E_a(R,\alpha) = E_z^s(R,\alpha) = \frac{e^{-jk_oR}}{R} \frac{\cos\alpha}{\sqrt{\tan^2(\frac{\gamma}{2}) - \tan^2(\frac{\alpha}{2})}}, \quad -\gamma \leq \alpha \leq \gamma \qquad (3)$$

Employing the dyadic Green's function approach, it can be shown that the far-field component $e_\theta(\theta,\phi)$ at the observation angles (θ,ϕ), due to a horizontal infinitesimal slot located at (x',z') on a conducting half plane is given by

$$e_\theta(\theta,\phi) = |\sin\phi| e^{j\pi/4} F(v) e^{+jk_o(x'\sin\theta\cos\phi + z'\cos\theta)} + \sin(\phi/2) e^{-j[\pi/4 + k_o(x'\sin\theta - z'\cos\theta)]} \Big/ \sqrt{\pi k_o x'\sin\theta}, \quad (\theta \neq 0,\pi) \qquad (4)$$

where,

$$v = k_o x'\sin\theta(1+\cos\phi)$$

$$F(v) = \int_0^v \frac{e^{-jt}}{\sqrt{2\pi t}}\, dt \qquad \text{(Fresnel Integral)} \qquad (5)$$

Note that $\lim_{v\to\infty} e^{j\pi/4} F(v) = 1/\sqrt{2}$

Substituting $z' = 0$ and $\theta = \pi/2$ in the expression for e_θ, it is seen that (4) reduces to equation 35.11 of [Tai, 1971].

We observe from (4) that the magnitude of the second term decays to zero as $k_o x' \to \infty$ ($\theta \neq 0,\pi$ as the asymptotic far-field expression is not valid

for $\theta=0,\pi$) and that e_θ is dominated by the first term, which in this case reduces to the familiar far-field kernel due to a slot in an infinite ground plane. Consequently, we may interpret the first term as the 'direct field' and the second term as the 'edge diffracted field'. In the E-plane, $\phi = \pi$, and it is seen from (4) that the direct field is identically zero and the far-field is contributed entirely by the edge diffracted field.

The far-zone field E_θ of the LTSA is obtained by integrating the aperture distribution E_a over the tapered slot S', with e_θ as the kernel i.e.,

$$E_\theta = \iint_{S'} e_\theta \, E_a \, ds' \tag{6}$$

It is shown in Appendix B that for shallow taper angles γ, the two dimensional integral in (6) may be reduced to a one dimensional integral. The result (suppressing the common phase factor and constants) is given by

$$E_\theta(\theta,\phi) = \sin\phi \int_{-\gamma}^{\gamma} \frac{\cos\alpha}{\sqrt{\tan^2(\frac{\gamma}{2}) - \tan^2(\frac{\alpha}{2})}} d\alpha \cdot \frac{1}{v_1}\left[F(v_2) - e^{-jv_1} F\{v_2(1-\cos\alpha)\}\right.$$
$$\left. + \sqrt{(\frac{v_3}{v_2})}\, e^{-jv_1\sec\alpha} \{F(v_3) - F\{v_3(1-\cos\alpha)\}\}^*\right] \tag{7}$$

where $F(.)$ is the Fresnel integral given by (5) and

$$v_1 = k_o L(1+\sin\theta\cos\phi\cos\alpha-\cos\theta\sin\alpha)$$

$$v_2 = k_o L\sin\theta(1+\cos\phi)$$

$$v_3 = k_o L\sec\alpha(1-\sin(\theta+\alpha))$$

and * denotes the complex conjugate.

Note that the E-plane pattern ($\phi = \pi$) is obtained from (7) by taking the limit as $\phi \to \pi$. In this case, we also have $v_2 = 0$ and $v_1 = v_3\cos\alpha$. On carrying out these steps, the E-plane electric field $E_E(\theta)$ is obtained as

$$E_E(\theta) = \int_{-\gamma}^{\gamma} \sqrt{\frac{2\cos\alpha(1-\sin(\theta+\alpha))}{\tan^2(\frac{\gamma}{2}) - \tan^2(\frac{\alpha}{2})}} \cdot e^{-jv_3} [F(v_3) - F\{v_3(1-\cos\alpha)\}]^* \, d\alpha \tag{8}$$

3. DISCUSSION OF THE COMPUTED AND THE EXPERIMENTAL RESULTS

The integral in (7) must be evaluated numerically. The singularity in the integrand as $\alpha \to \pm \Upsilon$ is removable and poses no problems in the numerical integration. Radiation patterns for the LTSA have been computed for lengths L/λ_o ranging between 3 and 10 and for flare angles between 8° and 21°.

The aperture distribution given in (7) includes only the forward travelling wave. To study the effects of the wave reflected at the aperture termination $X = 0$ on the radiation pattern of the antenna, a reflected wave was introduced in the aperture distribution and the voltage reflection coefficient Γ was varied over all the possible values i.e., $-1 \leq \Gamma \leq 1$. Patterns were computed for various combinations of L and 2Υ. Figs. 2a and 2b illustrate the effect of including a reflected wave on the aperture distribution for $L/\lambda_o = 3$ and 10 respectively, with Γ as a parameter. The cases of $\Gamma = \pm 1$ correspond to a uniform phase distribution on the aperture (i.e., a pure standing wave) and would have resulted in a broadside pattern with the maximum occuring along the Y-axis, had the aperture been radiating in free space. However, currents are induced on the metalization as a result of near-field scattering off the edge cbb'c'. These induced currents radiate in the end-fire direction as evidenced by the second term in equation (4). The radiated fields of the LTSA are dominated by those produced by the induced currents. This is clear from the end-fire nature of th H-plane pattern of the antenna as shown in Figs. 2a and 2b. Also, it is seen that the influence of the reflected wave on the forward lobe is not very critical and diminishes as the length of the antenna is increased. The front lobe of the radiation pattern for a long antenna is almost entirely decided by the

forward travelling wave. In all the subsequent patterns, only a forward travelling wave, as given in (7), is assumed for the aperture distribution.

The computed patterns in the E and the H-planes with $L/\lambda_o = 5$ and $2\Upsilon = 15^\circ$ are shown in Fig. 3a. Corresponding experimental patterns are shown in Figs. 3b and 3c. The experimental model was built using a 5-mil brass sheet with D = 11.0cm (the LTSA half height). A microwave diode (HP-5082-2215) was connected across the feed gap to detect the RF signal. The antenna was supported by using 1/2" styrofoam ($\varepsilon_r = 1.02$) strips along the outer boundary dd'c'cd of the antenna. Table I summarizes the comparison between the theory and experiment. It is seen that excellent agreement is obtained between the two for all the important aspects of the pattern viz., the 3 dB and the 10 dB beamwidths, locations of the minima and the sidelobe level. Figs. 4a-4c show the computed and the experimental patterns for a TEM-LTSA with $2\Upsilon = 11.9^\circ$ and $L/\lambda_o = 8$. Table II summarizes the comparison between the two. Again there is a very good agreement between the two. Figs 5a and 5b show the comparison of the 3 dB beamwidth between theory and experiment for 2Υ varying between 8° and 21° and for $L/\lambda_o = 5.0$ and 6.33 respectively. The H-plane beamwidth is relatively insensitive to the flare angle of the antenna. The beamwidth can, however, be controlled by varying the length of the antenna. In all the cases tested, the LTSA half height D satisfied $D \geq 2.75\lambda_o$ and $D/W_o \geq 3.3$, where $W_o = L\tan\Upsilon$. Restriction is placed on D so that comparison with the theory (which assumes infinite D) is meaningful. The slight ripples seen in the E-plane experimental patterns are attributed to the lateral truncation effects (i.e., finite D).

The computed 3 dB and 10 dB beamwidths of the LTSA in the E-plane and the H-plane as a function of L/λ_o and with 2Υ as a parameter are plotted in

Figs. 6a and 6b respectively. Important design parameters for the antenna in the E-Plane are both the flare angle and the length, whereas in the H-Plane, the pattern is relatively insensitive to the flare angle and is controlled only by varying the antenna length.

4. CONCLUSION

Radiation pattern analysis of the TEM-LTSA has been presented. The method of analysis involves two steps: In the first step, the electric field distribution in the tapered slot is determined by using the conformal mapping technique. In the second step, the equivalent magnetic current in the tapered slot is treated as radiating in the presence of a conducting half plane to rigorously account for near field scattering by the edge, and the far-fields are obtained. Comparison is made between theory and experiment and it is shown that excellent agreement is obtained over the entire range considered: $3 \leq L/\lambda_o \leq 10$ and $8^\circ \leq 2\gamma \leq 21^\circ$. Finally, design curves for the variation of beamwidths as a function of the normalized length, with the flare angle as a parameter, are presented.

Appendix A:

DERIVATION OF THE APERTURE DISTRIBUTION FOR THE TAPERED SLOT

In this section, we shall obtain an expression for the aperture distribution in the tapered slot region by first treating the associated infinite coplanar fin problem.

Fig. A1 shows the geometry of a coplanar fin structure formed by a zero thickness perfect electric conductor. Note that the coordinate system in this section is different from the one introduced in the main text. We would like to solve for the electric and magnetic fields E and H for this structure and later specialize to the slot region to obtain the aperture distribution in the tapered slot. Since the structure is multiply connected and has the same boundary for all 'r' (the spherical coordinate), it supports a spherical TEM wave. Adopting $e^{j\omega t}$ time convention, it follows from Maxwell's equations that a spherical TEM wave can be represented as

$$E = - e^{-jk_o r} \nabla_t \Psi \tag{A1}$$

where the scalar potential Ψ satisfies $\nabla_t^2 \Psi = 0$ and the subscript 't' denotes that the gradient operator is defined with respect to the tranverse i.e.,(θ,ϕ) coordinates. k_o is the free space propagation constant. Following Carrel, the scalar potential Ψ, after dropping the constant factors, is given by

$$\Psi = \int_0^{\sigma} \frac{d\sigma}{\sqrt{(1-\sigma^2)(1-\tau^2\sigma^2)}} \tag{A2}$$

where $\tau = \tan(\gamma/2)$ and $\sigma = \frac{1}{\tau} \tan(\theta/2)\, e^{j\phi}$.

The electric field distribution E^s in the slot is obtained from (A1) and (A2) and specializing to the case of $\phi = 0, \pi$. The final expression after carrying out the above operations is given by

$$E^s(r,\theta) = -e^{-jk_o r}\,\nabla_t\Psi\big|_{\phi=0,\pi} = -\hat{\theta}\,\frac{e^{-jk_o r}}{r}\cdot\frac{\sec^2(\theta/2)}{\sqrt{\tan^2(\frac{\gamma}{2})-\tan^2(\frac{\theta}{2})}}\cdot$$

$$\cdot\frac{1}{\sqrt{1-\tan^2(\frac{\theta}{2})}}, \quad |\theta| \le \gamma \qquad (A3)$$

where $\hat{\theta}$ is the unit normal in the θ-direction. In obtaining (A3), the Riemann sheet corresponding to $\sqrt{1} = +1$ is chosen. The term under the first radical sign in (A3) arises as a result of the edges at $\theta = \gamma$ and the second is due to those at $\theta = \pi/2$. For shallow taper angles γ, the edges at $\theta = \pi/2$ do not effect the field distribution in the tapered slot much and the following approximations are valid,

$$\sec^2(\theta/2) \approx 1 \quad \text{and} \quad \sqrt{(1-\tan^2(\theta/2)} \approx 1$$

Using these in (A3), and decomposing the resulting slot field into x and z components in the coordinate system introduced in section 2, we get,

$$E_x^s(R,\alpha) = \frac{e^{-jk_o R}}{R}\,\frac{\sin\alpha}{\sqrt{\tan^2(\frac{\gamma}{2})-\tan^2(\frac{\alpha}{2})}}, \quad |\alpha| \le \gamma \qquad (A4)$$

$$E_z^s(R,\alpha) = \frac{e^{-jk_o R}}{R}\,\frac{\cos\alpha}{\sqrt{\tan^2(\frac{\gamma}{2})-\tan^2(\frac{\alpha}{2})}}, \quad |\alpha| \le \gamma \qquad (A5)$$

Appendix B:

DERIVATION OF THE FAR-ZONE ELECTRIC FIELD OF THE TEM-LTSA

We have from equation (6) of section 2,

$$E_\theta = \iint_{S'} e_\theta \, E_a \, ds' \tag{B1}$$

where S' is the area occupied by the tapered slot. For shallow taper angles, the triangular region S' may be approximated by the circular sector of radius L and included angle 2γ. Hence,

$$E_\theta = \int_{-\gamma}^{\gamma} \int_{0}^{L} e_\theta \, E_a \, R \, dR \, d\theta \tag{B2}$$

The polar coordinates (R,α) referred to the vertex of the LTSA and the source coordinates (x',z') with respect to the coordinate system shown in Fig. 1a are related as $x' = L - R\cos\alpha$, $z' = R\sin\alpha$. Combining (3), (4) and (B2), we see that,

$$E_\theta = \int_{-\gamma}^{\gamma} \frac{\cos\alpha \, d\alpha}{\sqrt{\tan^2(\frac{\gamma}{2}) - \tan^2(\frac{\alpha}{2})}} \cdot \int_{0}^{L} \Big\{ |\sin\phi| F(v) \, e^{jk_o L\sin\theta\cos\phi} \cdot e^{-jk_o R(1+\sin\theta\cos\phi\cos\alpha-\cos\theta\sin\alpha)} \cdot e^{-jk_o R(1-\sin(\theta+\alpha))} \Big\} \, dR$$

$$- j\frac{\sin(\phi/2) \, e^{-jk_o L\sin\theta}}{\sqrt{\pi k_o \sin\theta (L-R\cos\alpha)}} \tag{B3}$$

where $v = k_o\sin\theta(1+\cos\phi)(L-R\cos\alpha)$

and $$F(v) = \int_{0}^{v} \frac{e^{-jt}}{\sqrt{2\pi t}} \, dt \tag{B4}$$

The integral over R in (B3) can be evaluated in closed form. Consider first the integral I_1 of the first term in the inner integral of (B3),

$$I_1 = |\sin\phi| \, e^{jk_o L\sin\theta\cos\phi} \cdot \int_{0}^{L} F(v) \, e^{-jk_o R(1+\sin\phi\cos\theta\cos\alpha-\cos\theta\sin\alpha)} \, dR$$

We integrate I_1 by parts and cast the resulting integral in a form suitable for defining it in terms of the Fresnel integral. The final result after carrying out the required manipulations is

$$I_1 = \frac{-jL|\sin\phi|\, e^{jk_0L\sin\theta\cos\phi}}{v_1}\left[F(v_2) - e^{-jv_1}F(v_2(1-\cos\alpha)) - \sqrt{\left(\frac{v_2}{v_3}\right)}\cdot\right.$$

$$\left.\cdot e^{-jv_1\sec\alpha}\{F(v_3) - F(v_3(1-\cos\alpha))\}^*\right]$$

where $v_1 = k_0L(1+\sin\theta\cos\phi\cos\alpha-\cos\theta\sin\alpha)$

$$v_2 = k_0L\sin\theta(1+\cos\phi) \qquad \} \qquad \text{(B5)}$$

$$v_3 = k_0L\sec\alpha(1-\sin(\theta+\alpha)$$

The integral I_2 involving the second term in (B3) may also be evaluated in closed form as follows:

$$I_2 = -j\frac{\sin(\phi/2)\, e^{-jk_0L\sin\theta}}{\sqrt{\pi k_0\sin\theta}}\int_0^L \frac{e^{jk_0R(1-\sin(\theta+\alpha))}}{\sqrt{L - R\cos\alpha}}\, dR$$

Letting $L-R\cos\alpha = u$ and simplifying, we get,

$$I_2 = -j\frac{\sin(\phi/2)\, e^{-jk_0L(1-\cos\theta\sin\alpha)\sec\alpha}}{\cos\alpha\sqrt{\pi k_0\sin\theta}}\cdot\int_{L(1-\cos\alpha)}^{L}\frac{e^{jk_0u(1-\sin(\theta+\alpha)\sec\alpha}}{\sqrt{u}}\, du$$

Introducing a second change of variable $p = k_0u(1-\sin(\theta+\alpha))\sec\alpha$, and evaluating the resulting integral, I_2 may be expressed in a closed form as

$$I_2 = -jL\sin\phi\sec\alpha e^{-j(k_0L\sin\theta+v_3)}\sqrt{\left(\frac{1}{v_2v_3}\right)}\cdot\left[F(v_3) - F(v_3(1-\cos\alpha))\right]^*$$

Substituting for I_1 and I_2 in (B3) and noting that $|\sin\phi| = \sin\phi$, $0 \le \phi \le \pi$, and simplifying the resulting expression, we get, for $0 \le \phi \le \pi$,

$$E_\theta(\theta,\phi) = -jL\, e^{jk_0L\sin\theta\cos\phi}\sin\phi\int_{-\gamma}^{\gamma}\frac{\cos\alpha\, d\alpha}{\sqrt{\tan^2\left(\frac{\gamma}{2}\right) - \tan^2\left(\frac{\alpha}{2}\right)}}\cdot\frac{1}{v_1}\left[F(v_2) - \right.$$

$$\left. e^{-jv_1}F(v_2(1-\cos\alpha)) + \sqrt{\left(\frac{v_3}{v_2}\right)}e^{-jv_1\sec\alpha}\cdot\right.$$

$$\left.\cdot\{F(v_3) - F(v_3(1-\cos\alpha))\}^*\right] \qquad \text{(B6)}$$

where F(.) is the Fresnel integral defined in (B4) and v_1, v_2 and v_3 are given in (B5)

REFERENCES

Carrel, R.L., The Characteristic Impedance of Two Infinite Cones of Arbitrary Cross Section, IRE Trans. Antennas Propogat, Vol. AP-6(2), 197-201, 1958.

Carver, K.R. and Mink, J.W., Microstrip Antenna Technology, IEEE Trans. Antennas Propagat, Vol. AP-29(1), 2-24, 1981.

Gibson, P.J., The Vivaldi Aerial, Proc. Eur. Microwave Conf., 9th, Brighton, U.K., 101-105, 1979.

Kerr, A.R., et al., A Simple Quasi-optical GaAs Monolithic Mixer at 110 GHz, 1977 IEEE MTT-S International Microwave Symposium Digest, San Diego, CA., 96-98, 1977.

Kollberg, E.L., et al., New Results on Tapered Slot Endfire Antennas on Dielectric Substrates, 1983 IEEE Int. Conference on Infrared and Millimeter Waves Digest, Miami Beach, FLA., F3.6, 1983.

Korzeiowski, T.L. et al., Imaging System at 94 GHz Using Tapered Slot Antenna Elements, paper presented at the 8th IEEE Int. Conference on Infrared and Millimeter Waves, Miami Beach, FLA., 1983.

Parrish, P.T. et al., Printed Dipole-Schottky Diode Millimeter Wave Antenna Array, SPIE Proc., 337, Millimeter Wave Technology, 49-52, 1982.

Prasad, S.N. and Mahapatra, S., A novel MIC slot-line Aerial, Proc. Eur. Microwave Conf., 9th, Brighton, U.K., 120-124, 1979.

Rutledge, D.B., (Feature Article), IEEE Antennas Propagat. Soc. Newsletter, Vol. 27(4), 1985.

Tai, C.T., Dyadic Green's Functions in Electromagnetic Theory, Intext Educational Pulishers, Scranton, Pennsylvania, 1971.

Yngvesson, K.S, Near-Millimeter Imaging with Integrated Planar Receptors: General Requirements and Constraints in Infrared and Millimeter Waves, vol. 10, edited by K.J. Button, Academic Press, New York, 1979.

FIGURE TITLES

1a. Geometry of the TEM-LTSA and the coordinate system.

1b. Geometry of the coplanar fin structure.

2. Variation of the principal plane patterns as a function of the load reflection coefficient Γ. a) $L/\lambda_o = 3.0$ b) $L/\lambda_o = 10.0$

3. Comparison of the radiation pattern between the theory and experiment. $L/\lambda_o = 5.0$, $2\Upsilon = 15.0^\circ$. a) Theory. b) E-Plane(Exp.) c) H-Plane (Exp.).

4. Comparison of the radiation pattern between the theory and experiment. $L/\lambda_o = 8.0$, $2\Upsilon = 11.9^\circ$. a) Theory. b) E-Plane (Exp.). c) H-Plane (Exp.).

5. Comparison of the 3 dB beamwidth between the theory and experiment. a) $L/\lambda_o = 5.0$ b) $L/\lambda_o = 6.3$.

6. Variation of the beamwidths of the TEM-LTSA as a function of the antenna length, with the flare angle as a parameter. a) E-Plane b) H-Plane.

A1. Geometry of the coplanar fin structure and the coordinate system.

Table I

Comparison of Pattern Between the Theory and Experiment

$L/\lambda_o = 5.0$; $2\Upsilon = 15^o$

	Beamwidth (Deg)		Side Lobe Level (dB)	Location of the First Minimum (Deg)
	3dB	10dB		
E-Plane				
Theory	36.5	55	-15	38
Exp.	34.2	57	-14	35
H-Plane				
Theory	47.0	67	-9.0	34.5
Exp.	45.5	72	-9.5	35.0

Table II

Comparison of Pattern Between the Theory and Experiment

$L/\lambda_o = 8.0$; $2\Upsilon = 11.9^o$

	Beamwidth (Deg)		Side Lobe Level (dB)	Location of the First Minimum (Deg)
	3dB	10dB		
E-Plane				
Theory	29	43	-16	33
Exp.	30	45	-15	30
H-Plane				
Theory	38	51.4	-9.0	32
Exp.	35	47.0	-7.5	30

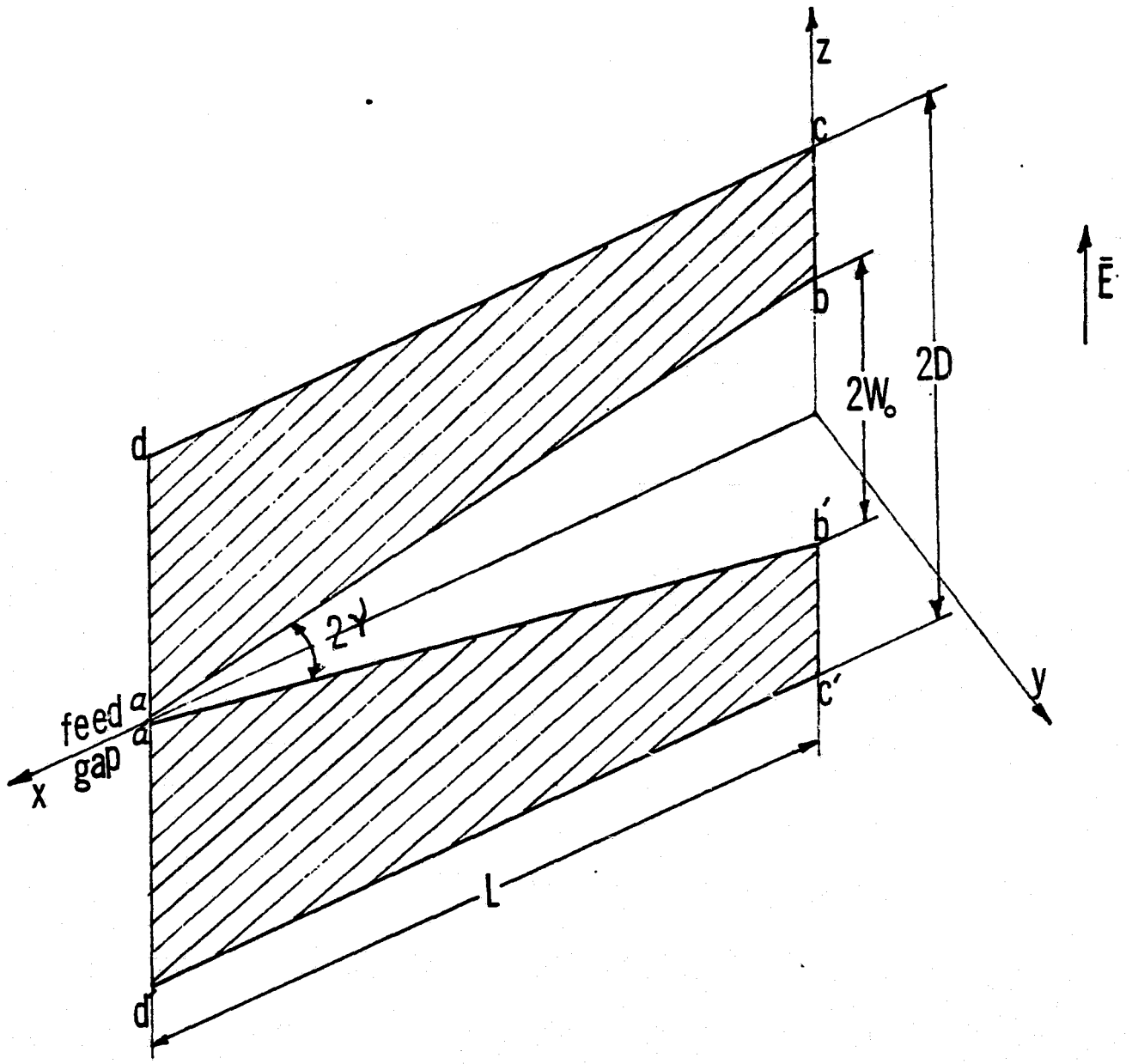

FIG. 1a

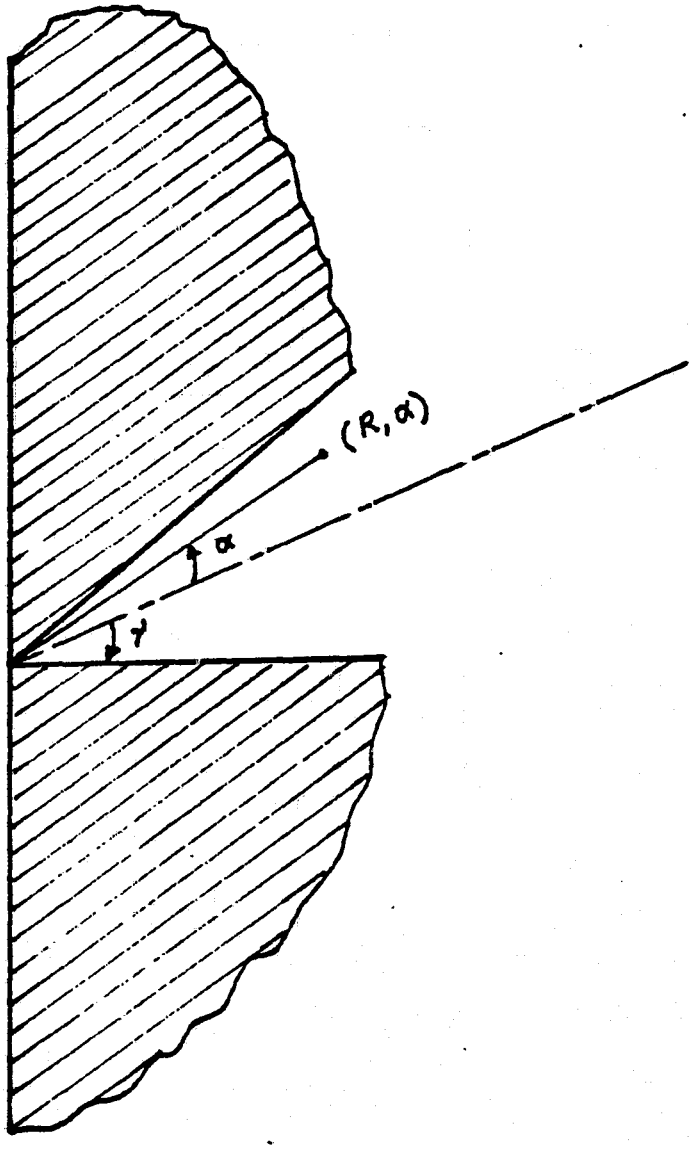

FIG. 1b

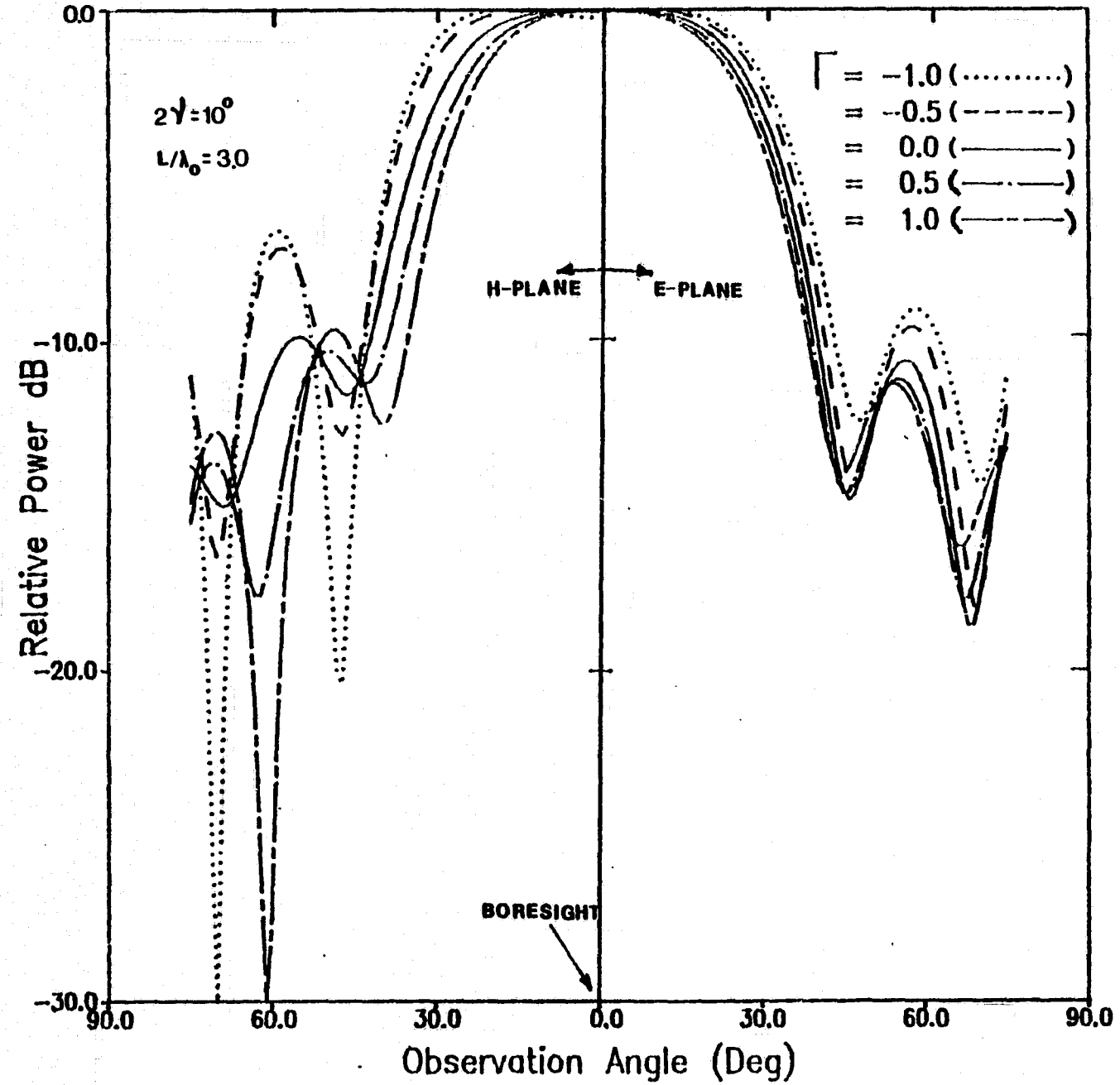
0.0
-10.0
-20.0
-30.0
Relative Power dB
2ψ=10°
L/λ₀=3.0
Γ = -1.0 (.....)
= -0.5 (- - - - -)
= 0.0 (————)
= 0.5 (—·—)
= 1.0 (— — —)
H-PLANE
E-PLANE
BORESIGHT
90.0
60.0
30.0
0.0
30.0
60.0
90.0
Observation Angle (Deg)

FIG. 2a

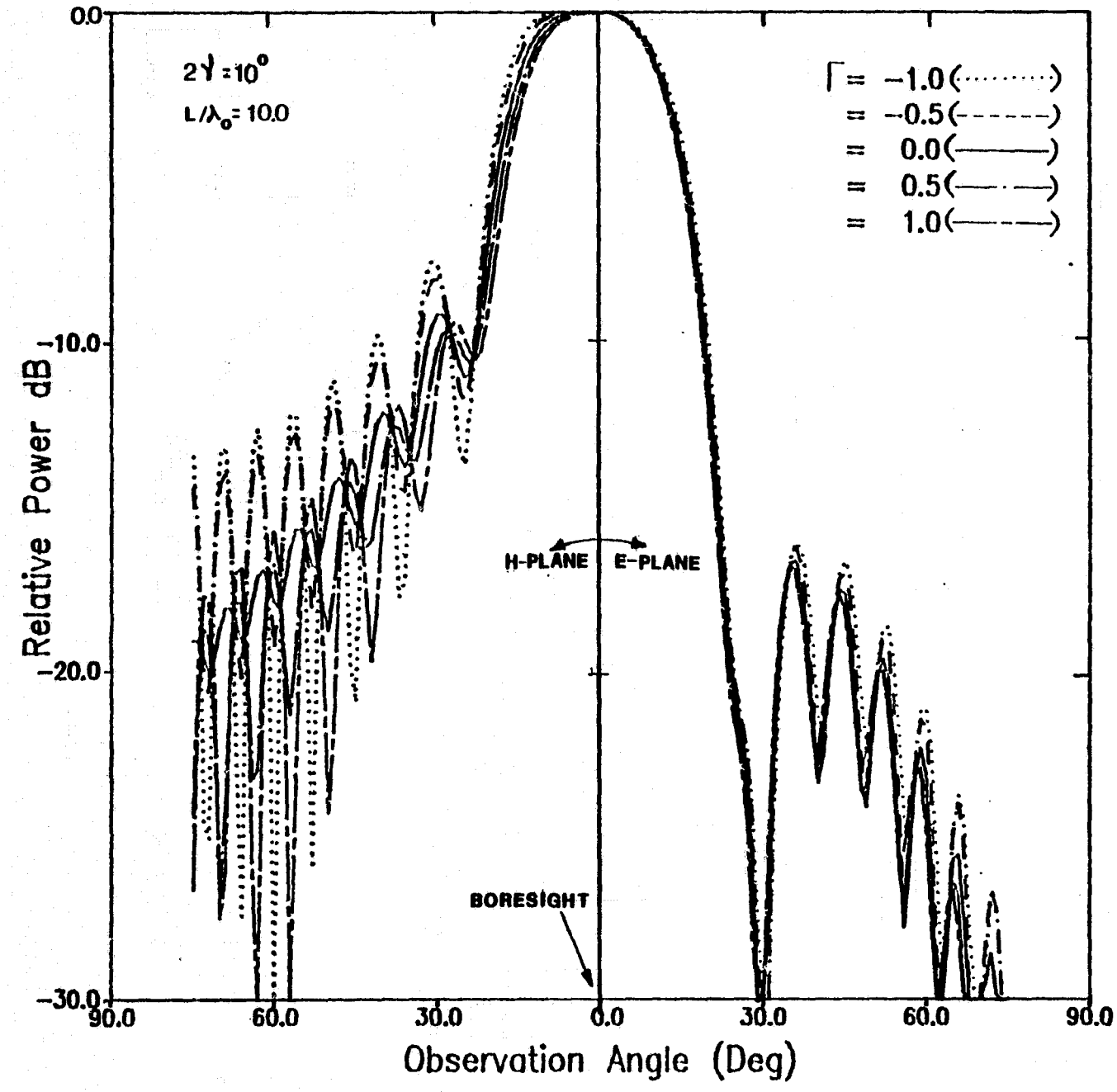
0.0
-10.0
-20.0
-30.0
2Ψ = 10°
L/λ₀ = 10.0
Γ = -1.0 (·····)
= -0.5 (- - - - -)
= 0.0 (———)
= 0.5 (—·—)
= 1.0 (— — —)
H-PLANE
E-PLANE
BORESIGHT
Relative Power dB
90.0
60.0
30.0
0.0
30.0
60.0
90.0
Observation Angle (Deg)

FIG. 2b

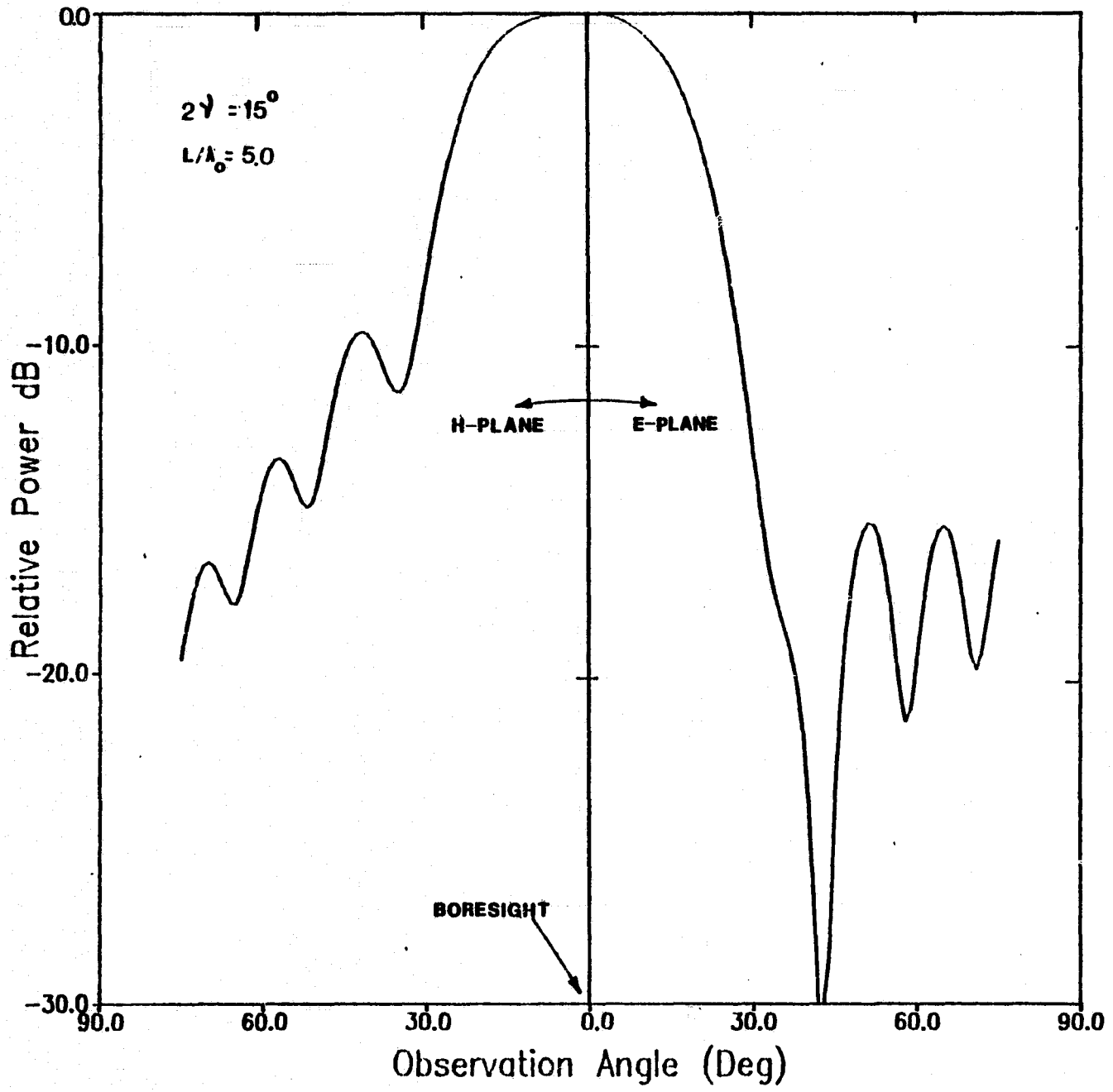
0.0
-10.0
-20.0
-30.0
2ψ = 15°
L/λ₀ = 5.0
H-PLANE
E-PLANE
BORESIGHT
Relative Power dB
90.0
60.0
30.0
0.0
30.0
60.0
90.0
Observation Angle (Deg)

FIG. 3a

ORIGINAL PAGE IS
OF POOR QUALITY

RECTANGULAR POWER PATTERN IN dB

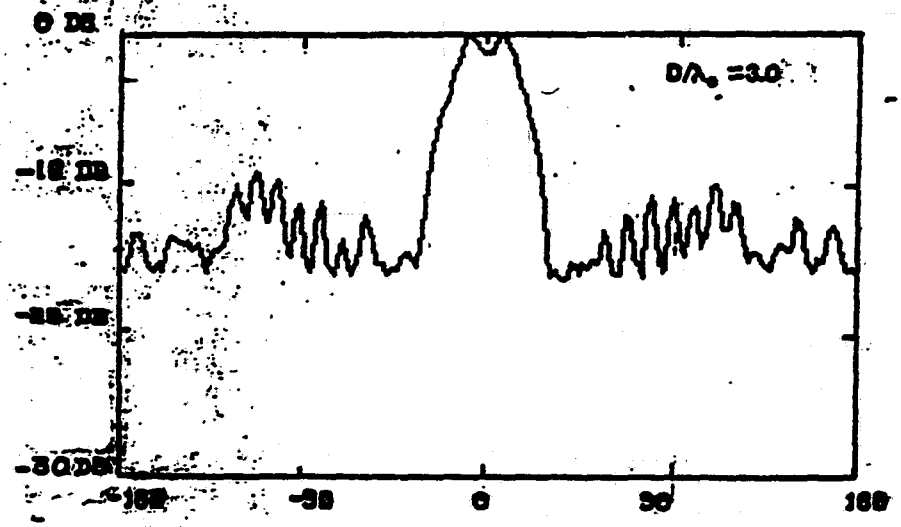

RECTANGULAR POWER PATTERN IN dB

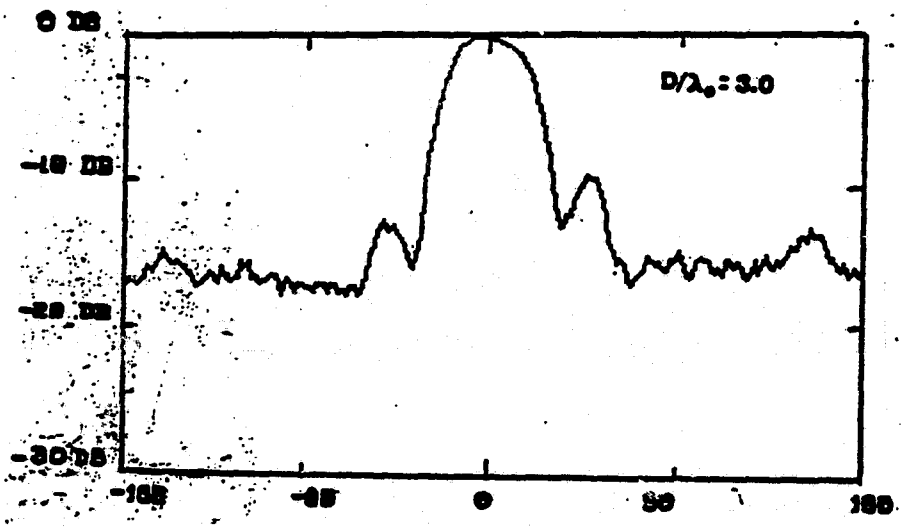

FIGs. 3b & 3c

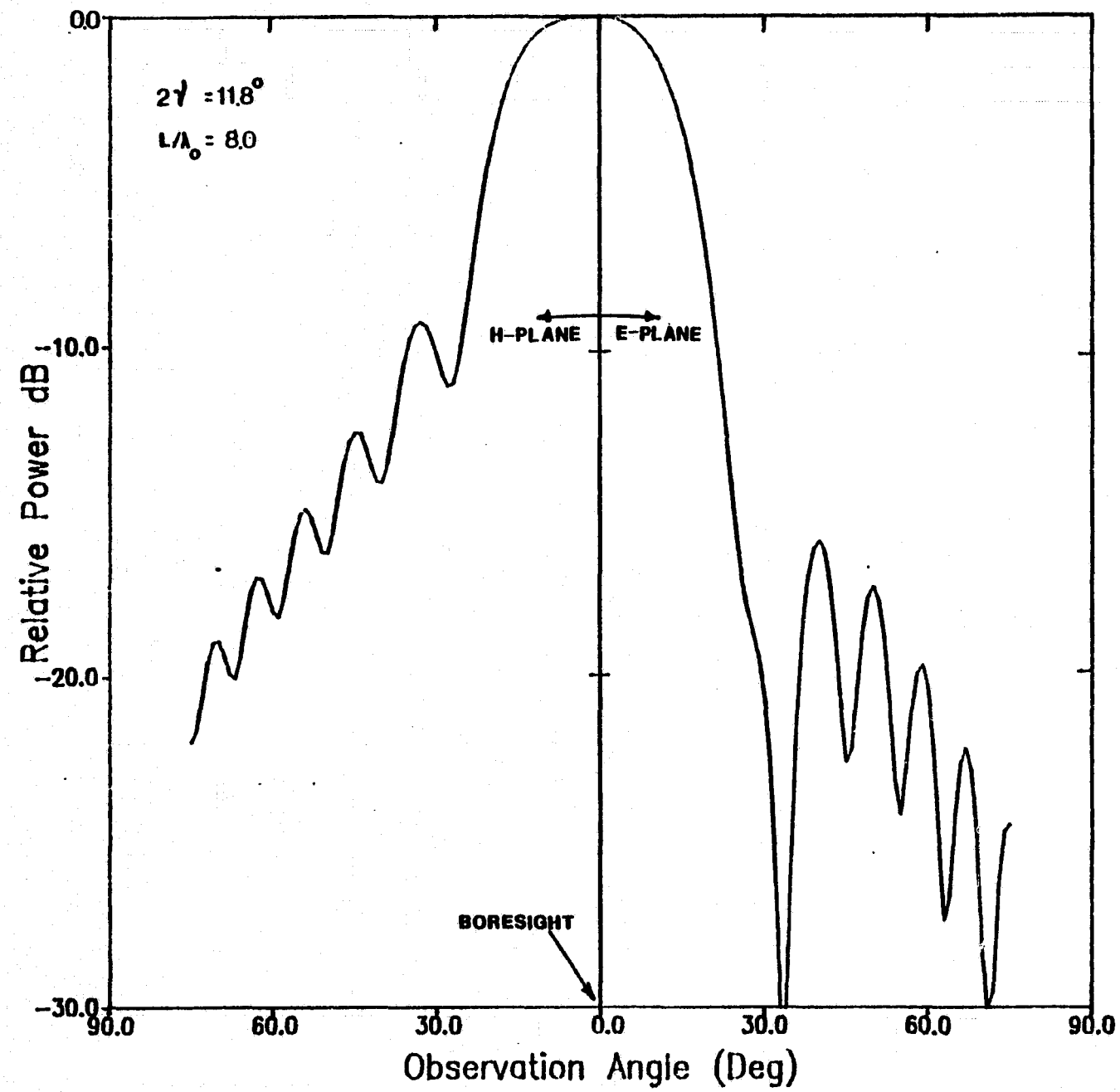
0.0
-10.0
-20.0
-30.0
2γ =11.8°
L/λ0 = 8.0
H-PLANE
E-PLANE
BORESIGHT
Relative Power dB
90.0
60.0
30.0
0.0
30.0
60.0
90.0
Observation Angle (Deg)

FIG. 4a

RECTANGULAR POWER PATTERN IN dB

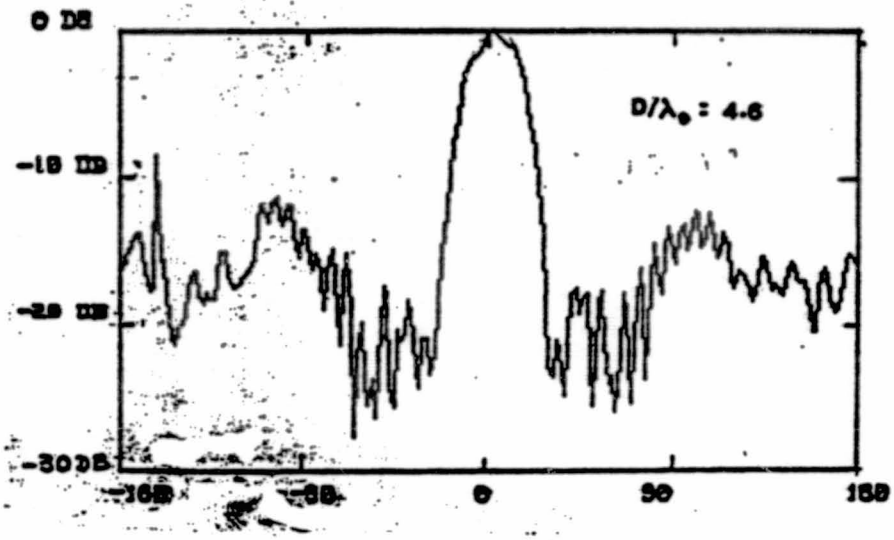

RECTANGULAR POWER PATTERN IN dB

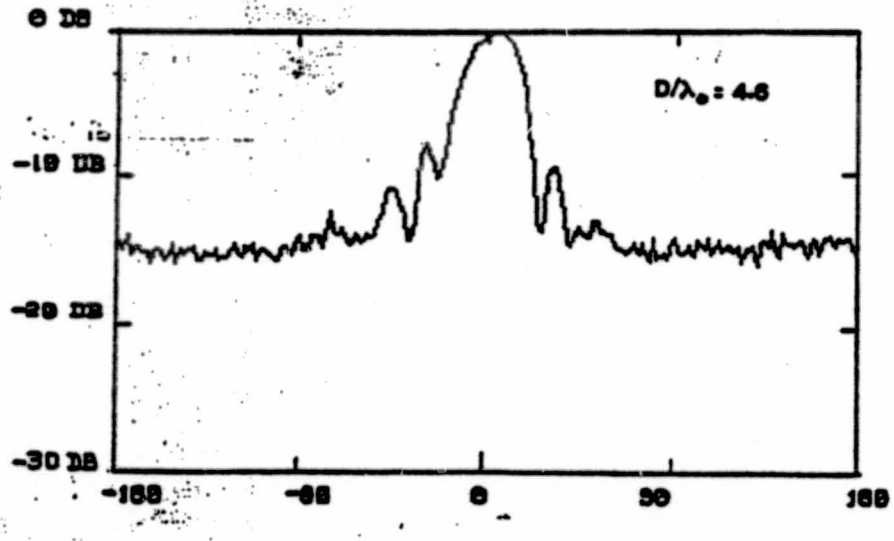

FIGS 4b & 4c.

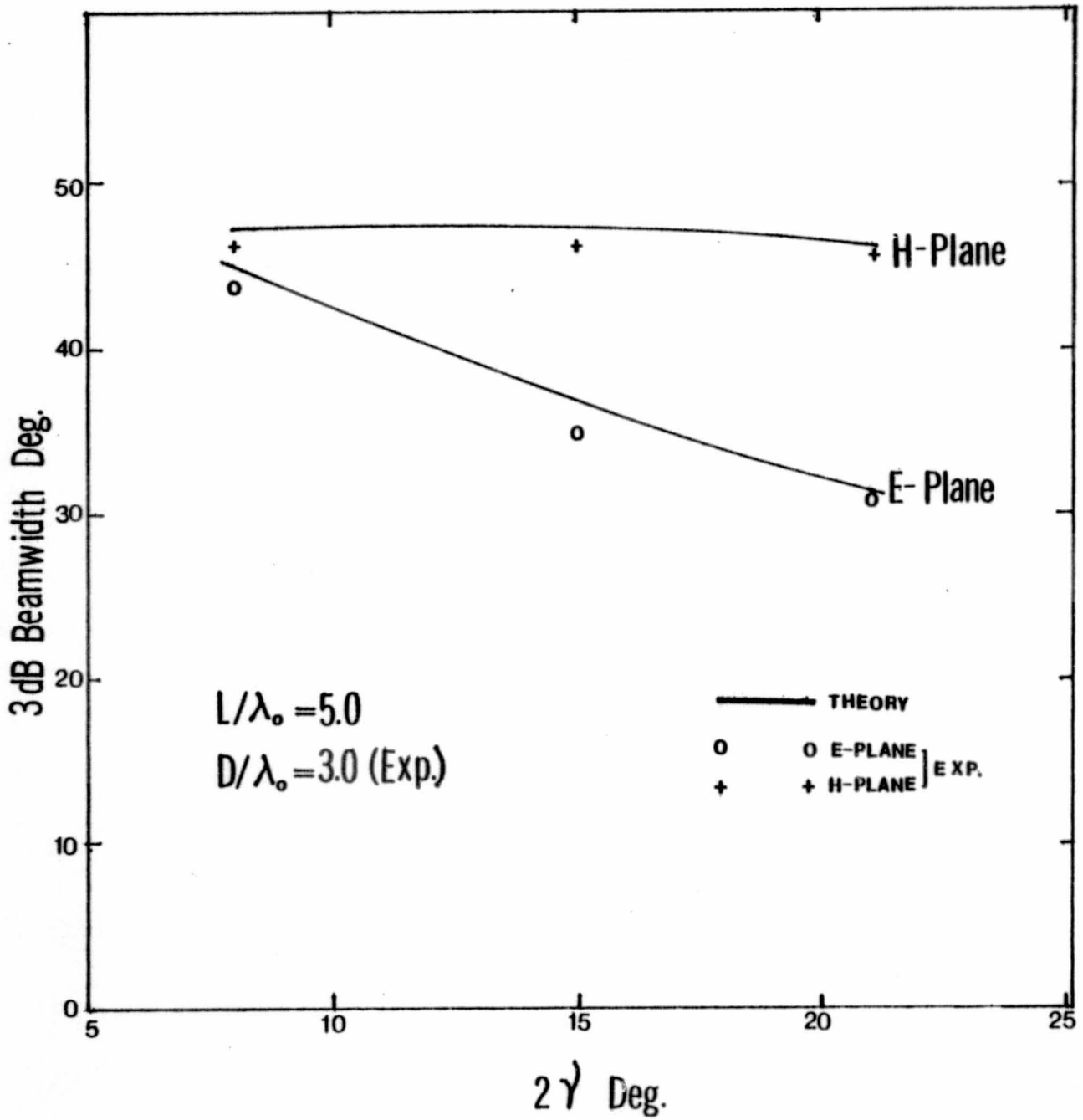
3dB Beamwidth Deg.
50
40
30
20
10
0
5
10
15
20
25
2γ Deg.
H-Plane
E- Plane
L/λ₀ =5.0
D/λ₀ =3.0 (Exp.)
THEORY
O E-PLANE
+ H-PLANE
EXP.

FIG. 5a

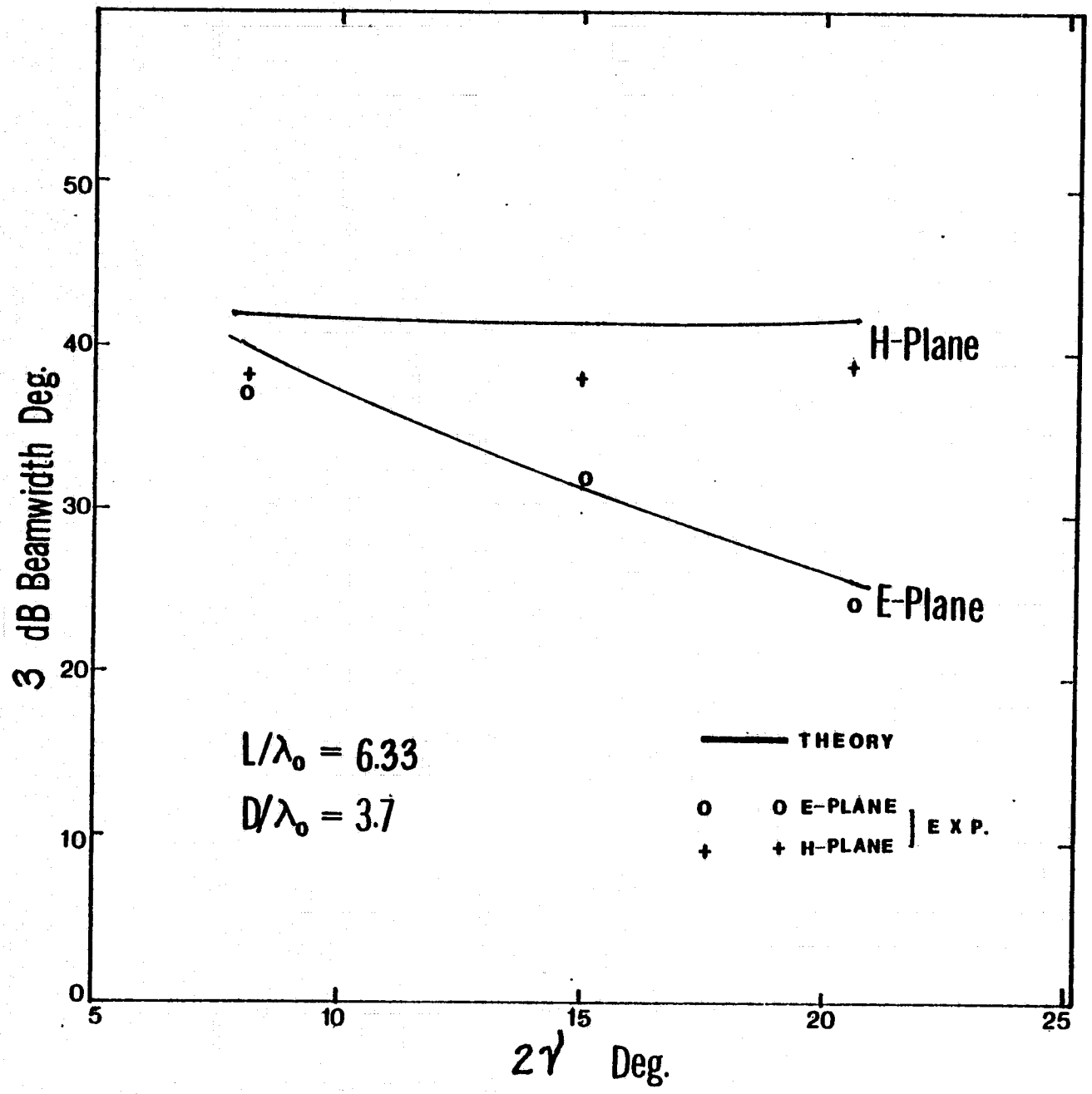
3 dB Beamwidth Deg.
50
40
30
20
10
0
5
10
15
20
25
2γ Deg.
H-Plane
E-Plane
L/λ₀ = 6.33
D/λ₀ = 3.7
THEORY
O E-PLANE
+ H-PLANE
EXP.

Fig. 5b

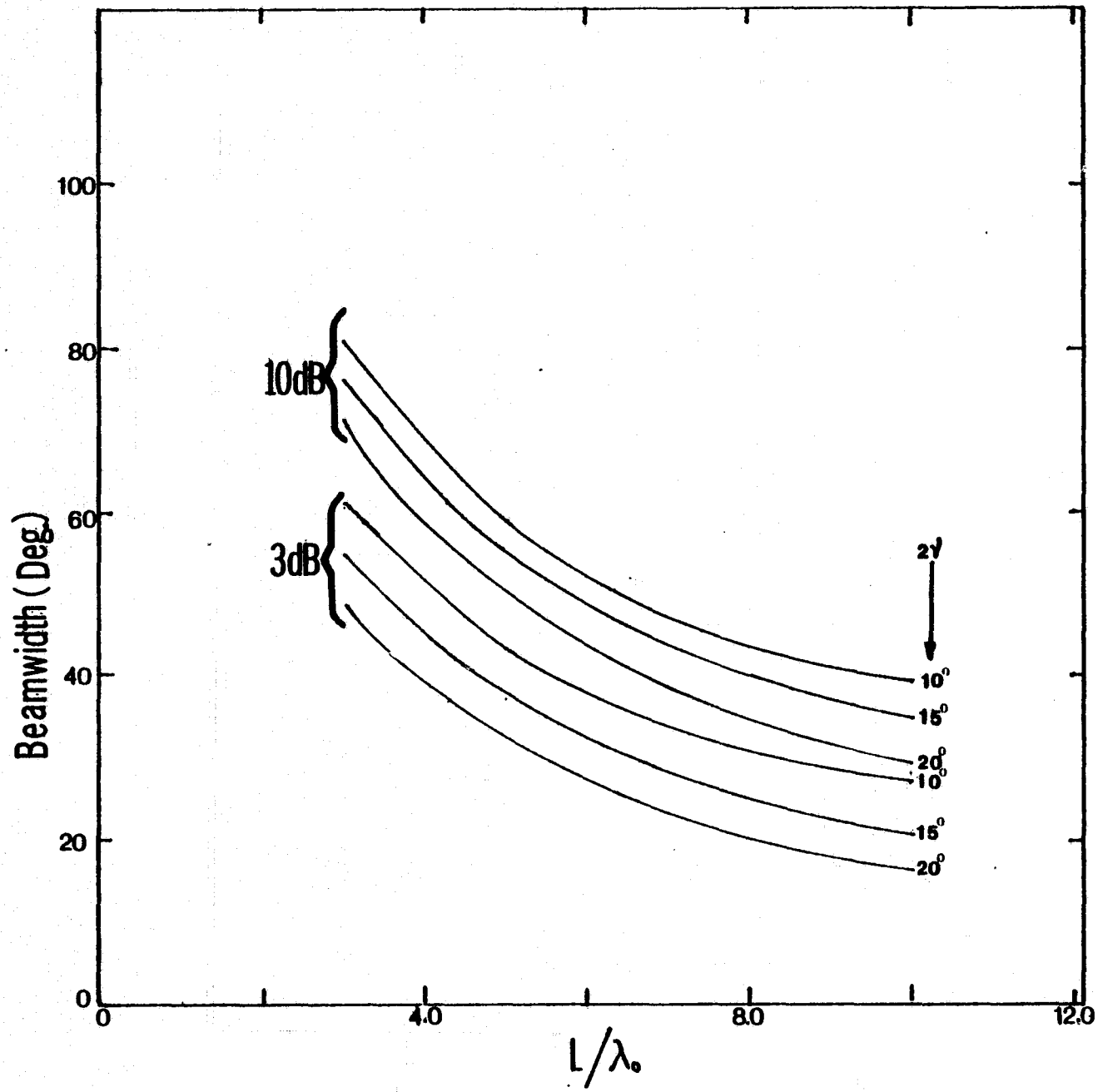
Beamwidth (Deg.)
100
80
60
40
20
0
10dB
3dB
2V
10°
15°
20°
10°
15°
20°
0
4.0
8.0
12.0
l/λ₀

FIG. 6a

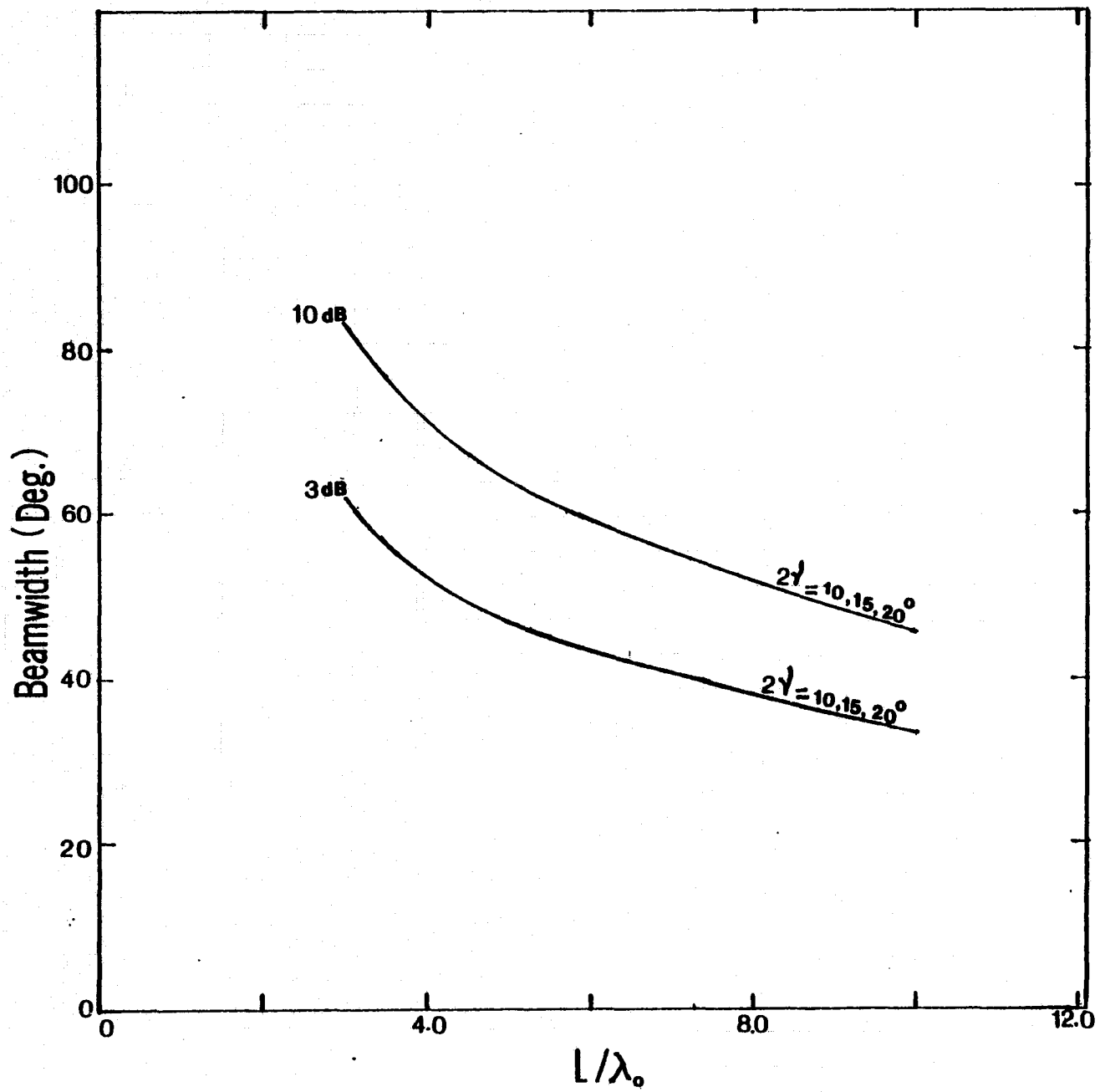
100
80
60
40
20
0
Beamwidth (Deg.)
10 dB
3dB
2γ = 10, 15, 20°
2γ = 10, 15, 20°
0
4.0
8.0
12.0
l/λ₀

FIG. 6b

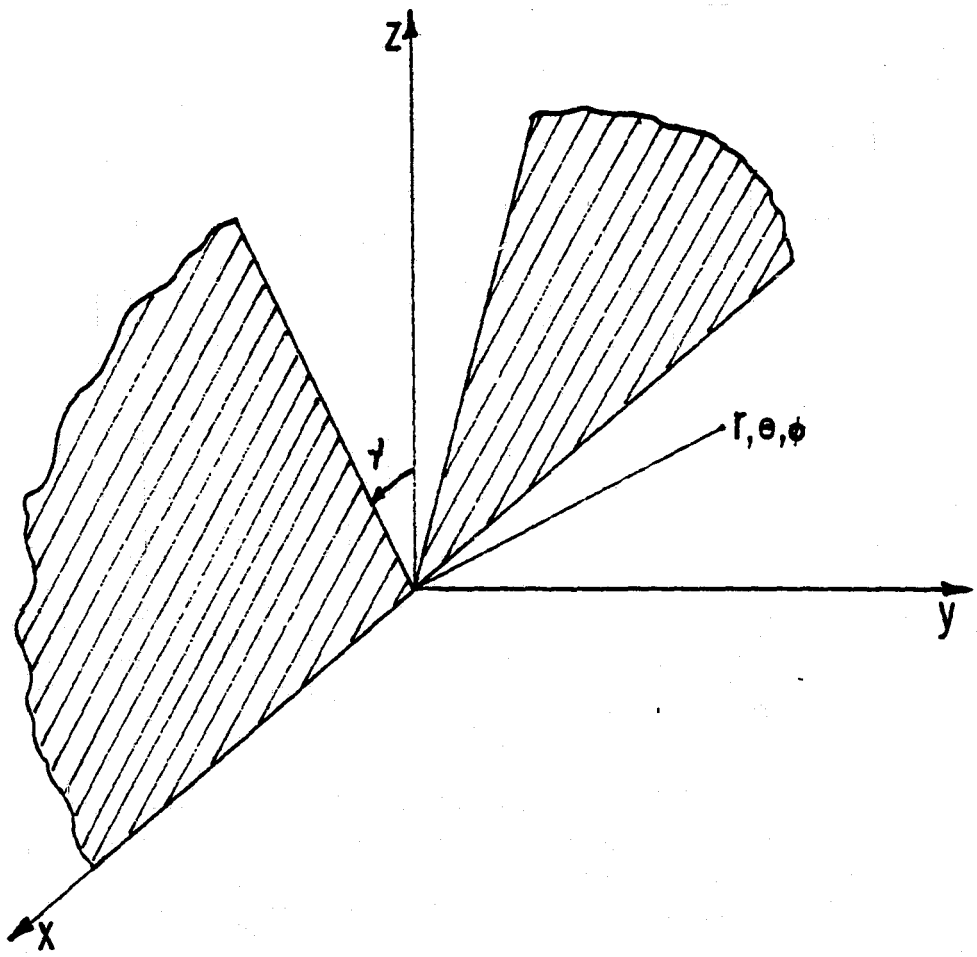

FIG. A1

APPENDIX VI

D4

Model experiments with slot antenna arrays for imaging

J.F. Johansson*, K.S. Yngvesson** and E.L. Kollberg*

* Department of Electron Physics I and Onsala Space Observatory, Chalmers University of Technology, S-412 96 Gothenburg, Sweden.

** Department of Electrical and Computer Engineering, University of Massachusetts, Amherst, Ma. 01002, USA.

APPENDIX 4 & 5 SENT TO AIAA

Abstract

We have developed a prototype imaging system at 31 GHz, which employs a two-dimensional (5x5) array of tapered slot antennas, and integrated detector or mixer elements, in the focal plane of a prime-focus paraboloid reflector, with an f/D=1. The system can be scaled to shorter millimeter waves and submillimeter waves. The array spacing corresponds to a beam spacing of approximately one Rayleigh distance and a two-point resolution experiment showed that two point-sources at the Rayleigh distance are well resolved.

Introduction

In radio astronomy the demand for observing time makes it necessary to use the equipment around the clock. The mapping of celestial objects can be a very time-consuming task, since many points need to be scanned and the finite integration time limits the throughput. One solution to this problem would be to use several antenna feeds at the same time. An array with N receptors yields an N-fold increase in mapping speed over a scanning system, at a given signal-to-noise ratio. Alternatively, the array can increase the sensitivity with a factor $\sqrt{N}$ for a given mapping speed.

Recently there has been a growing interest in imaging with feed arrays. Gillespie and Phillips[1] have proposed a horn array with bolometer detectors for radio astronomy at millimetric wavelengths. Rutledge et al[2] have used bow-tie receptors in a one-dimensional array for imaging. The bow-ties have also been used in a sub-mm version for fusion plasma diagnostics.[3]

Receptor requirements for imaging

It has been demonstrated that imaging systems require a focusing element (lens or reflector) with a high $f_\#$ (=f/D).[4] The number of elements that can be placed at the focus of a paraboloid can be computed using a formula given by Ruze.[5] The number of 3 dB beamwidths that can be scanned with a gain loss of 1 dB is

$$n = 0.44 + 22(f/D)^2 \qquad (1)$$

This limit ensures that the coma lobe level is below about -10 dB for a beam overlap at 3 dB. The number of receptors that can be placed at the focal plane without appreciable aberrations increases sharply when the $f_\#>1$. Hundreds of receptors could be used with an $f_\#=1$ two-dimensional imaging system, without any larger degradation of the imaging capabilities. This implies that either a primary-fed paraboloid with an $f_\#>=1$ or a Cassegrain system is preferred for imaging using reflectors.

Another parameter that affects the system performance is the blockage caused by the imaging array. To get a lower sidelobe level the blockage should be small, or entirely dispensed with by using an offset system.

The main requirement for the receptors is that they should provide symmetrical beams with a desired reflector edge illumination of about -10 to -13 dB even when they are densely packed. The power radiated outside the solid angle which is subtended by the reflector, as seen from the feed, should also be small. The ratio of this power and the total radiated power, denoted spill-over efficiency is

$$\eta_{sl} = \int_0^{\theta_0}\int_0^{2\pi} F(\theta,\phi)\sin\theta d\theta d\phi \;/\; \int_0^{\pi}\int_0^{2\pi} F(\theta,\phi)\sin\theta d\theta d\phi \qquad (2)$$

The coupling between the receptors should also be held at a low level to minimize cross-talk.

Endfire slotline antennas

A new type of planar receptor that belongs to the class of travelling-wave antennas has recently been investigated.[6] This antenna type consists of a dielectric substrate with a

metal ground-plane. A slot in the ground-plane is fed by a travelling wave. The radiation is maximal in the endfire direction, i.e. in the direction of the slot. The first antenna of this type (proposed by Gibson[7]) had an exponentially tapered slot width, and was given the name "The Vivaldi Aerial". The self-scaling properties of this antenna makes it extremely broadband.

We have experimented mainly with two other types; the Constant Width Slot Antenna (CWSA) and the Linear Taper Slot Antenna (LTSA). These types are less broadband but have narrower beams, compared with a Vivaldi antenna of the same length. The geometries of these three antenna types are shown in Figure 1.

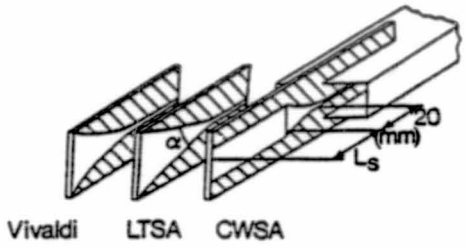

Figure 1. Three types of endfire slotline antennas.

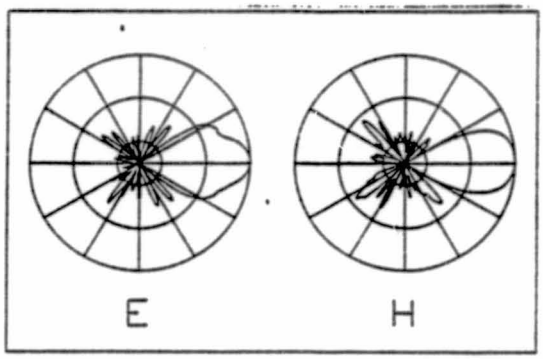

Figure 2. Radiation pattern of a CWSA at 31 GHz. 10 dB/div.

Typical E- and H-plane radiation patterns for a single CWSA element are shown in Fig. 2. The measurement was made at 31 GHz, the slot width was 8 mm, and the slot length was 10 mm. The substrate was .5 mm RT Duroid 5880 (ε_r=2.22).

We selected the CWSA antennas for our imaging arrays, since they proved to be easy to pack closely without much degradation of the beam patterns. We found it possible to use both sides of the substrate by interleaving the elements. They could then be even more densely packed without disturbing the slot field of their neighbours. (See Figure 3.)

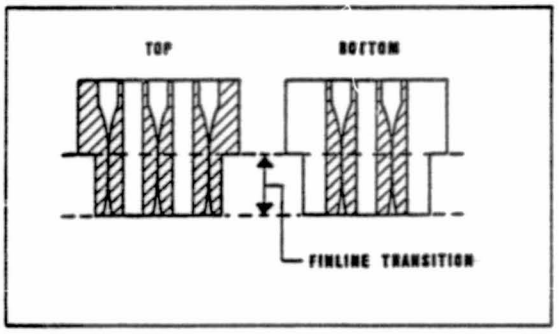

Figure 3. The two sides of the array substrate.

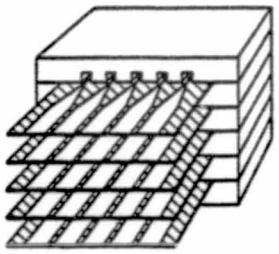

Figure 4. The 5x5 array with its waveguide fixture.

To facilitate measurements we made a slotline-finline-waveguide transition. The substrates could then easily be fitted into the waveguide fixture. A waveguide detector or mixer was bolted to the block at the selected element in the array. (See Figure 4.) In a real system it would of course be preferable to make full use of the planar geometry and integrate the mixer with the antenna. This design lends itself to a two-dimensional array, since the substrates can be densely packed in the H-plane without significant beam pattern degradation.

Antenna array measurements

To measure the antenna patterns we built a miniature anechoic chamber at Chalmers Univ. The chamber has a cross-section of 1x1 m and a distance of 2.0 meters between the transmitting and the receiving antenna. The antenna to be measured is placed on a turntable,

and is rotated by a stepping motor. The received signal is either fed to a Tektronix 492 spectrum analyser, used as a measurement receiver, or, in the detector case, to a 1 kHz amplifier and detector. The rotation and data acquisition is controlled by an HP9816 desk-top computer. To facilitate far-field measurements on larger antennas, it is possible to take off one side of the chamber and put the transmitter at a suitable distance.

To evaluate the array performance we measured different configurations of spacing and geometries for the array. A spacing of 13 mm at 31 GHz was found to be the best trade-off between spacing and radiation pattern properties.

The E- and H-planes of 9 of the elements in a 5x5 array with a 13 mm element spacing are shown in Figure 5. The numbering of the elements follows normal matrix notation, i.e. row number followed by column number. It is seen that the elements conform well with our requirements, i.e. about -10 dB at 28 degrees (the angle for an f_e=1 paraboloid). Note that despite the asymmetries in the array, the patterns are fairly symmetric.

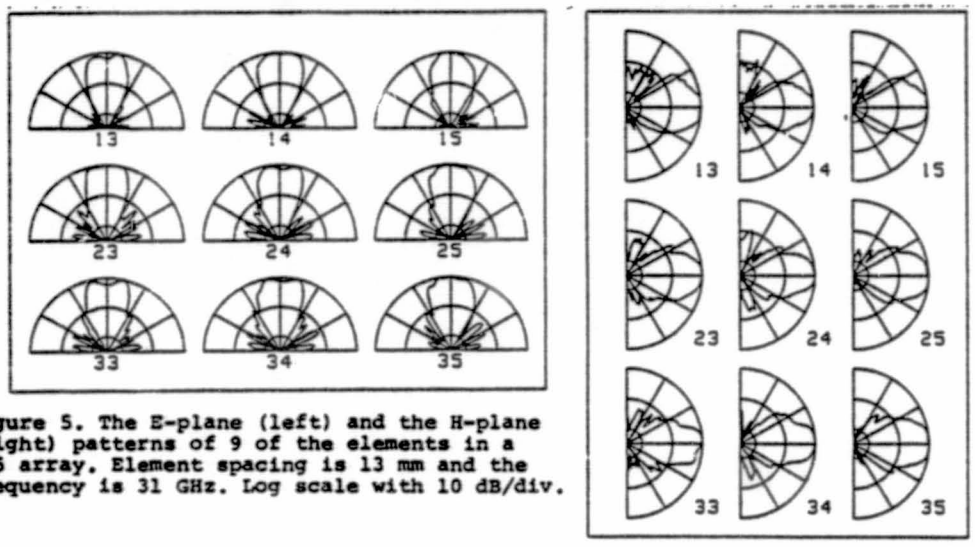

Figure 5. The E-plane (left) and the H-plane (right) patterns of 9 of the elements in a 5x5 array. Element spacing is 13 mm and the frequency is 31 GHz. Log scale with 10 dB/div.

The spill-over efficiency, as defined in (2), was numerically computed. The efficiency is in the region of 60-65 %, which is comparable to that of ordinary waveguide horn feeds (corrugated horns of course excepted). We also measured the patterns for a 10 mm spacing, but the patterns then showed more asymmetries and had broader beams, and hence lower spill-over efficiency.

Measured data for the imaging system

The arrays were placed at the prime focus of a commercial Millitech f_e=1, ϕ=305 mm paraboloid. The E- and H-plane patterns were measured for the different elements in the array. Figure 6 shows the E-plane patterns for the central, next-to-central, and the outer element in the mid row of a 3x5 array with 10 mm element spacing. Figure 7 shows the E-plane patterns for the 5 elements in the mid row of a 3x5 array with 13 mm element spacing. The sidelobe level is relatively high in the 13 mm case (about -10 dB), but this is consistent with the theoretical prediction for the 10 % of blockage. In the 10 mm case the blockage is smaller, but the unfavourable illumination gives a rise in the sidelobe level above the ideal.

The angular beam displacement $\delta\theta$ as a function of the lateral feed offset δx is given in a formula by Lee[8] as

$$\delta\theta = \arctan[(BDF)\cdot\delta x/f] \qquad (3)$$

The Beam Deviation Factor (BDF) is close to 1 for systems with f_e>1 at small offsets. The beam displacement is thus essentially a linear function of the lateral feed offset. Our measurements of the array with 13 mm element spacing gave beam displacements in the range of 2.1-2.6 degrees. This conforms well with the theoretical value of 2.33 degrees. With a stepping motor positioning accuracy of about +/- 0.2 degrees the discrepancy is acceptable.

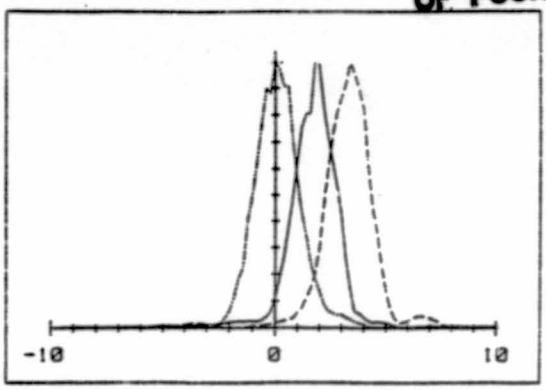

Figure 6. E-plane patterns for 3 elements in the mid row of a 3x5 array with 10 mm element spacing. Linear scale. Horizontal axis labelled in degrees.

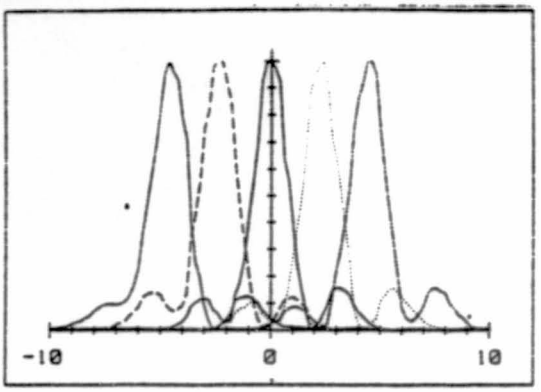

Figure 7. E-plane patterns for 5 elements in the mid row of a 3x5 array with 13 mm element spacing. Linear scale. Horizontal axis labelled in degrees.

Two-point resolution

Historically there exists a plethora of resolution criteria for optical systems. The two most well-known are the Rayleigh and Sparrow criteria.[9,10,11] Both these criteria are based on the Airy disc function,

$$I(r) = I_0 \left| \frac{2\, J_1[\pi r/(\lambda f_\#)]}{\pi r/(\lambda f_\#)} \right|^2 \qquad (4)$$

which is the diffraction pattern for a uniformly illuminated circular aperture. The Rayleigh distance is defined as the distance between the peak and the first null of the Airy disc. This distance, which is henceforth abbreviated δ_{Ra}, is given by

$$\delta_{Ra} = 1.219670\ \lambda f_\# \qquad (5)$$

Two sources at a separation of 1 δ_{Ra} give, when their amplitudes are added with a phase difference, an intensity pattern which is shown in Figure 8. Three cases of specific interest are shown:

- The in-phase case, i.e. a phase difference of 0 degrees.
- The quadrature case, " 90 degrees.
- The out-of-phase case, " 180 degrees.

We see in Figure 8 that the resolution is better for the quadrature case than the in-phase case. Note that for a two-source experiment the quadrature case is equivalent to the case of incoherent illumination.

The Sparrow criterion is based on the fact that the two peaks in the intensity pattern merge into one peak for a specific real separation. The Sparrow limit is 1.200463 δ_{Ra} for the in-phase case, and 0.776567 δ_{Ra} for the quadrature case.

To check the imaging qualities of the system we performed some two-point resolution experiments with the 3x5 array at 13 mm element spacing. Two conical horns were fed by a waveguide tee through an attenuator and a phase shifter. This made it possible to adjust the relative phase and amplitude of the two sources. The sources were excited with the same amplitude and the phase shifter was adjusted to get 0, 90, and 180 degrees of relative phase difference. The resulting antenna patterns are shown in Figure 9 for source separations of 0.77, 1.0, 1.2, and 1.45 δ_{Ra}.

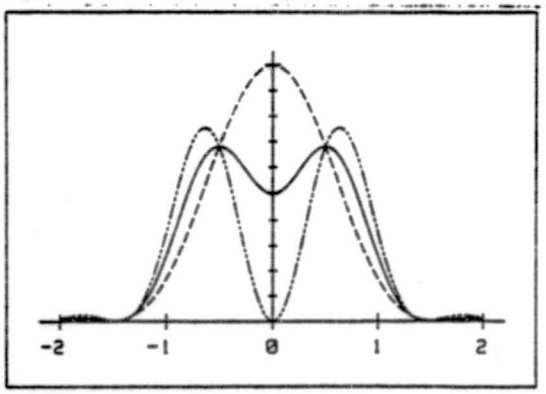

Figure 8. Intensity pattern of two point-sources separated by the Rayleigh distance. In-phase (--), quadrature (—) and out-of-phase (-·-·-). Labelled in Rayleigh dist. units.

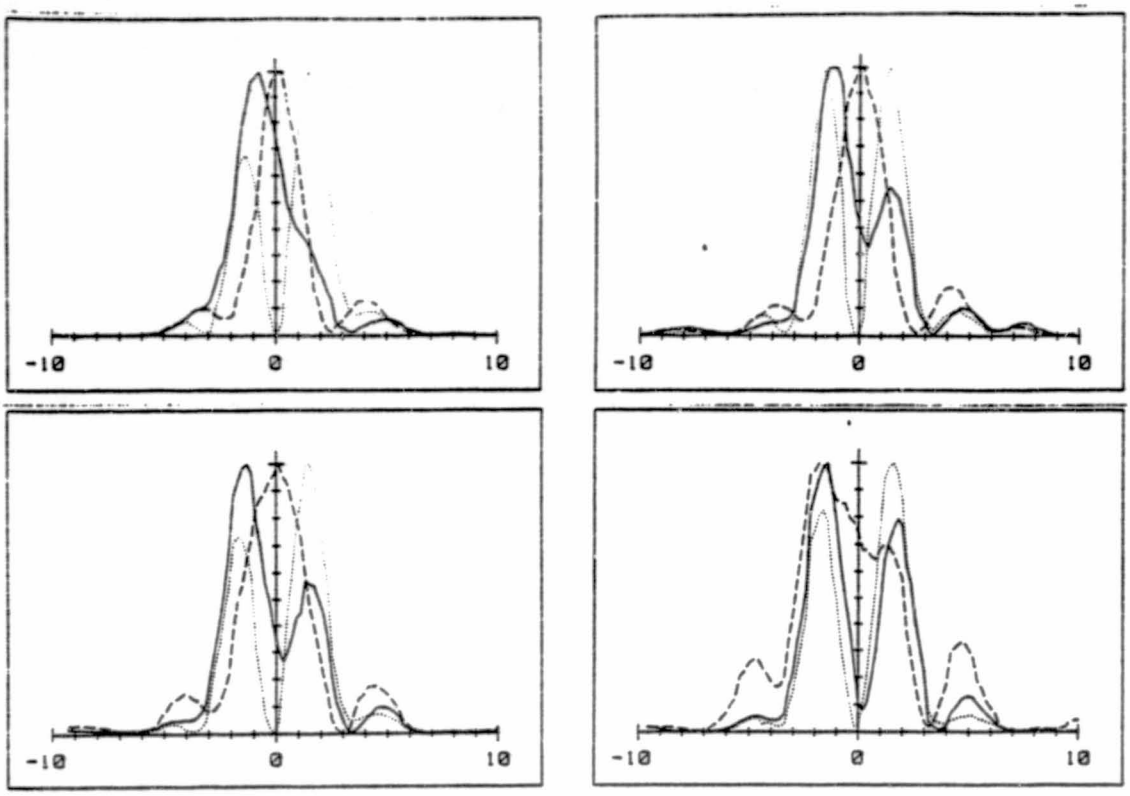

Figure 9. E-plane patterns for two point-sources. Separation is 0.77 (top left), 1.0 (top right), 1.2 (bottom left), and 1.45 δ_{Ra} (bottom right). The curves show phase differences of 0° (--), 90° (—), and 180° (··). Linear scale. Horizontal axis labelled in degrees.

The sources are resolved in the quadrature case (90°) for separations greater than or equal to 1.0 δ_{Ra}. In fact, the resolution is better than theory predicts for a uniformly illuminated dish. The blockage gives a narrower main lobe, but an increased side-lobe level is traded for this improvement in two-point resolution. A more complex object would thus be hard to resolve.

Plots of the apparent peak separation as a function of real separation for the three cases listed above are given in Figure 10.

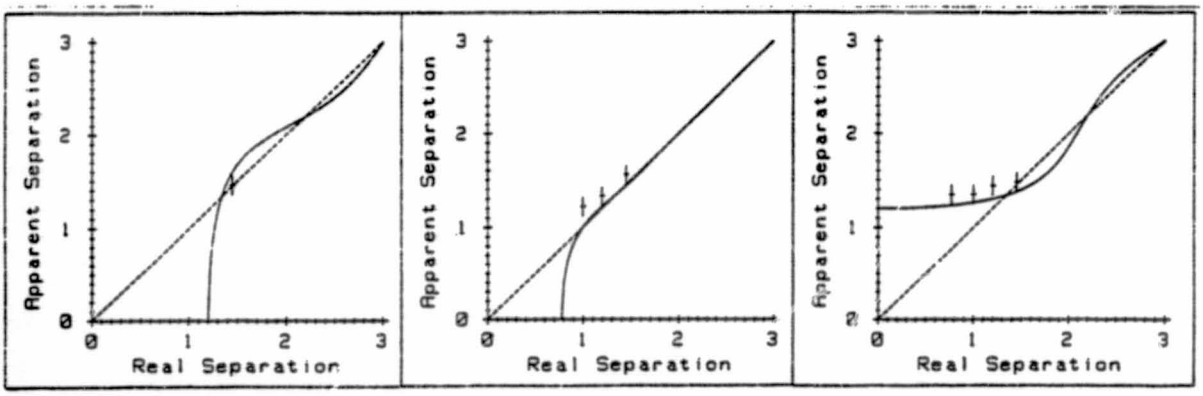

Figure 10.Apparent vs. real peak separation for a two-point source. The three cases are: in-phase (left), quadrature (middle), and out-of-phase (right). The axes are labelled in Rayleigh distance units. Measured points are also plotted in the figure.

Data points for the experiments with the 3x5 array at 13 mm separation are also plotted in the same figure. The points show the same qualitative separation dependence as the theoretical curves. The slight discrepancy between the measured and predicted separation is not unexpected since the prediction is based on an idealized system with uniform illumination.

The Optical Transfer Function (OTF)

A measure on the distortion which an imaging system introduces is the Optical Transfer Function (OTF).† With certain approximations (far-field, high $f_\#$) it is possible to use normal two-dimensional spatial Fourier transforms in the analysis of the system. In this model the input signal would be the object field and the output signal would be the image field. The system response is then represented by the OTF. The incoherent OTF for a circular aperture with uniform illumination is [9, 11]

$$H(\rho) = \begin{cases} \frac{2}{\pi}\left[\arccos\xi - \xi\sqrt{1-\xi^2}\right] & \xi<1 \\ 0 & \xi>1 \end{cases} \qquad \xi = \rho\lambda f_\# \tag{6}$$

which is shown in Figure 11. We see that the OTF is zero outside a radius of spatial frequency ρ given by

$$\rho = 1/(\lambda f_\#) \tag{7}$$

This is the cut-off frequency of the circular aperture system, i.e. spatial frequencies higher than this limit are irretrievably lost in the imaging process.

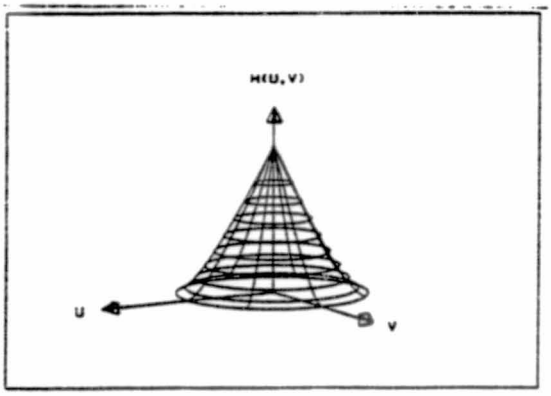

Figure 11. The OTF for a uniformly illuminated circular aperture.

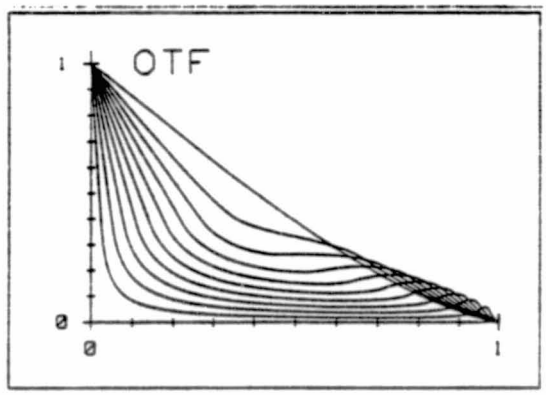

Figure 12. OTFs for annular apertures with increasing obscuration (0-90 %). Normalized axes.

An annular aperture, i.e. a circular aperture with a central circular obscuration, gives an OTF with a relative enhancement of high spatial frequencies. This gives an antenna pattern with a narrower main lobe and an increased side-lobe level. OTFs for annular apertures with different degrees of obscuration are plotted in Figure 12, to show the enhancement of high spatial frequencies.

The Fourier transform of the OTF gives the Point Spread Function (PSF), which represents the response in the image plane to a point source in the far-field. With angular coordinates instead of linear, this PSF is a good approximation of the antenna radiation pattern, if a high $f_\#$ is assumed.[12] This enables us to compute the OTF for an antenna system just by Fourier transforming the antenna pattern. For the circularly symmetric case this means taking the Hankel transform of the antenna pattern,

$$H(\rho) = C\, 2\pi \int_0^\infty F(\theta) J_0(2\pi\rho\sin\theta)\sin\theta\, d(\sin\theta) \tag{8}$$

A numerically efficient Hankel transform method is due to Barakat[13], and the transform formula is given by (9).

† Throughout this paper it is assumed that the OTF is real and non-negative. The OTF is then equivalent to the Modulation Transfer Function (MTF), which is the modulus of the OTF.

$$H(\rho) = \sum_{n=1}^{\infty} \frac{F[\alpha_n/(2\pi\psi)]\, J_0(\alpha_n \rho/\psi)}{[J_1(\alpha_n)]^2} \Big/ \sum_{n=1}^{\infty} \frac{F[\alpha_n/(2\pi\psi)]}{[J_1(\alpha_n)]^2} \qquad J_0(\alpha_n) = 0 \quad \rho > \psi \Rightarrow H(\rho) \ll 1 \tag{9}$$

The OTF resulting from a Hankel transform of the measured radiation patterns for the 3x5 array with 13 mm element spacing is shown in Figure 13. The 'ideal' OTF (6) for an $f_\#$=1, ϕ=305 mm paraboloid is also plotted in the diagram for comparison. There is a noticeable dip in the OTF for the measured pattern. This is evidently due to the large blockage (10 %) encountered in this case.

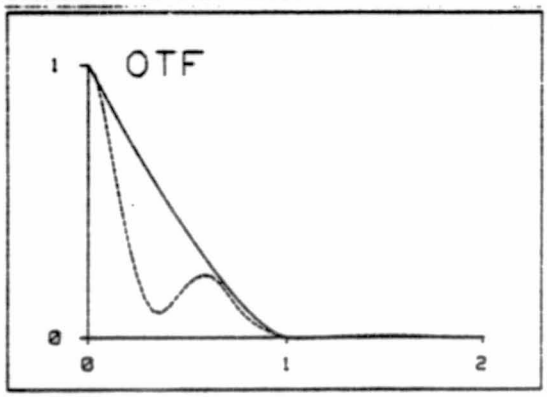

Figure 13. Calculated OTF (---) for an element in the 3x5 array with 13 mm spacing. Ideal OTF with cut-off at 1 (normalized) is also plotted (——).

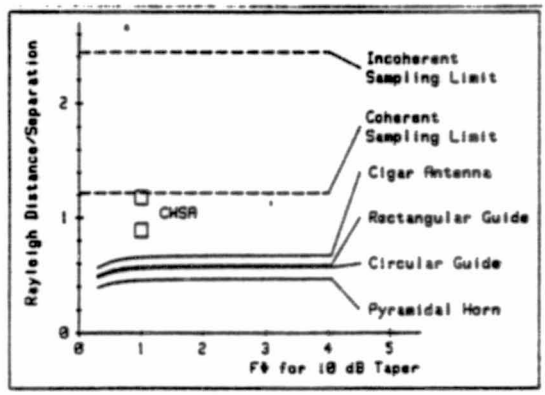

Figure 14. Comparison of packing density for different antenna feeds.

Image sampling

In the optical case, we can achieve image sampling by putting a high-resolution film in the image plane. For millimetre waves it is not possible to sample the image field distribution with an arbitrarily close sampling separation. The finite size of feeds which give low spill-over losses prevents feed separations closer than about $\lambda f_\#$. Using the Whittaker-Shannon sampling theorem[14,15], we can show that the maximum sampling separation which gives a completely diffraction-limited incoherent resolution is:

$$\Delta x = \lambda f_\# / 2 \tag{10}$$

The incoherent sampling limit is thus 1/2.44 of the Rayleigh distance for a system (the coherent sampling limit is twice this value, i.e. 1/1.22 of the Rayleigh distance).

It is convenient to compare different microwave feeds with regard to how closely they can be packed. Rahmat-Samii[16] has made calculations for four different feed types. Using his data, and calculating the realizable feed separation for a size which illuminate an $f_\#$ paraboloid with -10 dB at the edge, we get Figure 14. It is evident that increasing the $f_\#$ will not give any better resolution. In the same figure our data is plotted. Note that the CWSA array is nearly twice as good as the circular waveguide antenna array. The explanation of this enhanced packing density is that the slot antennas use their length to increase the gain over the equivalent cross-section aperture gain. The incoherent and the coherent sampling limits are also indicated in the figure. The fact that present two-dimensional imaging systems are inferior to the incoherent limit by a factor of at least two means that true diffraction limited resolution is still some distance away.

Integrated mixers

We intend to integrate beam-lead mixers/detectors with the antennas in the full 5x5 array in a scaled-down version. A scaling to a higher frequency would decrease the array size, and thus the blockage. Preliminary experiments at 31 GHz show about 10 dB conversion loss for an integrated mixer with an HP HSCH 5330 beam-lead diode. The corresponding circuit is shown in Figure 15. The design uses a slotline filter as an IF/bias filter.

For arrays with mixers, local oscillator (LO) power can be injected through a hole at the centre of the paraboloid. A rough estimate of the LO loss is 10-15 dB for a 1 dB variation in LO power over the array. The hole would then cover about 1 % of the reflector area, and would thus introduce negligible losses.

One interesting experiment would be to build an array with integrated SIS junctions. This would give excellent receiver noise performance.

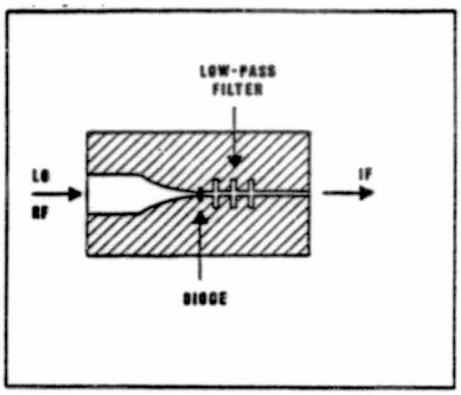

Figure 15. The integrated mixer circuit. A single CWSA element is shown.

Conclusion

We have used a two-dimensional 5x5 array of CWSA slotline antennas for imaging in the millimetric range. The receptors showed acceptable performance when used together with an $f_{\#}=1$ paraboloid. The achieved packing density is superior to conventional antennas for the same performance. The results are encouraging and we intend to continue the research in this area.

Acknowledgments

The financial support from the National Swedish Board for Technical Development and the Swedish Board for Space Activities is gratefully acknowledged. One of us (K.S Yngvesson) would like to acknowledge support for his sabbatical leave from the University of Massachusetts. We also thank our workshop personnel for their help with mechanical details.

References

1. A.R. Gillespie and T.G. Phillips, "Array Detectors for Millimeter Line Astronomy", Astron. Astrophys. 73, pp. 14-18, 1979.
2. D.B. Rutledge and M.S. Muha, "Imaging Antenna Arrays", IEEE T-AP-30, pp. 535-540, July 1982.
3. D.B. Rutledge, "Substrate-Lens Coupled Antennas for Millimeter and Submillimeter Waves", IEEE APS Newsletter, pp. 5-8, Aug. 1985.
4. K.S. Yngvesson, in "Infrared and Millimeter Waves" (K. Button, ed.), Vol. 10, pp. 91-110, Academic Press, 1983.
5. J. Ruze, "Lateral Feed Displacement in a Paraboloid", IEEE T-AP-13, pp. 660-665, Sept. 1965.
6. K.S. Yngvesson, et al, "Endfire Tapered Slot Antennas on Dielectric Substrates", To appear in IEEE Trans. Ant. & Prop.
7. P.J. Gibson, "The Vivaldi Aerial", Proc. 9th EuMC, pp. 101-105, 1979.
8. Shung-Wu Lee and Y. Rahmat-Samii, "Simple Formulas for Designing an Offset Multibeam Parabolic Reflector", IEEE T-AP-29, pp. 472-478, May 1981.
9. J.W. Goodman, "Introduction to Fourier Optics", McGraw Hill, 1968.
10. D.E. Stoltzmann, "The Perfect Point Spread Function", Applied Optics and Optical Engineering, Vol. IX, Ch. 4, pp. 111-148.
11. B.J. Thompson, "Image Formation with Partially Coherent Light", in "Progress in Optics", Vol. VII (E. Wolf, ed.), pp. 171-230, North Holland Publ. Co, 1969.
12. H.C. Minnett, et al, "Fields in the Image Space of Symmetrical Focusing Reflectors", Proc. IEE, Vol. 115, No. 10, pp. 1419-1430, Oct. 1968.
13. R. Barakat, "Application of the Sampling Theorem to Optical Diffraction Theory", J. Opt. Soc. Am., Vol. 54, No. 7, pp. 920-930, July 1964.
14. R.N. Bracewell and J.A. Roberts, "Aerial Smoothing in Radio Astronomy", Australia J. Phys., 7, pp. 615-640, 1954.
15. R.N. Bracewell, "Two-Dimensional Aerial Smoothing in Radio Astronomy", Australia J. Phys., 9, pp. 297-314, 1956.
16. Y. Rahmat-Samii, et al, "Realizable Feed-Element Patterns for Multibeam Reflector Antenna Analysis", IEEE T-AP-29, pp. 961-963, Nov. 1981.

A New Integrated Slot Element Feed Array for Multi-Beam Systems

K. Sigfrid Yngvesson, Member, IEEE, J. Johansson, Student Member, IEEE, and Erik L. Kollberg, Member, IEEE

K.S. Yngvesson is with the Department of Electrical and Computer Engineering, University of Massachusetts, Amherst, Mass. 01003.

J. Johansson and E.L. Kollberg are with the Department of Electron Physics I and Onsala Space Observatory, Chalmers University of Technology, S-41296 Gothenburg, Sweden

Abstract

A feed array consisting of constant width slot antennas (CWSA's), fed from a block containing fin-line transitions, has been developed. The array has a two-dimensional configuration, with five elements each on five parallel substrates. Beam-widths are compatible with use in f/D = 1.0 multi-beam systems, with optimum taper. Array element spacings are close to a factor of two smaller than for other typical arrays, and spill-over efficiency is about 65%.

Introduction

Integrated antenna arrays are presently being developed for a large number of applications. Multi-beam antenna systems, utilizing an array which feeds a reflector or a lens, however, still often are restricted to using waveguide type arrays. Some exceptions can be noted for the area of imaging multi-beam systems, such as the endfire tapered slot element array of Korzeniowski et al [1], and the linear bow-tie array used by Rutledge et al [2]. Farr et al [3] have studied fin-line antenna elements, but not given any results on arrays of such elements. Tapered slot arrays have the advantage of being fully two-dimensional. Such an array has been developed further in the work reported here, and has been adapted for use with reflector antennas (or lenses) with an f/D of about one. This is a common f-number for both imaging and communication satellite antenna applications, since it allows a conveniently large number of beams. Constant width slot elements (CWSA's) have been employed, as shown in Figure 1. A significant advantage of the CWSA array is that the spacing between elements can be made smaller by about a factor of two, compared with a waveguide array used in a system with the same f-number.

Array Design

The array design was based on work with single elements of endfire tapered slot antennas, described in other publications [4], [5]. Such antennas achieve a somewhat enlarged gain due to the traveling-wave nature of the radiation mechanism, compared with what one would expect from the cross-sectional dimensions. It is important to note

that it is possible to design slot elements such that the beam width is the same in both the E– and the H–plane (the plane of the substrate is the E–plane, and the plane perpendicular to the substrate is the H–plane). Endfire slot elements radiate most efficiently when the slot width approaches one wavelength. An efficient CWSA, for example, utilizes an exponential taper from a narrow slot to a a slot of constant width equal to about $0.8\lambda_o$ (see Figure 1). The length of the constant width section is determined so that the required beamwidth at the edge of the reflector (or lens) is obtained (see [4]). Alternative shapes studied in [4] and [5] have either linear of exponential tapers in the radiating region of the antenna element, but the CWSA was chosen for this study since it resulted in the smallest aperture dimensions and therefore the most compact array. The edge angle of a parabolic dish of f-# one is 56° (full width), and the array was designed for an edge taper of approximately –10 dB for optimum illumination of the dish. Other values of the edge angle can be matched by adjusting the length of the constant width section. In our case, a single element with a length of this section equal to 10 mm met the specifications for an array to be used at 31 GHz. Radiation patterns of single elements are of course modified when the elements are placed in the array, but can still be used as a rough guide to the beamwidths one can expect in the array environment.

Experimental Details

A fin–line fixture was used for feeding the antenna array, as shown in Figure 1. Inside the metal block, the slot width is tapered to the height of the waveguide to form a fin–line transition. A standard waveguide mixer for a spectrum analyzer was used as a detector. In all cases, an 0.5 mm thick Duroid substrate was used. This thickness was about optimum for the fairly short antennas which met the specification for the beamwidth. Radiation patterns were recorded either by reading the peak spectrum analyzer signal, or by modulating the transmitter at 1 kHz, and using a narrow band amplifier after the detector. A small antenna range in the form of a box with a trapezoidal section for the source, and with all inside surfaces covered with Eccosorb material, was employed. The test antenna or array was turned by a stepping motor under control by a Hewlett–Packard 9816 computer. Data were accessed and plotted by the computer automatically. The linear dynamic range attained was typically 25–30 dB.

Experimental Results

The radiation patterns in the E– and H–planes for single elements are shown in Figure 2. Single CWSA elements can show shoulders on the E–plane pattern. The amplitude and location of the shoulders depend on the size and shape of the block, as well as the frequency. While such interaction effects with the fixture are presently not exactly predictable, it is possible to empirically eliminate any undesirable shoulders on the beam, for example by changing the frequency.

When elements of the above type were assembled into an array, it was found that the shoulders were not present in the E–plane pattern. It was found convenient to place alternate elements on opposite sides of the substrate, thus allowing the elements to be DC–insulated from each other. Despite the asymmetrical placement, only very small asymmetries in the radiation patterns were typically measured, after the widths of the copper strips which define the constant width sections had been trimmed. Measured radiation patterns for an array of 5x5 elements, with a spacing of 13 mm (about $1.33\lambda_o$) both between elements on a substrate, and between adjacent substrates, are shown in Figure 3. Elements have been numbered using the convention which is used for a square matrix, while viewing the array from the detector side. Thus, element 33 is the central element, etc. Only patterns for the right–hand upper quadrant are given, since data for the other quadrants are identical due to the symmetry of the array.

Coupling effects between the elements modify the E–plane patterns so that they become more flat–topped. The taper at the specified opening angle for an f/D = 1 system (56°) is still about –10 dB, however. For the H–plane patterns, typical tapers at the specified opening angle also are in the range –8 to –10 dB and thus agree with the design specification. The only exception to this are the H–plane patterns for elements 13 and 15, which have tapers which have increased to –5 dB on the side of the beam which is away from the center of the array, but show a normal taper on the other side of the beam. Also the sidelobes are notably asymmetric. The asymmetry can be easily explained, since these elements are on the outermost substrate. It is easy to remedy the asymmetry, if desired, by using an extra "dummy" substrate on each side of the array.

A 1x5 element array was also measured with similar results, see Figure 4.

Discussion

The design effort was guided by the earlier experience with arrays of linearly tapered slot antennas, which had demonstrated that it was possible to achieve quite small element spacings in endfire tapered slot arrays [1]. Data were also taken for a CWSA array with a 10 mm spacing, but this array did not have a symmetric beamwidths in the E– and H–planes. The spacing of 13 mm, which met the design specification, is to our knowledge the smallest spacing achieved in a two–dimensional array, matched to an f/D = 1 dish. The significance of this fact can be illustrated by comparison with data for arrays constructed from other types of elements. For example, an array of conical horn feeds which would give an edge taper of –10 dB for an f/D = 1 dish at 31 GHz, must have an inside aperture diameter for each element of 20 mm. Allowing for the thickness of the waveguide walls, it is seen that the spacing in the CWSA array is about one half that of the comparable conical horn array. The cross–sections of the two arrays are compared in Figure 5.

In a recent publication, Rahmat–Samii et al have compared the gain of different types of feed elements which might be used in arrays [6] (cigar antennas, rectangular and circular

waveguides, and a pyramidal horn). A standard feed power pattern of the form $(\cos\theta)^{2q}$ was used, and the q-value was found for arrays of different types of elements as a function of the normalized distance between elements. We have adapted the data used by Rahmat-Samii et al so that a comparison can be made of the angular resolution (proportional to element spacing) which can be obtained in an imaging system of a given f-#, using arrays of the different types of feed elements. A taper of -10 dB was assumed, and the Rayleigh distance divided by the element spacing is plotted versus f-# in Figure 6. The Rayleigh distance, δ_{Ra} is the element spacing which corresponds to the images of two point-sources, which can just be resolved according to the Rayleigh criterion [7]. It is given by:

$$\delta_{Ra} = 1.22\lambda_o f - \# \qquad (1)$$

The sampling limit, marked in Figure 6, corresponds to an element spacing of $\delta_{Ra}/2.44$ [7]. Data for tapered slot arrays from this work, as well as [1], have been included, and show that tapered slot arrays give superior resolution to other types of elements. Equally interesting is to note that there is a potential for substantially decreasing the beam-spacing in a multi-beam satellite antenna by employing a tapered slot-antenna array.

Another factor which has a bearing on the utility of the CWSA arrays in multibeam systems is the spill-over efficiency, i.e. the fraction of the power radiated by an element in the array, which would be within the full edge-angle of the dish or lens. We have estimated the spill-over efficiency by using the E- and H-plane radiation patterns, and assuming a smooth cosine variation between these planes. Typical results are about 65%.

One may therefore conclude that CWSA arrays have spill-over efficiencies close to those of comparable waveguide arrays as well as offering significantly closer beam spacings than the latter. Considering the ease and decreased cost of fabrication, as well as lower weight, CWSA and other tapered slot antenna elements can thus be considered as attractive alternatives for multi-beam antenna systems.

References

[1] Korzeniowski, T.L., Pozar, D.M., Schaubert, D.H., and Yngvesson, K.S., "Imaging System at 94 GHz Using Tapered Slot Antenna Elements", 8th Intern. Conf. Infr. Millimeter Waves (1983).

[2] Rutledge, D.B., and Muha, M.S., "Imaging Antenna Arrays", IEEE Trans. Antennas and Propag., AP-30, 535—540 (1982).

[3] Farr, E., Webb, K., and Mittra, R., "Studies in Fin-Line Antenna Design for Imaging Radar Applications", Arch. Electr. Ubertr., 39, 87—89 (1985).

[4] Yngvesson, K.S., Schaubert, D.H., Korzeniowski, T.L., Kollberg, E.L., Thungren, T., and Johansson, J., "Endfire Tapered Slot Antennas on Dielectric Substrates", accepted for publication, December 1985 issue, IEEE Trans. Antennas and Propag.

[5] Korzeniowski, T.L., "A 94 GHz Imaging Array Using Slot Line Radiators", Ph.D. Thesis, Department of Electrical and Computer Engineering, University of Massachusetts, August 1985.

[6] Rahmat-Samii, Y., Cramer, P., Jr., Woo, K., and Lee, S.W., "Realizable Feed-Element Patterns for Multibeam Reflector Antenna Analysis", IEEE Trans. Antennas and Propagat., AP-29, 961—963 (1981).

[7] Goodman J.W., "Introduction to Fourier Optics", McGraw-Hill, New York:1968.

Acknowledgements

Support from the following sources is gratefully acknowledged: The work on tapered slot antennas and arrays at the University of Massachusetts is supported by the NASA Langley Research Center, Hampton, Va., under grant number NAG-1-279. The University of Massachusetts supported Professor Sigfrid Yngvesson's sabbatical leave at Chalmers University of Technology. Work on tapered slot antennas and arrays at Chalmers University is supported by the Swedish Board for Technical Development.

Figure Captions

Figure 1. CWSA array using a fin-line fixture.

Figure 2. Radiation patterns measured on single elements of CWSA's in a finline fixture.

Figure 3. Measured radiation patterns for a 5x5 CWSA array in a fin-line fixture, with 13 mm element spacing in both planes. Data for the upper right-hand quadrant of the array are shown, with elements numbered in matrix notation as shown in (a), (b) shows E-plane patterns, and (c) H-plane patterns.

Figure 4. Measured radiation patterns of a 1x5 CWSA array in a fin- line structure, with 13 mm spacing between elements, (a) E-plane, (b) H- plane.

Figure 5. Comparison of the cross-sections of (a) a CWSA array and (b) a conical waveguide horn array, both adapted for optimum illumination of an f/D = 1 dish at 31 GHz.

Figure 6. Plot of Rayleigh distance, δ_{Ra}, divided by the element-spacing for arrays of the following elements: (a) CWSA (this paper) (b) LTSA [1], (c) Cigar antenna [6], (d) Rectangular guide [6], (e) Circular guide [6], (f) pyramidal horn [6]. The array elements are assumed to illuminate a reflector with f-# given on the horizontal axis, and with a -10 dB taper.

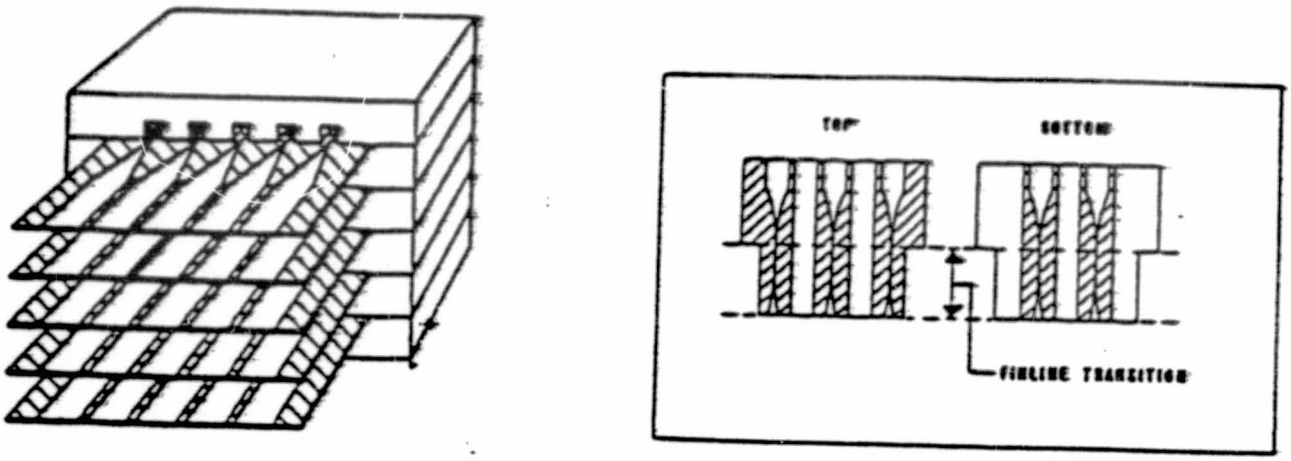

Figure 1

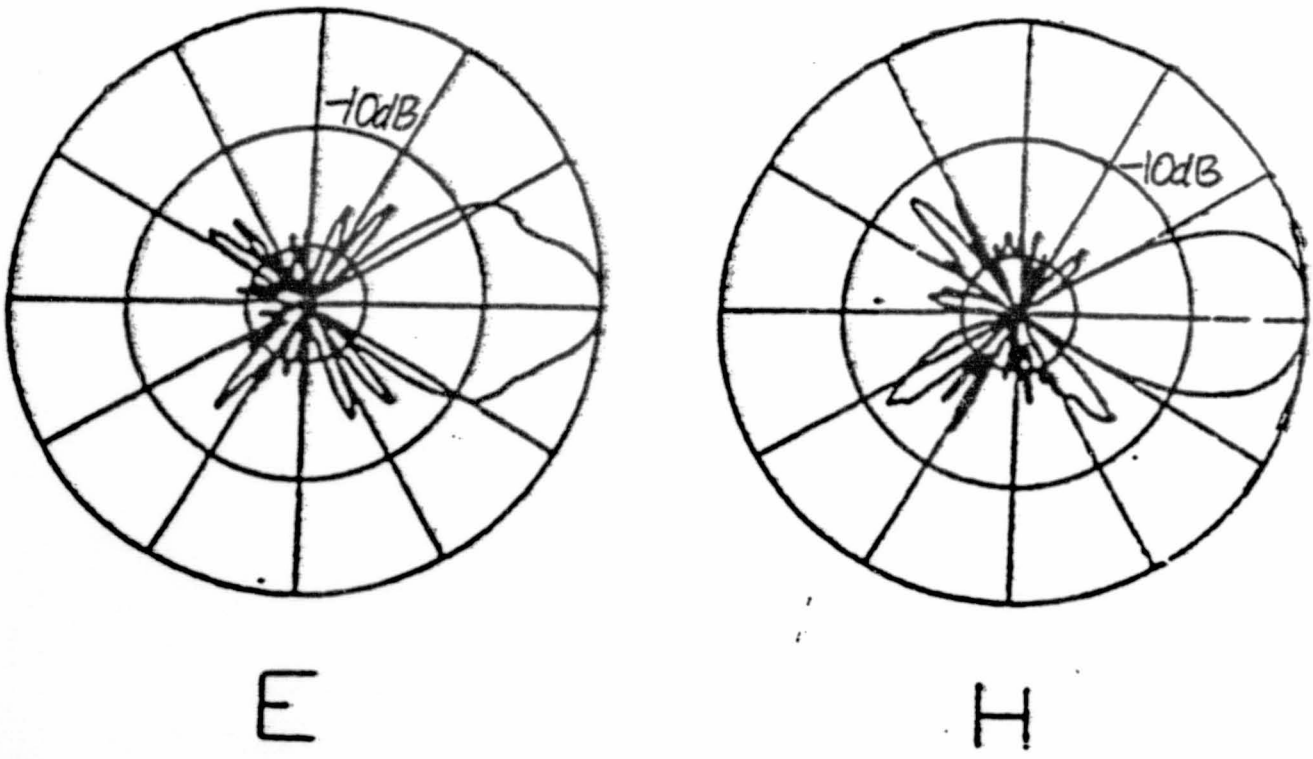

Figure 2

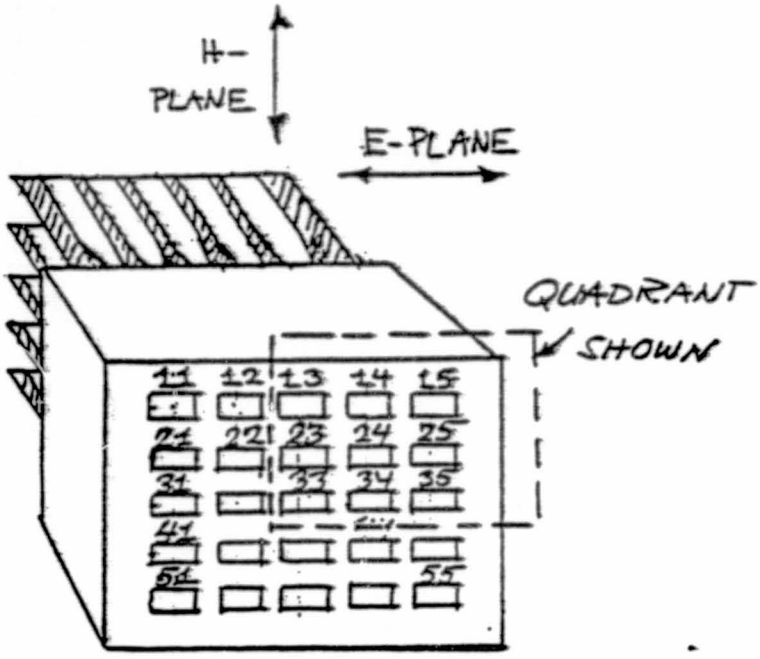

Figure 3a

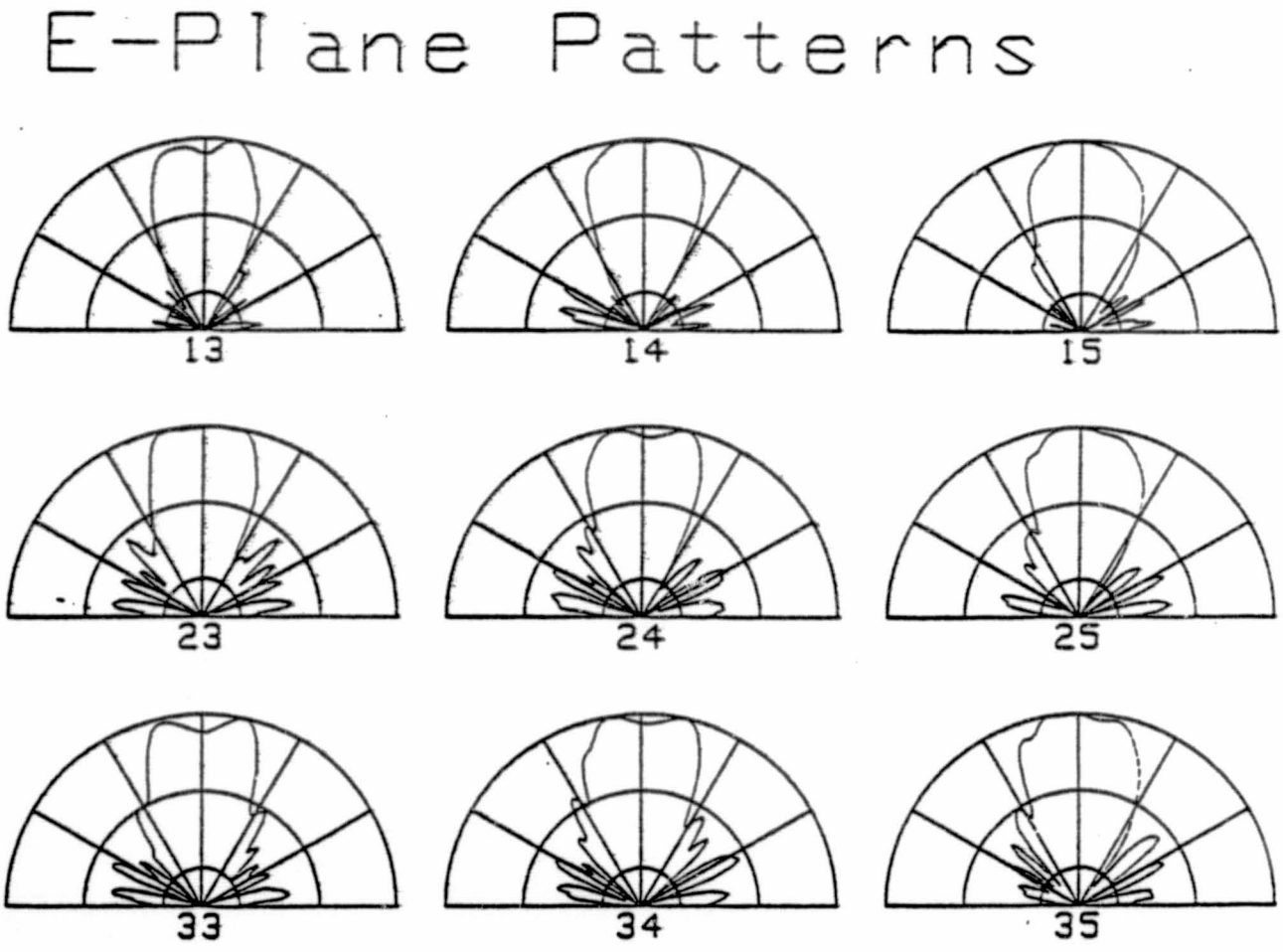

Figure 3b

H-Plane Patterns

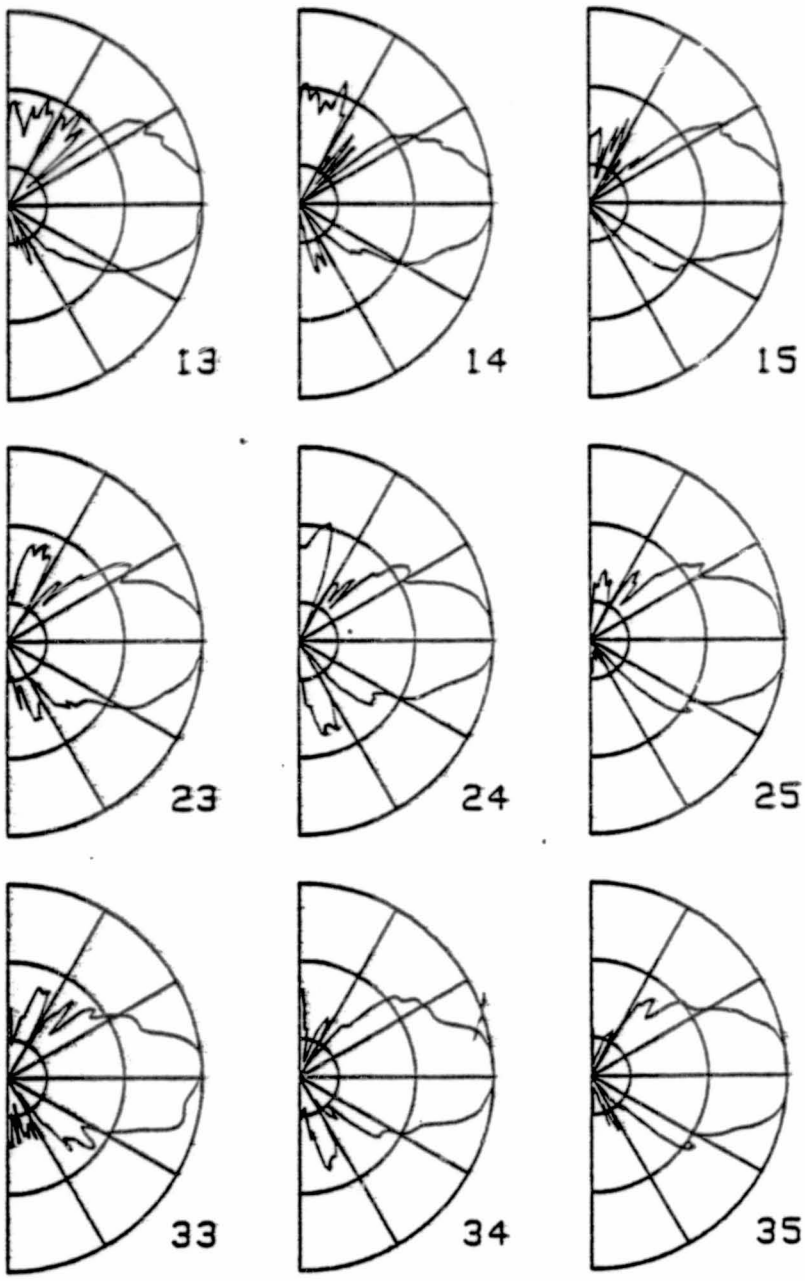

Figure 3c

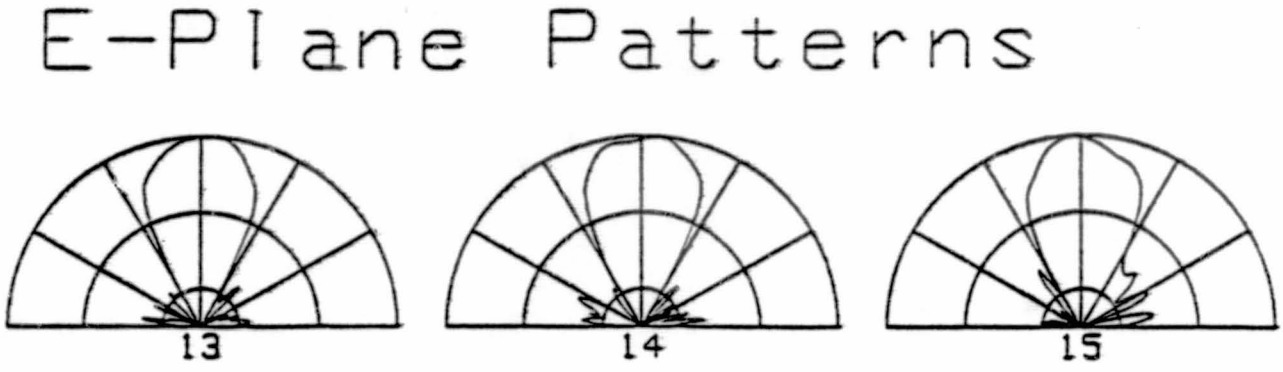

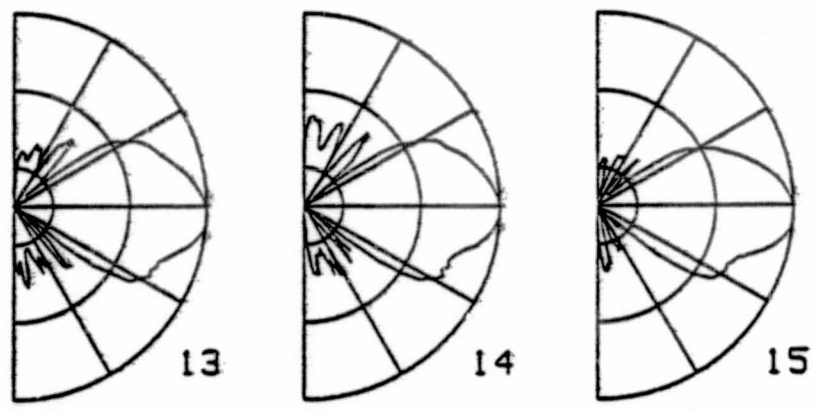

Figure 4

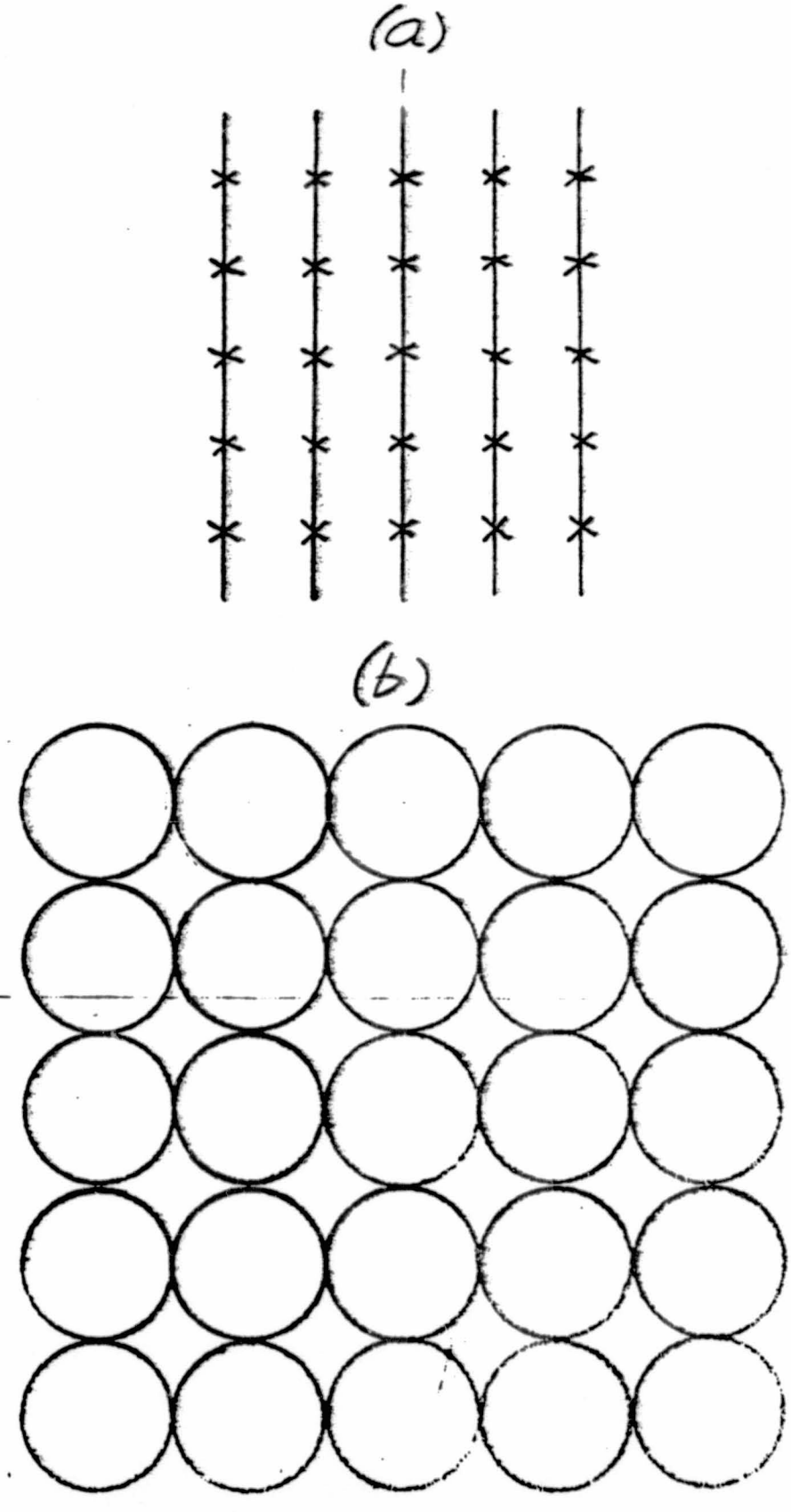

Figure 5

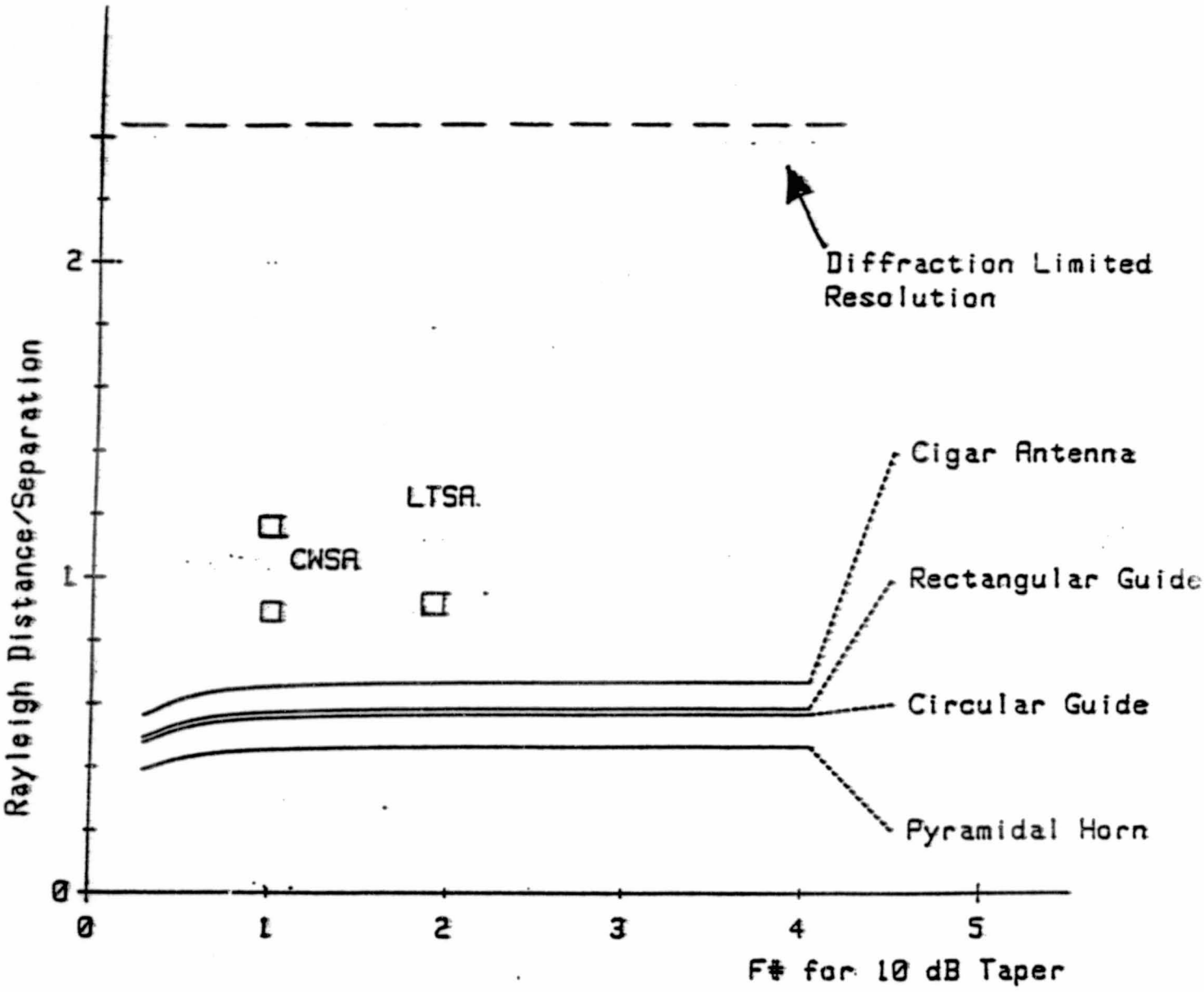
Diffraction Limited
Resolution
Cigar Antenna
Rectangular Guide
Circular Guide
Pyramidal Horn
LTSA
CWSA
Rayleigh Distance/Separation
F# for 10 dB Taper
0
1
2
3
4
5

Figure 6